

---

# Ground-based remote sensing of warm low-level stratified clouds - new perspectives and applications

---

INAUGURAL-DISSERTATION  
zur  
Erlangung des Doktorgrades  
der Mathematisch-Naturwissenschaftlichen Fakultät  
der Universität zu Köln

vorgelegt von  
**Nils Küchler**  
aus Karlsruhe

Köln, 2019



BERICHTERSTATTER:  
PD Dr. Ulrich Löhnert  
Prof. Dr. Roel Neggers

TAG DER MÜNDLICHEN PRÜFUNG:  
26.10.2018

*“Man kann einem Menschen nichts lehren; man kann ihm nur helfen, es in sich selbst zu finden.”*

Galileo Galilei (1564 - 1642)



# Contents

|  |           |
|--|-----------|
| <b>Zusammenfassung</b>   | <b>1</b>  |
| <b>Abstract</b>  | <b>5</b>  |
| <b>1 Introduction</b>  | <b>7</b>  |
| 1.1 Motivation . . . . .   | 7         |
| 1.2 Thesis Overview . . . . .  | 13        |
| <b>2 Warm Low-Level Stratified Clouds</b>  | <b>17</b> |
| 2.1 Physical Properties . . . . .  | 17        |
| 2.2 Observing Warm Low-Level Stratified Clouds . . . . .                           | 19        |
| 2.3 Modeling Warm Low-Level Stratified Clouds . . . . .                            | 29        |
| <b>3 Energy Transitions and Climate Change</b>                                     | <b>31</b> |
| 3.1 Study I: Uncertainty Estimates of Energy System Investment<br>Models . . . . . | 31        |
| 3.2 Optimal Tilt Angles of Photovoltaic Systems in Germany . . . . .               | 34        |
| 3.3 Sensitivity of Radiation Models . . . . .                                      | 34        |
| <b>4 New Opportunities for Ground-Based Remote Sensing of Clouds</b>               | <b>39</b> |
| 4.1 Publication I . . . . .  | 39        |
| 4.2 Measurement Uncertainties due to Sequential Chirp Sampling . . . . .           | 58        |
| 4.3 Dealiasing Radar Doppler Spectra . . . . .                                     | 59        |
| <b>5 Retrieving Liquid Water Content of Warm Stratified Clouds</b>                 | <b>63</b> |
| 5.1 Publication II . . . . .   | 63        |
| 5.2 Publication III . . . . .  | 71        |
| <b>6 Discussion and Outlook</b>  | <b>83</b> |
| 6.1 Uncertainty Estimates of Energy System Investment Models . . . . .             | 83        |
| 6.2 New Opportunities for Remote Sensing of Clouds . . . . .                       | 84        |
| 6.3 Retrieving Liquid Water Content of Warm Stratified Clouds . . . . .            | 86        |
| 6.4 The Big Picture and Future Visions . . . . .                                   | 90        |

|   |            |
|---|------------|
| <b>A Eigene Beteiligung an Veröffentlichungen</b> | <b>95</b>  |
| <b>Bibliography</b>                               | <b>105</b> |

*Für jene, die diesen Moment nicht mehr mit mir  
teilen können.*





# Zusammenfassung

Klimawandel und ansteigende Weltbevölkerung erhöhen den Druck auf die globale Gemeinschaft, insbesondere auf den *Globalen Norden*, drastische Veränderungen in Bezug auf Lebenseinstellung, Lebensstil und Ressourcenmanagement zu initiieren, um eine bewohnbare Umwelt zu erhalten, natürliche Risiken zu minimieren und dadurch diejenigen zu schützen, die am verwundbarsten sind und am wenigsten Verantwortung für den derzeitigen Zustand unseres Planeten tragen. Unter anderem, kommt dem Wechsel von fossilen zu erneuerbaren Energiequellen (*Erneuerbaren*) eine Schlüsselrolle zu, um unsere „hochkarbonisierte“ Gesellschaft in ein Zeitalter ohne CO<sub>2</sub>-Emissionen zu überführen. Die Integration von Erneuerbaren in existierende Energienetze oder gar die Gestaltung einer Energieversorgung, die nur auf Erneuerbaren beruht, stellen nach wie vor große Herausforderungen dar, die interdisziplinärer Forschung bedürfen. Solch eine Forschung wird an der Universität zu Köln im Rahmen des Projektes *Energy Transitions and Climate Change* durchgeführt, um sowohl sehr spezifische als auch interdisziplinäre Forschung zu betreiben, die sowohl ungelöste Probleme in Bezug auf Erneuerbare und Klimawandel untersucht und außerdem neue Fragestellungen hervorbringen soll.

In dieser Arbeit werden Resultate einer interdisziplinären Studie diskutiert, die die Unsicherheit von prognostizierten Energienetzen für Deutschland auf Grundlage von *Reanalysedaten* untersucht. Diese Unsicherheit hängt unter anderem von der Genauigkeit der berechneten Solarenergie von *Photovoltaikanlagen* ab und zeigt die größte Sensitivität gegenüber Veränderungen der direkten solaren Einstrahlung. Daraus folgt, dass zunächst die Genauigkeit von Reanalysen, die die solare Einstrahlung berechnen, bestimmt werden muss, um im Folgenden Aussagen über die Unsicherheit von prognostizierten Energienetzen treffen zu können. Fehler der direkten Solarstrahlung in Reanalysen hängen zum großen Teil davon ab, wie gut diese Wolken reproduzieren. Hierbei spielen warme, tiefe, stratiforme Wolken, die sogenannten Stratocumulus Wolken (Sc), auf Grund ihres häufigen Auftretens und ihrer hohen Rückstreuungseigenschaft von Sonnenstrahlung, eine wichtige Rolle. Damit stellt das Verständnis von Bildungs- und Entwicklungsprozessen von

Sc ein wichtiges Problem für Anwendungen im Bereich der erneuerbaren Energien dar. Um Modelle und Parameterisierungen, die z.B. in Reanalysen eingebettet sind, zu evaluieren, bedarf es akkurater Messungen von Sc, welche das Hauptthema dieser Arbeit darstellen: Wie genau können wir die vertikale Verteilung von Flüssigwasser (LWC) in warmen, tiefen, stratiformen Wolken, insbesondere Sc, unter Verwendung von bodengebundener Fernerkundung, bestimmen?

Die drei Schlüsselpublikationen dieser kumulativen Dissertation versuchen diese Frage aus verschiedenen Perspektiven zu beantworten: [Publikation I](#) evaluiert die Leistungsfähigkeit eines neuen W-Band Radar-Radiometers (JOYRAD-94), das verwendet werden kann um physikalische Eigenschaften von Sc zu bestimmen. Es wird durch einen Vergleich mit einem nebenstehenden Radar gezeigt, das JOYRAD-94 Radarreflektivitäten mit einer Genauigkeit von circa 0.5 dB messen kann. Der Vergleich brachte außerdem eine neue Methode hervor, mit deren Hilfe Radar Doppler Spektren genauer abgeleitet werden können, nämlich mit hoher vertikaler Auflösung bei einem großen Messbereich für Dopplergeschwindigkeiten. JOYRAD-94 ist außerdem mit einem passiven 89 GHz Mikrowellenradiometer (MWR) ausgestattet, das die Ableitung des integrierten Flüssigwassergehalts mit einer Genauigkeit von  $15 \text{ g m}^{-2}$  ermöglicht, sofern der integrierte Wasserdampfgehalt mit einer Unsicherheit von  $2 \text{ kg m}^{-2}$  aus einer externen Quelle bekannt ist. Passive und aktive Komponenten sind optimal aufeinander abgestimmt, da JOYRAD-94 beide Signale über die selbe Antenne empfängt. Dies stellt eine Neuheit in der bodengebundenen Fernerkundung dar. Welche Vorteile sich daraus ergeben wird in [Publikation II](#) diskutiert. Diese untersucht wie genau der LWC, unter Verwendung eines gängigen Verfahrens (von hier an *StandFrisch*), welches Radar und MWR kombiniert, und unter Berücksichtigung der horizontalen Abstand beider Geräte, bestimmt werden kann. Es wird gezeigt, dass unterschiedliche Beobachtungsvolumina beider Geräte bereits ab einem Abstand von 10 m zu einem relativen Fehler von 10 % im gesamten LWC Profil führen, welcher durch Erhöhen des Abstands auf 100 m bis auf 30 % anwächst. Des Weiteren wird deutlich, dass die Ableitung von LWC an vertikalen Wolkenrändern eine optimale Übereinstimmung der Beobachtungsvolumina bedingt, das heißt, schon bei einem Abstand von 10 m können keine vernünftigen Ergebnisse mehr erzielt werden. [Publikation III](#) untersucht die Genauigkeit von StandFrisch für verschieden zusammengesetzte Sc. StandFrisch ist anwendbar sofern sich keine Nieseltropfen in der Wolke befinden. Ist dies jedoch der Fall, ist StandFrisch nicht mehr in der Lage den LWC

korrekt zu bestimmen. [Publikation III](#) stellt deshalb eine Modifikation von StandFrisch vor, welche es erlaubt den LWC in sowohl nieselfreien also auch nieselenthaltenden Wolken mit einer Genauigkeit von 20 % abzuleiten.

Die Resultate der hier vorgestellten Publikationen erhöhen die Genauigkeit von einer gängig verwendeten Methode zur Ableitung des LWC in warmen, tiefen, stratiformen Wolken und charakterisieren außerdem die Unsicherheit dieser Methode. Damit trägt diese Dissertation dazu bei mikrophysikalische Prozesse, welche Wolkenbildung und -entwicklung beeinflussen, in Sc besser zu verstehen. Darüber hinaus kann die genaue Kenntnis des LWCs die Evaluation von Modellen und Parameterisierungen verbessern, welche z.B. in Reanalyses implementiert sind. Gut charakterisierte Modelle und deren Daten sind unabdingbar für verschiedenste Anwendungen wie z.B. Wetter- und Klimavorhersage oder das Prognostizieren von zukünftigen Energienetzen.



# Abstract

Climate change and an increasing global population increase the pressure on the global community, in particular the *Global North*, to initiate drastic changes in mindset, lifestyle and resource management to sustain a habitable environment, to minimize natural hazards, and thereby, to protect those who are most vulnerable and least responsible for the current condition of our planet. Among others, the shift from fossil to renewable energy sources (renewables) plays a key role in transforming a high-carbon society into a zero-carbon one. The integration of renewables into existing energy systems or even the design of an energy system consisting of renewables only are still challenging tasks that require interdisciplinary research. Such research is conducted by the University of Cologne hosting the project [Energy Transitions and Climate Change](#) to support both specific and interdisciplinary research for investigating open questions and creating new ones related to renewable energies and climate change.

Here, results of an interdisciplinary study are discussed investigating the uncertainty of predicted energy systems in Germany based on the analysis of *reanalysis* data. Among others, this uncertainty depends on the accuracy of estimated solar energy from *photovoltaic* panels and is most sensitive to changes in direct solar radiation. Hence, to assess the uncertainty of predicted energy systems based on reanalysis data, the accuracy of the latter itself, especially estimated solar radiation, must be characterized well. Uncertainties in direct solar radiation in reanalysis data depend to high extent on the prediction of clouds, especially those clouds that are abundant and have a high albedo at visible wavelengths such as stratocumulus clouds (Sc). Thus, understanding their formation and evolution constitutes an important topic for renewable energy applications. To evaluate models and parameterizations implemented into reanalysis, accurate observations of Sc are necessary, which is the main topic of this work: how accurately can we retrieve the liquid water content (LWC) of warm low-level stratified clouds, in particular Sc, using ground-based remote sensing?

The three key publications of this cumulative thesis try to answer this question from different perspectives: [Publication I](#) evaluates the performance

of a new W-band radar-radiometer (JOYRAD-94) that can be used to derive physical properties of clouds. It is shown, by comparing JOYRAD-94 to a co-located radar, that it is capable of measuring radar reflectivity at 94 GHz with an accuracy of about 0.5 dB. The comparison also revealed a new method to *dealias* radar Doppler spectra using two co-located radars enabling cloud observations with both high vertical resolution and large unambiguous Doppler velocity. Additionally, JOYRAD-94 is equipped with a passive microwave radiometer (MWR) channel at 89 GHz enabling the retrieval of the liquid water path with an uncertainty of about  $15 \text{ g m}^{-2}$  when the integrated water vapor is known with an accuracy of  $2 \text{ kg m}^{-2}$  from an external source. Optimal beam matching between the radar and the radiometer of JOYRAD-94 is accomplished by receiving the active and passive signals over the same antenna. This is a novelty in ground-based remote sensing. The advantage of optimally matched beams for cloud remote sensing is discussed in [Publication II](#) that investigates how the accuracy of a commonly used LWC retrieval (henceforth *StandFrisch*), combining radar and MWR, changes when the instruments are displaced to each other, i.e. observe different cloud scenes. It is found that displacing the instruments by 10 m increases the relative retrieval uncertainty of retrieved LWC by 10 % in the entire profile. At 100 m displacement, the relative error reaches 30 %. Moreover, it is shown that studying LWC at cloud edges requires optimally matched beams, i.e. a displacement by 10 m does already yield unreasonable results. [Publication III](#) assess the accuracy of *StandFrisch* for various compositions of Sc. *StandFrisch* is capable of retrieving LWC in non-drizzling Sc. However, once drizzle is present, *StandFrisch* does not obtain reasonable estimates of LWC. [Publication III](#) provides a modification of *StandFrisch*, the *ModFrisch*, that allows retrieving LWC in both drizzling and non-drizzling Sc with an accuracy of 20 %.

The findings of the three publications increase the accuracy of a commonly used LWC retrieval technique for warm low-level stratified clouds and characterize the retrieval's uncertainties. Therefore this thesis makes an important contribution to better understand micro-physical processes in Sc, which drive cloud formation and evolution. Moreover, more accurate LWC profiles can help to improve the evaluation of models and their parameterizations, which are, for example, implemented in reanalysis data. Well characterized models and their data are inevitable for various applications such as weather and climate predictions, as well as estimating future energy systems.

# Chapter 1

## Introduction

### 1.1 Motivation

Climate change is one of the biggest challenges humanity is currently facing (IPCC, 2014). Its consequences can already be observed and many predicted changes in our climate system are not promising: the intensification of droughts (Teuling, 2018), more extreme precipitation events and floods (Madsen et al., 2014), an increased occurrence frequency of *El Niño* events (Cai et al., 2014) or an increased risk of extreme heat waves (Herring et al., 2014). A second challenge that we are facing is the continuous growth of the global population. Current predictions estimate a global population of about 10 billion people by 2050 (Gerland et al., 2014). This implies a drastic increase in the consumption of natural resources, especially, when considering that highly populated countries from the *Global South*, such as China or India, are catching up with the habits and lifestyles of the *Global North*. IPCC (2014) showed that if we do not modify our lifestyle, a continuous increase of the global population will foster climate change and make the ambitious goals of the *Paris Agreement* of 2015 (UNFCCC, 2015) unachievable. Therefore the *United Nations* defined seventeen *Sustainable Development Goals* (SDG; United Nations, 2017) whose achievement is supposed to preserve a habitable planet and to respect the human rights of those who are most vulnerable. Among others, the SDGs aim to expunge hunger, establish gender equality and provide affordable and clean energy.

Currently, the cleanest energy sources are renewable energy sources (renewables), such as wind and solar energy. Both have great potential to substitute the majority of climate-damaging coal power plants (Delucchi and Jacobson, 2011); however, due to their fluctuating nature, their integration into

the existing energy systems<sup>1</sup> is still challenging (Lorenz et al., 2011). Moreover, accurate and spatially highly-resolved climate predictions of available solar and wind energy in the future are necessary to increase the interest for large scale investments by the private sector and to help policy makers in taking sustainable decisions (Dowling, 2013). The prospective structure of energy systems depends on demand and available technologies in the future and on political decisions such as a zero-CO<sub>2</sub> emission scenario by 2050 to mitigate climate change (Rockström et al., 2017), but also on the investments into renewables today (Uyar and Beşikci, 2017). Decisions on investments are often based on energy system investment models (ESIM) that predict future energy systems optimizing (among others) energy demand, investment costs and available renewable energy (Kaundinya, Balachandra, and Ravindranath, 2009). However, uncertainty estimates of ESIMs based on the meteorological input data are sparse in the literature and therefore represent an important field of research.

Highly-resolved long-term reanalysis data, such as the *COSMO Reanalysis* with 6 km horizontal resolution (COSMO-REA6; Bollmeyer et al., 2015), provides an excellent opportunity to quantify available solar and wind energy and their uncertainties on time-scales of decades with high spatial resolution. Therefore reanalysis data has been used in numerous climatological applications (Bengtsson, Hagemann, and Hodges, 2004; Hersbach et al., 2017), and has also gained interest in applications of ESIMs (Langodan et al., 2016; Zhang et al., 2018). Reanalyses are the best estimate of the atmospheric state created by combining models and observations (Wahl et al., 2017). Both models and observations are associated with uncertainties that lead to uncertainties in reanalysis products, such as solar radiation that depends on how clouds are parameterized within the model (Bollmeyer et al., 2015). Thus, accurate cloud observations are needed to evaluate models and parameterizations in which clouds are in general still a major uncertainty source (Dufresne and Bony, 2008).

Different cloud types influence different components of the Earth's radiation budget: at visible wavelengths, warm low-level stratified clouds play an important role. They cover approximately 30-40 % of the Earth's surface (Wood, 2015; Rossow and Schiffer, 1999) and are strongly reflecting. Thereby,

---

<sup>1</sup>The term *energy systems* refers to the spatial distribution of installed power plants, i.e. where is how much capacity of wind, solar, coal, nuclear or gas power installed.



stratocumulus clouds (Sc), the most common kind of warm low-level stratified clouds, contribute to 20 % of annual mean cloud coverage. Consequently, Sc are very important for the climate system, which is described by Wood (2012) stating:

*"Only small changes [...] of Sc clouds are required to produce a radiative effect comparable to those associated with increasing greenhouse gases [...]"*

Besides their impact on the global radiation budget, Sc influence local parameters such as available solar energy. Figure 1.1 illustrates the annual mean coverage of Sc. It shows that regions in which most energy is currently consumed and where most resources are invested into renewables, e.g. Europe or China (Frankfurt School-UNEP, 2018), exhibit cloud coverages of 10 to 40 %. Because of the need of accurate predictions of the Earth's radiative balance and available solar energy in the future

*"[u]nderstanding why, where, when, and how stratocumuli form, and being able to quantify their properties, therefore constitutes a fundamental problem in the atmospheric sciences." (Wood, 2012)*

One parameter that characterizes Sc is the *liquid water content*<sup>2</sup> (LWC [ $\text{kg m}^{-3}$ ]). The evolution of LWC depends on environmental parameters such as humidity and temperature profiles, adiabaticity of the lifting process and air turbulence (Houze, 2014b). The relationship between the LWC, the cloud droplet number concentration ( $N$  [ $\text{m}^{-3}$ ]), and the particle size distribution (PSD) determine the extinction properties of liquid clouds (Houze, 2014a), e.g. how much solar radiation is reflected back into space. Thus, it is important to quantify the vertical distribution of liquid in Sc.

There are two main approaches, each subdividing into various methods, to measure the LWC: in-situ observations, such as particle counters that are mounted on balloons or airplanes (Vidaurre, Hallett, and Rogers, 2011; Chen et al., 2018) and remote sensing measuring radiative properties of clouds (Atlas, 1954; Fielding et al., 2014). In-situ air-borne observations are in general more accurate because the PSD is directly measured; however, instantaneous profiling of the vertical column is difficult because balloons rise to slow and airplanes are associated with large horizontal velocities (Wang et al., 2012). Thus, to obtain profiles from balloon and airplane measurements steady-state and horizontal homogeneity are required, respectively. In contrast, satellite and ground-based remote sensing is capable of profiling clouds with

---

<sup>2</sup>The LWC is used to describe the vertical distribution of liquid within the cloud.

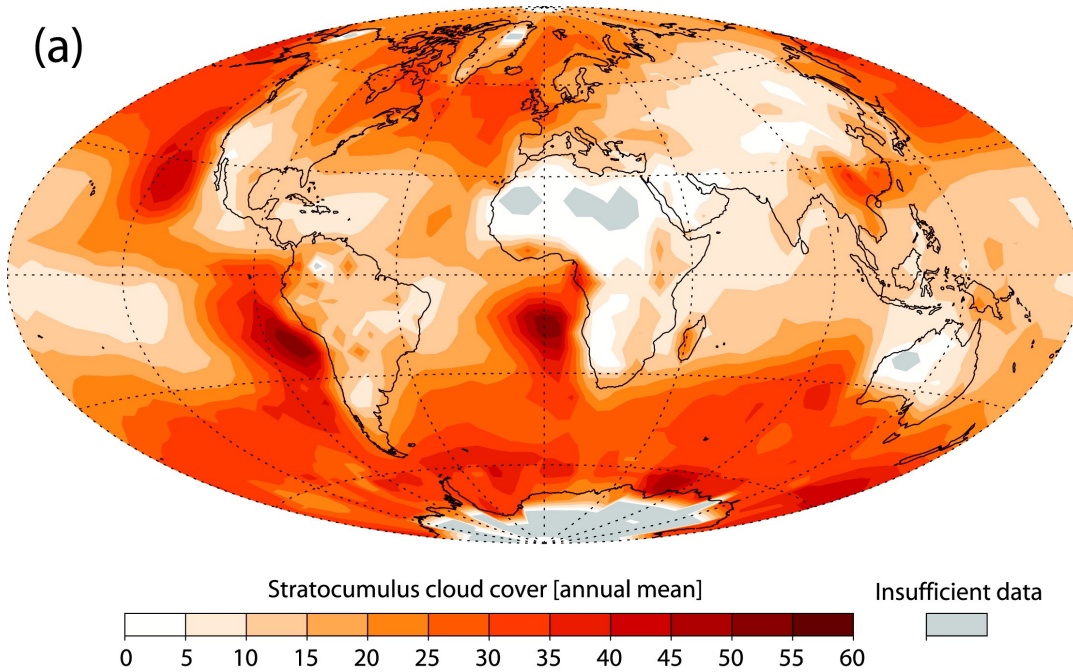


FIGURE 1.1: "(a) Annual mean coverage of stratocumulus clouds. Data are from the combined land–ocean cloud atlas database (Hahn and Warren 2007)." (Wood, 2012)

temporal resolutions of seconds (Marchand et al., 2008; Wang et al., 2017). Moreover, most instruments operate automatically and are therefore more practical when recording long-term data sets at a certain location. The disadvantage is that obtaining cloud properties from radiative measurements is an inverse problem that is often ill-posed meaning that assumptions must be made on the expected properties of the cloud (Löhnert et al., 2008). Satellites provide data with large spatial, sometimes global, coverage that can be used to create global maps of atmospheric properties (e.g. Fig. 1.1). However, temporal<sup>3</sup> and vertical resolution is poor in comparison to ground-based sensors. This is particularly problematic if the evolution of cloud properties is investigated, especially, for those processes that happen on small temporal (seconds to minutes) and spatial (a few meters) scales, such as rain production (Stephens and Haynes, 2007) or entrainment of air at cloud top (Rooy et al., 2013), both affecting LWC.

A commonly used setup of instruments is to combine a *radar* (**R**adio **D**etection and **R**anging) with a microwave radiometer (MWR) (e.g. Illingworth et al., 2007; Zhao et al., 2012). The former provides information on the vertical distribution of liquid water and the latter can obtain the liquid water path (LWP

<sup>3</sup>only for non-geostationary satellites

[ $\text{kg m}^{-2}$ ]), i.e. the total amount of liquid in the observed column. Often a *lidar* (**L**ight **D**etection and **R**anging) is additionally used to determine cloud base, which is often missed by the radar due to missing sensitivity. The basis of deriving LWC from radar is that the radar backscatter signal (henceforth radar reflectivity factor  $Z_e$ ) is proportional to the 6<sup>th</sup> power of the scattering particle's diameter in the Rayleigh scattering-regime (Petty, 2006, p. 379), thus, the LWC can be related to  $Z_e$  using a power law (Atlas, 1954). Yet, a simple power law relation is associated with large uncertainties reflected in a large variety of proposed relations in the literature (Atlas, 1954; Sauvageot and Omar, 1987; Fox and Illingworth, 1997; Wang and Geerts, 2003; Kogan, Kogan, and Mechem, 2007). To decrease retrieval uncertainties, the LWP can be used to constrain the total amount of liquid (Frisch, Fairall, and Snider, 1995; Frisch et al., 1998). Frisch et al. (1998) showed that under certain conditions (see section 2.2.6), the square root of  $Z_e$  can be directly used to distribute the LWP over the vertical column. On the one hand, these assumptions make retrieving LWC simple leading to a regular use of this approach<sup>4</sup> in the remote sensing community (Zhao et al., 2012). On the other hand, the retrieval is strongly constrained: for instance, it does not work once drizzle is present in the cloud, which is frequently the case in Sc (Stevens et al., 2003). Other techniques face similar difficulties (Fox and Illingworth, 1997; Baedi et al., 2000), so that the robust retrieval of LWC under various conditions remains an important problem that needs to be solved.

In addition to reliable retrievals, accurate observations are needed for reasonable results. The LWP is obtained from brightness temperature (BT [K]) measurements between 20 and 90 GHz (e.g. Crewell et al., 2001; Gaffard and Hewison, 2003; Kuchler et al., 2017) with an accuracy of 15-30  $\text{g m}^{-2}$ , depending on instrument noise and calibration accuracy (Löhnert and Crewell, 2003; Hewison and Gaffard, 2007; Turner et al., 2007; Maschwitz et al., 2013). In contrast to MWR measurements, radars are generally associated with uncertainties of up to several decibels (dB) (e.g. Hogan et al., 2003; Li et al., 2005; Merker et al., 2015). For some LWC retrievals, such as Frisch et al. (1998) or differential attenuation approaches (e.g. Hogan, Gaussiat, and Illingworth, 2005), correctly calibrated radars are not required; yet, there are many applications that need radar measurements with high accuracy, such as retrieving LWC using a power law relation (Atlas, 1954). Two different types of radar

---

<sup>4</sup>or a modified version

technologies are commonly used: pulsed systems (Doviak, Zrnić, and Sirmans, 1979; Clothiaux et al., 1995; Görsdorf et al., 2015) that transmit several pulses of high power (some kW) and *frequency modulated continuous wave* (FMCW) radar transmitting a continuous signal with a few Watts (Strauch, 1976; Yamaguchi et al., 2009; Huggard et al., 2008; Bennett et al., 2009; Thies et al., 2010; Delanoë et al., 2016). Both types are associated with advantages and disadvantages that are discussed in more detail in [Publication I](#) where a new FMCW radar is introduced. Besides the uncertainties that are associated with the instruments themselves, synergetic observations are associated with a further error source: instruments are mostly not located exactly at the same place, but rather displaced by a few meters. This constitutes a further uncertainty source due to potentially different conditions in the observed volumes, which is a known problem but is mostly not quantified (Frisch et al., 1998; Kneifel et al., 2016).

This introduction began with climate change and ended with synergetic observations. In between, reanalysis and renewables, uncertainty estimates in ESIMs and global cloud cover, liquid water content and retrieval assumptions, LWP measurements and new radar technology have been discussed. This shows, how many specific aspects a global topic like climate change has and how deep one can dive into details of which even the last detail might be of great importance to complete the puzzle. Such a complexity requires both specialized and interdisciplinary research while the latter is in particular important for obtaining the big picture (Nature Editorial, 2016). Within the *DFG Excellence Initiative*, the University of Cologne hosts the project *Energy Transitions and Climate Change* (ET-CC) to support both specific and interdisciplinary research for investigating open questions and creating new ones related to renewable energies and climate change. ET-CC is an interdisciplinary cooperation between several public institutions, such as the *Institute of Energy Economics* and the *Institute for Geophysics and Meteorology* of the University of Cologne. In the framework of ET-CC, the following topics are investigated in this thesis: (i) using reanalysis data to estimate uncertainties in ESIMs ([Study I](#)); (ii) evaluating a new FMCW radar-radiometer for studying cloud processes ([Publication I](#)); (iii) investigating how the measurement setup influences LWC retrieval uncertainties ([Publication II](#)); and providing a new retrieval approach to determine LWC in both drizzling and non-drizzling conditions ([Publication III](#)).

Trying to solve the entire puzzle would have been presumptuous, yet, I hope that I can provide some puzzle pieces, although, they might be from

different corners. The next section contains an overview about the studies and the outline of this thesis. This thesis is cumulative relying on three publications ([Publication I](#), [Publication II](#), [Publication III](#)) with a specific focus on cloud remote sensing and is framed by an interdisciplinary study ([Study I](#)) on renewable energy applications. I hope you will enjoy reading this work as much as I enjoyed writing this introduction.

## 1.2 Thesis Overview

ESIMs generally use a time series of *representative days* that should cover possible extreme events<sup>5</sup> (e.g. Nahmmacher et al., 2016). Thereby, the number of days is restricted to about a dozen, because ESIMs are computationally expensive. This simplification implies uncertainties; however, uncertainty estimates of such clustering techniques, in particular based on biases in the input data, have not yet been investigated. [Study I](#) investigates uncertainties of ESIMs, based on biases of meteorological input data, such as solar radiation and wind speed: first, the biases of solar radiation and wind are obtained from comparing the 20 years reanalysis data set COSMO-REA6 (Bollmeyer et al., 2015) to observations. Then, the initially selected representative days are disturbed by the the found biases, which leads to differences in the ESIM output, e.g. the share of renewable energy production in the modeled energy systems. [Study I](#) can be considered as an example of why accurate observations of cloud properties are necessary. The analysis investigates how biased reanalysis data, which can be evaluated with independent observations, affects the results of ESIMs. To the authors' knowledge, this is the first study that provides uncertainty estimates for predicted energy systems. Moreover, the comprehensive analysis in [Study I](#) implies that currently used approaches to estimate solar and wind energy generation over larger areas, such as Germany, might be insufficient and therefore provides a promising approach based on reanalysis data.

The findings in [Study I](#) lead directly to questions that are associated with accurate cloud observations: how accurate are reanalyses? What is the best way to evaluate reanalyses? What is required for a comprehensive evaluation? Certainly, there are many more questions arising from [Study I](#), of which many are directly or indirectly related to the observation of clouds. Therefore

---

<sup>5</sup>E.g. no wind and no solar energy availability or maximum wind and solar energy availability.

**Study I**, directly related to the **ET-CC** project, frames the three key publications of this work as illustrated in Fig. 1.2. The three key publications are all connected by the following question:

*How can liquid water content profiles be observed accurately?*

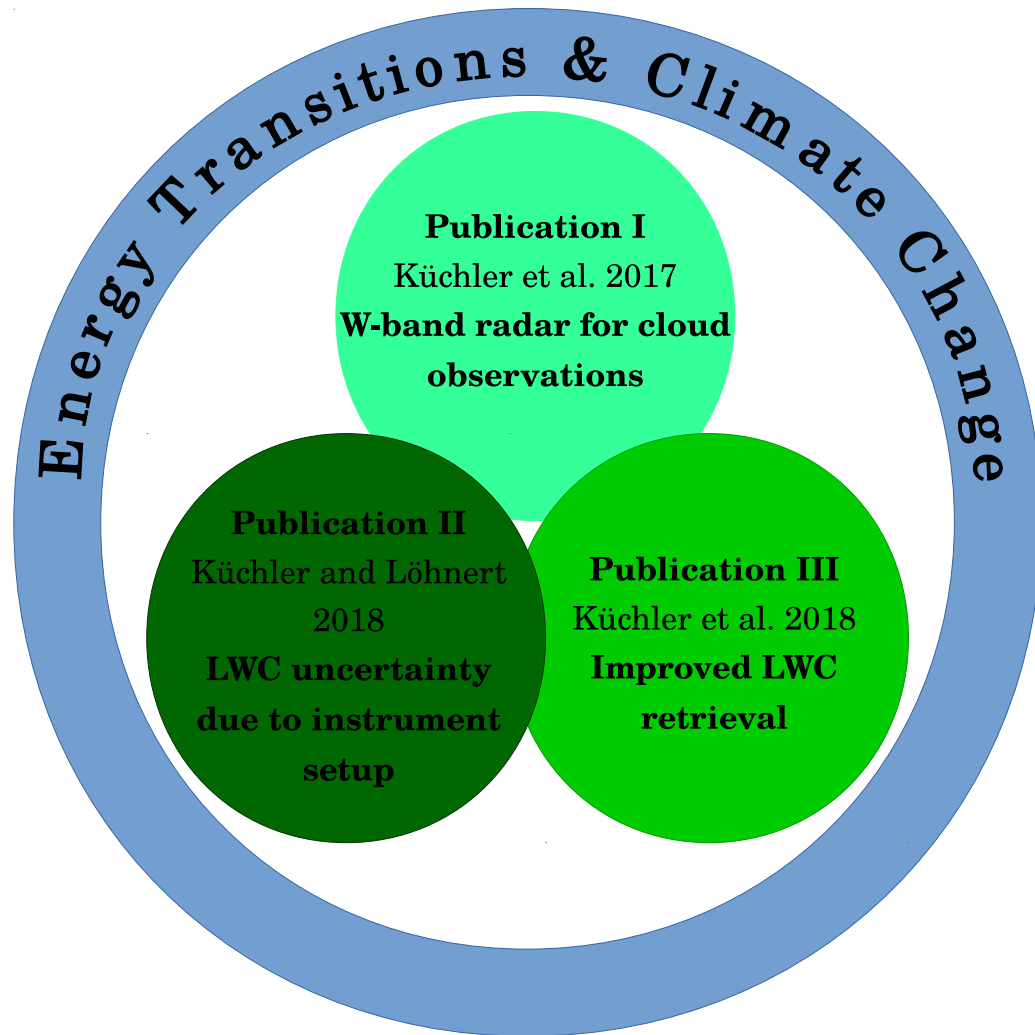


FIGURE 1.2: Schematic overview of the studies. Key publications are the studies in green motivated by the broader context of the project *Energy Transitions and Climate Change*.

**Publication I** gives an answer from the engineering perspective. The study introduces and evaluates a new W-band<sup>6</sup> radar-radiometer that provides a novelty in ground-based remote sensing: the instrument combines passive and active microwave remote sensing using the same antenna, i.e. both

<sup>6</sup>In general, the *W-band* refers to the frequency band between 75 to 110 GHz.

components observe the same scene. Moreover, it is shown that the radar-radiometer is capable of recording climatological data sets of cloud properties that help to quantify model uncertainties based on robust statistics (Illingworth et al., 2007). Additionally, [Publication I](#) presents a new method that improves Doppler spectra processing when two co-located radars are measuring simultaneously. Improved Doppler spectrum processing with high vertical resolution provides the opportunity to investigate micro-physical processes at cloud edges, such as entrainment (Wood, 2012; Babkovskaia et al., 2015), and in the melting layer (Giangrande et al., 2016), which strongly influence the thermodynamic structure of clouds.

[Publication II](#) approaches the question from the perspective of an experimental meteorologist: LWC profiles are most commonly obtained by combining radar and MWR following Frisch, Fairall, and Snider (1995) or Frisch et al. (1998) (Zhao et al., 2012); however, no investigations have been made on what impact the horizontal distance between the radar and the MWR has on the retrieval accuracy. [Publication II](#) investigates the uncertainty that is introduced by combining radar and MWR while considering the horizontal distance and thereby the different scenes that the instruments observe. Thus, [Publication II](#) is directly connected to [Publication I](#) that presents an instrument that combines radar and MWR using the same antenna. The findings from [Publication II](#) are transferable to any remote sensing application that uses more than one instrument with high temporal resolution. Moreover, bias analyses between models and observations, such as autoconversion schemes (Wood, 2005), may yield different results when considering sensor displacement as an additional uncertainty source.

[Publication III](#) tries to answer the question by evaluating the applicability of the retrieval by Frisch et al. (1998) and thereby connects to [Publication I](#) and [Publication II](#). The study investigates the accuracy of Frisch et al. (1998) under the presence of drizzle and yields a promising improvement under drizzling conditions. This does not only provide more accurate profiles of LWC, but can also help to understand retrieval biases in passive and active remote sensing (e.g. Frisch, Fairall, and Snider, 1995; Cadeddu et al., 2017). Furthermore, enhancing the knowledge on the vertical structure of warm low-level stratified clouds improves the estimation of the Earth's radiation budget (Stephens, Paltridge, and Platt, 1978; Slingo, 1990), the quantification of parameterization schemes (Zhang et al., 2005), the understanding of the relation between small scale cloud-processes and the general circulation (Wood et al., 2011), and the theory of how boundary fluxes (at the cloud base

and top) and precipitation affect cloud adiabaticity (Wood, 2012).

In addition to the theory discussed in the publications, chapter 2 gives an overview about physical properties of warm low-level stratified clouds, including formation and evolution, micro-physics, and interaction with microwave radiation. Moreover, FMCW radar theory is discussed in detail, which is the basis for all retrieval techniques applied here. Note that a detailed theoretical background for [Study I](#) (contained in chapter 3) is not provided, because [Study I](#) is not the main focus of this work and can rather be seen as extended motivation. Since [Study I](#) is an interdisciplinary study that is currently in preparation, chapter 3.1 provides a more detailed discussion of the work I contributed to this study. [Publication I](#) is presented in chapter 4 including supplementary material and discussions. Chapter 5 contains [Publication II](#) and [Publication III](#). The final chapter concludes with a discussion and an outlook.



## Chapter 2

# Warm Low-Level Stratified Clouds

### 2.1 Physical Properties

In the following the basic concepts of the formation and evolution of warm<sup>1</sup> low-level stratified clouds are briefly discussed, also considering micro-physical processes that are associated with different cloud stages.

#### 2.1.1 Formation and Evolution

Both stratus clouds (St) and Sc form "*under conditions of large-scale subsidence and strong lower-tropospheric static stability*" (Wood, 2015). Unlike Sc, St are normally not associated to deep convection, and can be formed by advection of warm air over cold surfaces, by lifted air-masses starting to condense or by lifted fog layers. Usually, St are of transient nature due to long-wave (LW) radiative cooling at cloud top triggering turbulence and thereby transforming into Sc (Wood, 2015).

Sc develop typically at the top of the well-mixed boundary layer where LW radiative cooling of the clear boundary layer induces condensation of turbulent plumes that are generated by buoyancy and wind. They are maintained by cloud top LW radiative cooling sustaining buoyant generation of turbulence that deepens the cloud layer (Houze, 2014b). During day time, cloud top LW cooling is partially compensated by solar absorption, which is why the maximum Sc cloud cover typically occurs before sunrise (Bergman and Salby, 1996). Entrainment of dry and warm air from the free-troposphere aloft deepens and tends to dilute the stratified cloud layer (Lilly, 1968) and thereby weakens the mixing of air-parcels from cloud top down to the surface. The Sc layer becomes decoupled from the surface moisture supply and

---

<sup>1</sup>Clouds that have a temperature larger than 0°C and contain only liquid water are called "warm" clouds.

turns into a cumulus-dominated cloud field enhancing surface forcing and triggering further convection (Wood, 2012).

The vertical distribution of LWC in Sc has been shown to increase almost linearly in marine environments. Moreover, their structure is frequently close to adiabatic (Nicholls, 1989; Miles, Verlinde, and Clothiaux, 2000; Wood, 2005; Zuidema et al., 2005). However, initiation and evolution of drizzle<sup>2</sup> can lead to subadiabatic profiles, especially, in heavy drizzling conditions when the replenishment of moisture cannot compensate moisture removal by precipitation (Nicholls and Leighton, 1986; Gerber, 1996). The structure of LWC in continental Sc is more variable compared to marine Sc due to a wider range of turbulent conditions and is often subadiabatic (Kim, Klein, and Norris, 2005).

### 2.1.2 Cloud Micro-Physics

Cloud droplets form in general under heterogeneous nucleation that allows droplet formation at supersaturations of a few percent (McFiggans et al., 2006). Water vapor molecules condensate on solvable or insoluble *cloud condensation nuclei* (CCN) lowering the equilibrium vapor pressure over the (solution) droplet's surface compared to a pure water droplet<sup>3</sup> of the same size. Until the droplet reaches its critical radius, further growth requires an increase of supersaturation. At the critical radius a droplet becomes activated and grows further without the need of an increasing supersaturation. The critical radius depends on the chemical composition, i.e. the fraction of solvable material, of the CCN (McFiggans et al., 2006). The concentration of CCN varies regionally depending on the availability of sources. CCN are divided into primary sources such as sea spray, wind-generated dust, forest-fires, or industrial operations, and secondary sources being atmospheric gaseous constituents that are converted by chemical processes such as photochemical reactions (Rogers and Yau, 1989, p. 89-90).

Droplets grow due to different mechanisms: growth by diffusion being the condensation of water vapor molecules on the droplet and collection being the merging of droplets (Lamb and Verlinde, 2011). Whereas diffusion depends on environmental pressure, temperature and humidity, collection is a stochastic process determined by the collision and coalescence efficiencies

---

<sup>2</sup>There is no sharp definition of drizzle. In literature threshold diameters between 30 and 60  $\mu\text{m}$  can be found.

<sup>3</sup>The formation of a pure water droplet is called homogeneous nucleation, is initiated by random collisions of water vapor molecules and requires supersaturations of several hundred percent.

of cloud droplets. Collection can be described with the *stochastic collection equation* that considers parameters such as size, fall velocity, LWC and air-turbulence (Rogers and Yau, 1989, p. 124).

In the beginning droplets grow by diffusion until a threshold diameter is exceeded ( $\approx 30 \mu\text{m}$ )<sup>4</sup> at which size the collection process starts to dominate. During the collection process, droplets grow much faster than during diffusion (Beard and Ochs, 1993). Although, drizzle development by diffusion takes about an hour or more, drizzle and rain formation can take place in less than half an hour (Stephens and Haynes, 2007), which is a process that has not yet been fully understood (Acquistapace, 2016, p. 16). The collection process is subdivided into autoconversion and accretion. The former refers to merging of equally sized droplets, which happens in the early stage of drizzle development. The latter describes the collection of smaller cloud droplets while larger drizzle drops begin falling through the cloud (Rogers and Yau, 1989, p. 141).

Although the number concentration ( $N$ ) of drizzle drops is in general several magnitudes smaller than that of cloud droplets, drizzle plays an important role in cloud thermodynamics and in cloud remote sensing: drizzle development and precipitation removes cloud water, which can lead to subadiabatic and even non-linear LWC profiles if turbulent fluxes cannot replenish cloud condensate sufficiently (Wood, 2005). Furthermore, drizzle leads to cooling below cloud base due to evaporation inducing turbulence. Despite its small  $N$ , and thereby negligibly contributing to LWC, drizzle strongly masks radar scattering signals due to its size, which complicates the retrieval of LWC in drizzling clouds (see sections 2.2.1 and Publication III).

## 2.2 Observing Warm Low-Level Stratified Clouds

In this section, the two main observational concepts, which are used in this work, are discussed: passive microwave radiometry and radar<sup>5</sup>. Both depend on the interaction between microwave radiation and cloud particles, which is briefly discussed in the following, too.

---

<sup>4</sup>Therefore  $30 \mu\text{m}$  are sometimes used as threshold to discriminate between cloud droplets and drizzle.

<sup>5</sup>also known as active microwave radiometry

### 2.2.1 Interaction with Microwave Radiation

Di-electric extinction properties, i.e. (back-) scattering and absorption (emission)<sup>6</sup>, of a hydro-meteor<sup>7</sup> depend on its phase, shape, size, density, temperature and the frequency ( $f$ ) at which extinction is investigated (Petty, 2006). Here, the focus will be on emission and backscattering properties of hydro-meteors at microwave frequencies between 1 and 100 GHz. Figure 2.1 shows a microwave extinction spectrum for a cloudy scene at frequencies between 1 and 100 GHz. The extinction coefficient is mainly determined by absorption/emission as scattering by cloud droplets can be neglected at these frequencies (Petty, 2006, p. 346), in particular at lower microwave frequencies. At higher frequencies, scattering by larger droplets or drizzle of radiation emitted by cloud particles must be accounted for in the measurements (Cadeddu et al., 2017). The spectrum illustrated in Fig. 2.1 is dominated by the water vapor continuum, the liquid water continuum, the pressure broadened water vapor rotational absorption line at 22.235 GHz and the pressure broadened rotational absorption complex of oxygen at 60 GHz (Löhnert and Crewell, 2003). Contributions from other atmospheric constituent such as nitrogen and ozone contribute negligibly. Measuring microwave emissions at multiple frequencies allows to retrieve atmospheric properties such as temperature profiles, the integrated water vapor (IWV [ $\text{kg m}^{-2}$ ]) or the LWP. The latter will be discussed in more detail in section 2.2.5.

Although scattering is mostly negligible for passive remote sensing (see above), where absorption dominates extinction, active microwave sensors, i.e. radars, use the back-scattering properties of hydro-meteors. Radars transmit signals with high power producing a measurable back-scattered signal that is directly related to the back-scattering cross-section  $\sigma_B$  [ $\text{m}^2$ ] of the particles. For zenith-pointing radars, cloud droplets and drizzle appear as spheres and their backscattering properties can be described by *the Mie theory* (Mie, 1908). The back-scattering cross-section of particles with a diameter  $D$  [m] much smaller than the observed wavelength  $\lambda$  ( $D \ll \lambda$ ) can be described by a special case of the Mie theory, the so-called *Rayleigh-scattering regime* (Petty, 2006, p. 355):

$$\sigma_B = \frac{\pi^5 |K_w|^2 D^6}{\lambda^4} \quad (2.1)$$

<sup>6</sup>Kirchhoff's radiation law states that a body emits radiation as efficient as it absorbs it at given frequency (Petty, 2006, p. 126).

<sup>7</sup>*Hydro-meteor* is a governing term for water particles, such as rain, cloud droplets or ice particles, in the air.

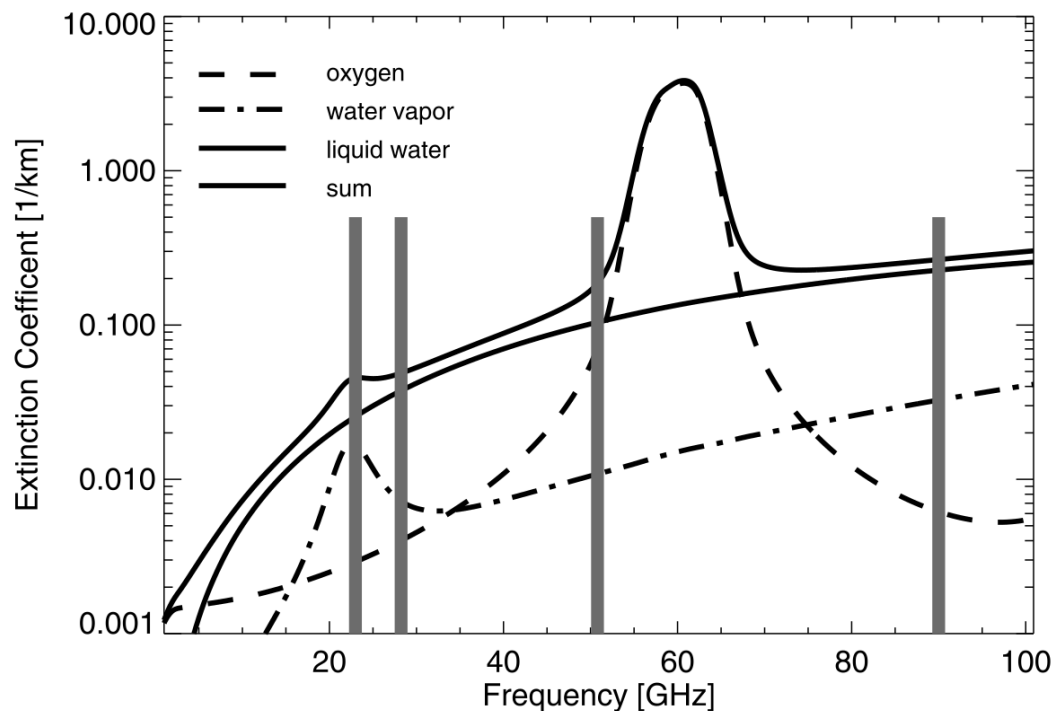


FIGURE 2.1: "Microwave extinction due to water vapor, oxygen, and typical cloud liquid water content of  $0.2 \text{ g m}^{-3}$  at 895 hPa. [...]" Source Löhnert and Crewell (2003).

where  $K_w$  depends on the dielectric properties of the particle<sup>8</sup>. Rayleigh-scattering applies for cloud droplets and drizzle when probing with frequencies between 1 and 50 GHz. At higher frequencies, Rayleigh scattering can become invalid for drizzle, depending on drop size and frequency. Moreover, absorption by liquid water must be taken into account at higher frequencies when analyzing the return signal (Hogan, Gaussiat, and Illingworth, 2005).

### 2.2.2 Passive Microwave Radiometry

The main components of a direct detecting MWR, as presented in Publication I, are depicted in Fig. 2.2. In direct detecting systems, no manipulations are done on the incoming signal before it reaches the detector<sup>9</sup>. The reflector focuses the incoming radiation into the horn antenna where the signal is coupled into the transmission line. The signal is split by band-pass filters

<sup>8</sup>The index "w" in  $K_w$  stands for "liquid water" to be consistent with the notation in Publication I.

<sup>9</sup>In superheterodyne receivers the incoming signal is converted by a local oscillator into a *intermediate frequency* (IF) simplifying signal processing (Armstrong, 1921). This architecture is implemented in the radar-system presented in Publication I.

into the according frequency channels before detectors convert the signals into voltages (Ulaby, Moore, and Fung, 1981, p. 363).

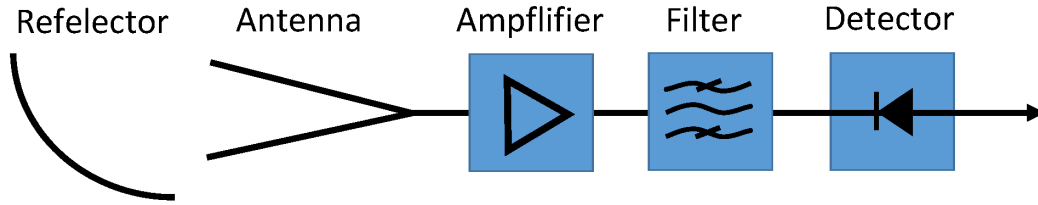


FIGURE 2.2: Schematic illustration of the receiver chain of a direct detecting radiometer. Source (Küchler et al., 2016).

The total power  $P_r$  [W] received by a MWR is determined by the power delivered by the scene  $P_{sc}$  and the instruments' noise power  $P_N$ :

$$P_r = P_{sc} + P_N \quad (2.2)$$

In the Rayleigh-Jeans regime (where  $hf \ll k_B BT$ )<sup>10</sup>, the  $P_{sc}$  and  $P_N$  can be expressed in terms of Planck-equivalent brightness temperatures (BT [K]) (Ulaby and Long, 2014, p. 272)

$$P_r = k_B(BT_{sc} + BT_N) \quad (2.3)$$

Expressing the power of the scene in terms of BT is convenient, because BTs already include the frequency dependence of the scene's radiative properties simplifying a qualitative comparison of observations at different frequencies.

The performance of a MWR can be described by its accuracy and precision. The accuracy is determined by the quality of the absolute calibration. The MWRs used in this work are typically calibrated with a so-called *liquid-nitrogen calibration* that was found to provide an accuracy of approximately 0.5 - 1 K (Maschwitz et al., 2013; Küchler et al., 2017). The precision (also known as sensitivity) depends on gain fluctuations, system noise, integration time and receiver bandwidth (Reeves, Ansons, and Landen, 1975, p. 518).

### 2.2.3 Frequency Modulated Continuous Wave Radar

Vertical structure of clouds can be obtained by using active remote sensing such as radar (Kollias et al., 2007; Kneifel, Kulie, and Bennartz, 2011; Luke and Kollias, 2013; Tridon and Battaglia, 2015; Acquistapace et al., 2017). Two

<sup>10</sup>with Planck's constant  $h$  and Boltzmann's constant  $k_B$

technologies are currently available: pulsed systems and FMCW radars. The former transmit a pulse of microwave radiation and measure the delay time and the strength of the return signal (Doviak, Zrnić, and Sirmans, 1979). In contrast, FMCW radar transmits continuously while changing the frequency, a so-called *chirp* (Strauch, 1976).

Millimeter FMCW radars are suitable to obtain information on cloud micro-physics such as the vertical distribution of hydro-meteors (e.g. Lhermitte, 1987; Delanoë et al., 2016). Section 4.1 presents one key publication of this thesis (Publication I), introducing a new W-band FMCW radar-radiometer. Publication I contains basic principles of FMCW radar theory; however, explanations are very brief. Therefore, a more detailed description of FMCW radar theory is given here.

Figure 2.3 shows the principle of FMCW radar using a saw-tooth chirp for a steady particle<sup>11</sup> at distance  $R$  [m]. The transmission frequency is continuously<sup>12</sup> increased spanning the bandwidth  $B$  [Hz] over the chirp duration  $T_c$  [s]. The transmitted signal ( $s_t$  [W]) is reflected at distance  $R$  leading to the time shift

$$\Delta t = \frac{2R}{c}, \quad (2.4)$$

with  $c$  being the propagation velocity of the electro-magnetic wave. Hence, the difference  $f_{IF}$  [Hz] between the transmitted and received signal ( $s_r$  [W]) is constant over the entire chirp and  $f_{IF}$  can be expressed via

$$f_{IF} = \frac{2R}{c} \frac{B^*}{T_{samp}}. \quad (2.5)$$

where  $B^*$  is the actual bandwidth used over the effective sampling time  $T_{samp}$ .

The  $f_{IF}$  signal is obtained from mixing  $s_t$  and  $s_r$ , which is mathematically a multiplication of both signals. The signal at the detector output  $s_d$  is composed of two periodic contributions: one being composed out of the sum of the phases of  $s_t$  and  $s_r$  and the other out of their difference, i.e.  $f_{IF}$  (Strauch, 1976, p. 13). The former is filtered out leading to

$$s_d \propto \sin(f_{IF}) \quad (2.6)$$

Usually,  $s_t$  is backscattered at several distances leading to a superposition

<sup>11</sup>The influence of Doppler shifts due to moving particles can be in general neglected when determining the range of the scatterer, because the frequency shift is much smaller than the frequency interval that separates two range gates.

<sup>12</sup>Note that *continuously* refers to a stepwise increase of the transmitted frequency due to discretized nature of digital data.

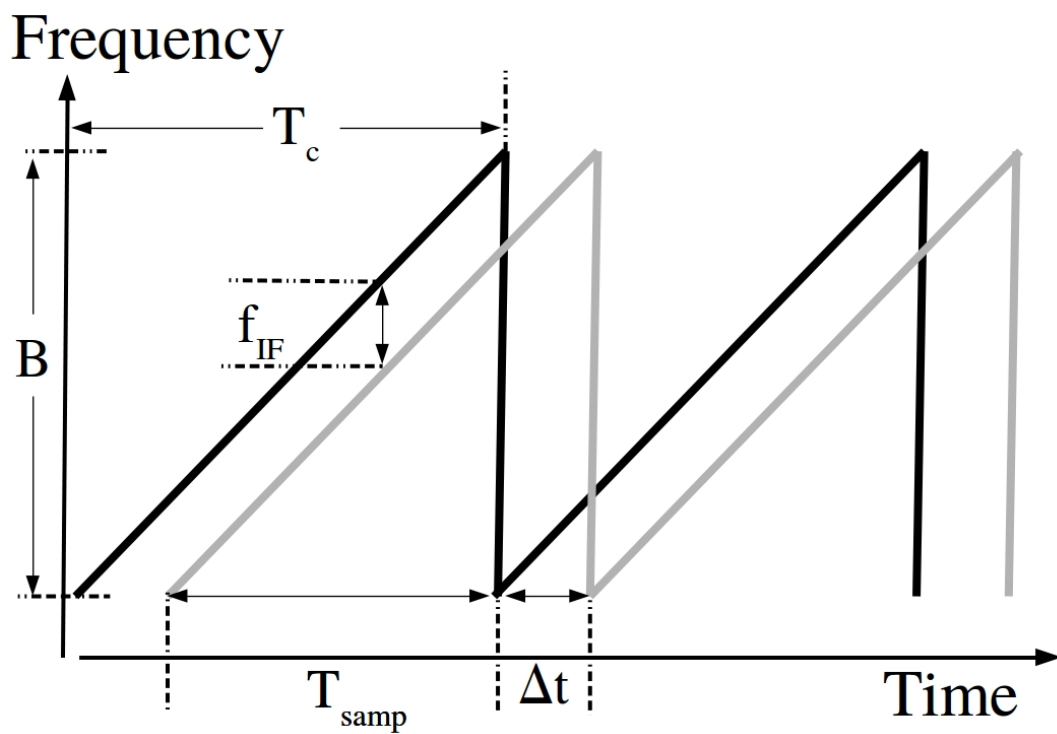


FIGURE 2.3: Example of a sawtooth chirp  $T_c$ . Transmitted frequencies over  $B$  (black line). Received frequencies delayed by  $\Delta t$  (gray line). The backscattering particle's distance and velocity determine  $f_{\text{IF}}$ . The sampling time  $T_{\text{samp}}$  is determined by the maximum distance that is sampled.



of  $f_{IF}$  signals. To unfold this superposition, a *Fast Fourier Transformation* (FFT; Cooley and Tukey, 1965) is performed over one chirp providing the original  $f_{IFs}$  that can be directly mapped into the range space via Eq. (2.5).

The smallest change of  $f_{IF}$  ( $\delta f_{IF}$ ) that can be resolved depends on the sampling frequency  $f_0$  of the data processing unit and the number of sampled data points ( $N_{fft}$ ):

$$\delta f_{IF} = \frac{f_0}{N_{fft}} \quad (2.7)$$

Due to the *Nyquist limit* (Shannon, 1949), the FFT frequency spectrum can resolve  $N_{fft}/2$  *intermediate frequencies* (IFs). The total sampling time

$$T_{samp} = N_{fft} T_{bin} \quad (2.8)$$

is determined by  $N_{fft}$  and the sample time  $T_{bin}$  of each discrete frequency step of the chirp.

Thus, Eq. (2.7) can be rewritten to

$$\delta f_{IF} = \frac{f_0 T_{bin}}{T_{samp}} = \frac{1}{T_{samp}} \quad (2.9)$$

showing that the frequency resolution depends only on the total sampling time.

To determine the range resolution  $\delta R$ , the discretized derivative from Eq. (2.5) is taken yielding

$$\frac{\delta f_{IF}}{\delta R} = \frac{2B^*}{c T_{samp}}. \quad (2.10)$$

Combining Eq. (2.9) and Eq. (2.10) gives the range resolution:

$$\delta R = \frac{c}{2B^*} \quad (2.11)$$

After decomposing the IF signals into the corresponding range gates, the decomposed IF signals can be further analyzed by applying a second FFT in each range gate that separates the contributions from targets moving with different velocities yielding the *Doppler spectrum*. A moving target with velocity  $v_d$  [m s<sup>-1</sup>] shifts the phase of  $s_r$  over time producing a frequency shift  $f_d$  [Hz] of the IF signal according to the Doppler effect:

$$f_d = f_t \frac{2v_d}{c} \quad (2.12)$$

where  $f_t$  is the transmitted frequency. The phase change of  $s_r$  over time is

sampled by executing  $M_{fft}$  chirps sequentially providing a time series of IF signals in each range gate. Thus, the Doppler frequency resolution<sup>13</sup> is given by

$$\delta f_d = \frac{f_{samp}}{M_{fft}}, \quad (2.13)$$

which can be mapped into the velocity space. The sampling frequency of the chirps  $f_{samp}$  is inversely proportional to the chirp duration:

$$f_{samp} = \frac{1}{T_c} \quad (2.14)$$

The maximum unambiguous velocity ( $v_N$ ; henceforth *Nyquist velocity*) is determined by the Nyquist limit, i.e. the maximum resolvable  $f_d$ :

$$f_d^{max} = \frac{f_{samp}}{2} = \frac{1}{2T_c} \quad (2.15)$$

#### 2.2.4 Radar Moments

Due to a finite vertical resolution and a finite beam width, radar back-scatter signals are created by multiple scatterers. When assuming randomly distributed particles and no shadowing effects between them<sup>14</sup>, the back-scattering cross-section per unit volume (henceforth *radar reflectivity*  $\eta$  [ $\text{m}^{-1}$ ]) can be expressed as (Doviak and Zrnić, 1993, p. 82)

$$\eta = \int_0^\infty n(D)\sigma_B(D)dD \quad (2.16)$$

with the particle size distribution  $n(D)$  [ $\text{m}^{-4}$ ]. Assuming Rayleigh-scattering,  $\eta$  can be re-written using Eq. (2.1) to

$$\eta = \frac{|K_w|^2 \pi^5}{\lambda^4} Z \quad (2.17)$$

with the *radar reflectivity factor* [ $\text{m}^6 \text{m}^{-3}$ ]

$$Z = \int_0^\infty n(D)D^6 dD. \quad (2.18)$$

<sup>13</sup>Note that despite the 1<sup>st</sup> FFT, the FFT spectrum of the 2<sup>nd</sup> FFT consists of  $M_{fft}$  independent points because the input time series are complex, instead of real, numbers.

<sup>14</sup>Then, incoherent scattering theory is applicable, i.e. the total scattering cross-section equals the sum of individual particles' cross-sections.

If the Rayleigh-approximation does not apply,  $Z$  is called the *equivalent radar reflectivity factor*  $Z_e$ , which will be henceforth used to assure generality.

From the Doppler spectrum in velocity space (Fig. 2.4), spectral moments can be determined after the noise floor has been removed. Here, the method from Hildebrand and Sekhon (1974) is used. The  $k^{\text{th}}$  statistical moment  $M^k$  about the value  $q$  of the Doppler spectrum is given by

$$M^k = \int_{-\infty}^{\infty} (v_d - q)^k Z_e(v_d) dv_d \quad (2.19)$$

with the spectral reflectivity factor  $Z_e(v_d)$  and the Doppler velocity  $v_d$ . Hence, the  $0^{\text{th}}$  moment of  $M^k$  about  $q = 0$  is the reflectivity factor  $Z_e$ .

The first moment of the discrete Doppler spectrum, normalized with  $Z_e$ , is the mean Doppler velocity [m s<sup>-1</sup>] and is given by

$$v_m = \frac{\sum_i^{M_{fft}} Z_e(v_d(i)) v_d(i)}{Z_e}, \quad (2.20)$$

where  $M_{fft}$  is the number of spectral bins<sup>15</sup>. The mean Doppler velocity is determined by the nominal fall velocities of each particle and the vertical air motion (Gunn and Kinzer, 1949). It has been used for many different application, such as to obtain PSD (Gunn and Kinzer, 1949), vertical air motion (Kollias, Albrecht, and Marks, 2002) or to constrain LWC retrievals (Khain et al., 2008). In Publication I,  $v_m$  is used to investigate the performance of the new FMCW radar.

Beside  $Z_e$  and  $v_m$ , higher central moments about the mean of the distribution are typically used in radar-meteorology (Doviak and Zrnić, 1993, p. 109). The square root of the second central moment is the spectral width [m s<sup>-1</sup>]

$$\sigma_v = \sqrt{\frac{\sum_i^{M_{fft}} Z_e(v_d(i)) (v_d(i) - v_m)^2}{Z_e}} \quad (2.21)$$

depending on  $v_m$  and is influenced by turbulence and wind shear (Doviak, Zrnić, and Sirmans, 1979), which can therefore be retrieved analyzing Doppler spectra (e.g. Atlas, 1964).

The Doppler spectrum skewness, being the third central moment,

$$Sk = \frac{\sum_i^{M_{fft}} Z_e(v_d(i)) (v_d(i) - v_m)^3}{Z_e \sigma_v^3} \quad (2.22)$$

<sup>15</sup> $M_{fft}$  refers to the number of samples of the  $2^{nd}$  in the data processing (see section 2.2.3).

is a measure of how much the spectrum is tilted with respect to a symmetric distribution. The skewness is smaller (greater) than zero, if the spectrum is tilted to towards larger (smaller) values. The skewness can be used for example to identify liquid layers in ice clouds (Yu et al., 2014) or to determine the onset of drizzle (Luke and Kollias, 2013; Acquistapace et al., 2017). The latter approach is used in Publication III in a modified way to improve the retrieval of LWC in drizzling liquid water clouds.

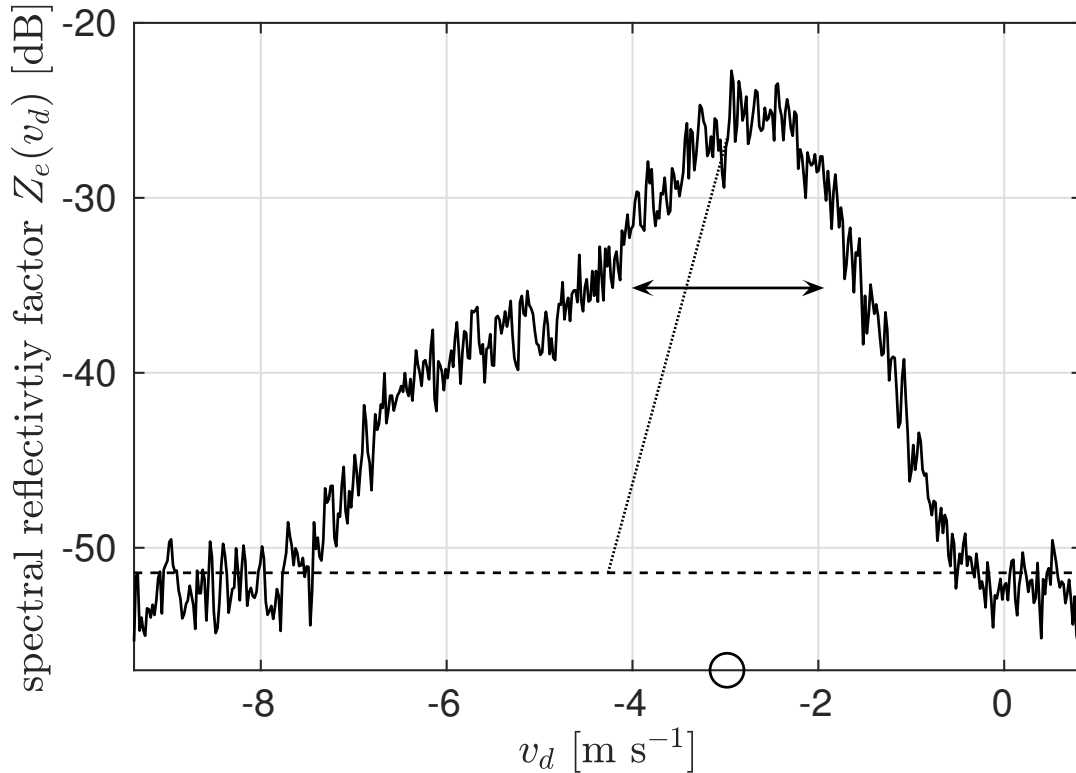


FIGURE 2.4: Radar Doppler spectrum (solid line), measured by a 94 GHz radar (Publication I), showing the spectral reflectivity  $Z_e(v_d)$  depending on the Doppler velocity  $v_d$ . The dashed horizontal line indicates the mean noise floor that is subtracted from the signal before spectral moments are calculated. The circle indicates the mean Doppler velocity, the double-arrow the spectral width, and the dotted and tilted line the negative skewness. Note that Doppler velocities smaller than zero correspond to particles moving towards the radar. This notation is used in Publication I. However, some data sets are based on a converse notation, such as the data set used in Publication III.

### 2.2.5 Determining the Liquid Water Path

State-of-the-art LWP retrievals combine several (minimum 2) frequencies, usually at 22.235 and around 30 GHz (Crewell et al., 2001). LWP [kg m<sup>-2</sup>] is

linearly related to the differential change of BT at these frequencies (Löhnert and Crewell, 2003). As the first frequency is located at the water vapor absorption line, the IWV can be obtained simultaneously. In section 4.1, it will be shown that LWP can also be retrieved by using only one BT at a window frequency when knowing the IWV from an external source. The accuracy of LWP retrievals is about 15-30 g m<sup>-2</sup> depending both on the instrument's sensitivity and absolute calibration accuracy (Löhnert and Crewell, 2003; Turner et al., 2007).

### 2.2.6 Retrieving Liquid Water Content

The liquid water content of warm low-level stratified clouds can be derived with various ground-based techniques (e.g. Atlas, 1954; Fox and Illingworth, 1997; Frisch, Fairall, and Snider, 1995; Frisch et al., 1998; Rusli, Donovan, and Russchenberg, 2017). A commonly used approach is to combine LWP from MWR and  $Z_e$  measurements from radar like in Frisch et al. (1998) (henceforth *standFrisch* for "standard Frisch"). The *standFrisch* scales the LWP with the reflectivity signal to obtain LWC [kg m<sup>-3</sup>] estimates:

$$LWC_i = \frac{LWP \sqrt{Z_e(i)}}{\sum_{j=1}^{N_i} \delta R_j \sqrt{Z_e(j)}} \quad (2.23)$$

where  $\delta R_i$  [m] is the vertical resolution at layer  $i$  and  $N_i$  is the total number of layers. The retrieval assumes that the number concentration of droplets is constant with height and that Rayleigh-scattering applies, i.e. the 3<sup>rd</sup> moment of the PSD is linearly related to the 6<sup>th</sup> moment. These assumptions have been found to be frequently valid for Sc (Frisch et al., 1998); however, an uncertainty remains. In particular, once drizzle is present in the cloud *StandFrisch* is strongly biased or even produces unrealistic results (see [Publication III](#)). Note that any relative uncertainty in LWP translates into the same relative uncertainty in the entire LWC profile. The *standFrisch* is used in [Publication II](#) and [Publication III](#).

## 2.3 Modeling Warm Low-Level Stratified Clouds

Modeling cloud processes is necessary to increase the understanding of cloud micro-physical processes and to provide references for cloud observations. Further, they can help to develop and improve retrieval algorithms as is

shown in [Publication III](#). Cloud micro-physical processes can be either parameterized or modeled by solving the governing thermodynamical- and fluid-dynamical equations.

Everything that the spatio-temporal resolution of a model cannot resolve, has to be parameterized. Hence, the scales vary tremendously, on which parameterizations are implemented: in climate and coarse weather prediction models, macro-physical properties of clouds, such as LWP, must be parameterized (Bogenschutz and Krueger, 2013). Large eddy simulations (LES) parameterize cloud micro-physics, such as autoconversion, in bulk micro-physical schemes (Kessler, 1969) or explicit micro-physical schemes (Feingold et al., 1994). Direct numerical simulations can resolve turbulence to Kolmogorov scale, but still require parameterizations of some micro-physics, such as droplet activation or condensation (e.g. Kumar et al., 2017).

If the cloud micro-physics are given, radiative transfer models (RTM; Clough et al., 2005) can be applied to estimate extinction properties of hydrometeors (Ebell et al., 2011). RTMs can also be used to forward model radar and MWR observables, such as Doppler spectrum moments and BTs, to investigate how changes in micro-physics affect MWR and radar observations and to test retrievals.

In [Publication II](#) and [Publication III](#) two different types of models are used: the *1-D steady state bin-micro-physical model* (MiMo) by Kollias et al. (2011) is used to simulate drizzle evolution in warm clouds and the *Passive and Active Microwave Radiative Transfer Model* (PAMTRA; Maahn et al., 2015) to simulated radar and MWR observables. Information on model setup and uncertainties are provided in the corresponding sections as well as in the cited literature.

## Chapter 3

# Energy Transitions and Climate Change

### 3.1 Study I: Uncertainty Estimates of Energy System Investment Models

In context of the project *Energy Transitions and Climate Change*, an interdisciplinary study is conducted to investigate how energy systems must be modified to account for a changing climate and the associated shifts in "climate-friendly" energy policy. The study by Henckes et al. (2018b, in preparation) investigates the uncertainty of the Renewable Power System Model (RPSM), being an energy investment model (ESIM), that assumes a reduction of CO<sub>2</sub>-emissions of 90 % compared to 1990 by 2050 in Germany (henceforth 90%-scenario). ESIMs are used to investigate how future stable energy systems look like by optimizing costs, demand and available energy resources, such as nuclear energy, coal, gas and renewables. Henckes et al. (2018b) estimate the uncertainty of RPSM based on uncertainties of meteorological input data that is needed to predict available wind and solar energy. They average the 20 years high-resolution (6 km horizontal grid) reanalysis COSMO-REA6 over Germany (Bollmeyer et al., 2015) to a one-year reference time series of wind and solar radiation and quantify the time series' uncertainties by comparing COMSO-REA6 data to observations. To reduce computational costs, Henckes et al. (2018b) reduce the time series to about a dozen *representative days* by a multi-dimensional clustering (e.g. Nahmmacher et al., 2016). Thus, the representative days should represent most of the variability of possible scenarios of energy demand and production to ensure a stable energy supply under various meteorological conditions. The meteorological input data is converted into available renewable energy using the Renewable Energy Output Model (Henckes et al., 2018a). Figure 3.1a shows how the share of

different technologies of the total energy generation evolves under the 90%-scenario based on the determined representative days. The total generation, i.e. the sum of demand and losses by power plants, is assumed to stay constant. It is evident that the share of renewables, in particular wind, increases until 2050. The decrease of the renewables' share after 2050 is currently under investigation and cannot be answered yet. Comparing the increase of wind energy to the increase of photovoltaic (PV) energy shows that wind energy production in Germany is much more efficient than PV, hence, more investments are made in the wind energy sector. Nevertheless, PV contributes to about 7 % to the total generation by 2050.

To obtain the uncertainty of RPSM, Henckes et al. (2018b) run RPSM additionally using representative days with perturbations according to the uncertainties found for wind and solar radiation. First results indicate (Fig. 3.1b) that the predicted energy system shows significant differences between the perturbed run and unperturbed one. Figure 3.1b illustrates what happens if available wind and solar energy is underestimated: investments into wind energy, in terms of share of energy generation, are reduced by almost 20 % by 2050 and must be replaced by other technologies. Besides investments into biomass, the underestimation of wind and solar energy is compensated by investments into gas energy. This implies that Germany, being the world's biggest importer of gas (BGR, 2017), would need to increase its imports enhancing the dependency on gas-exporting countries. The preliminary findings by Henckes et al. (2018b) show that it is key to further investigate the uncertainties of ESIMs in order to ensure reasonable decisions on energy policy and investments into renewables. Note that the authors consider only errors in the meteorological input data and do not consider any biases due to model assumptions, demand variations or political decisions such as the exit from nuclear energy production by Germany.

To estimate the available solar energy that is used as input by Henckes et al. (2018b), the tilt angle of photovoltaic (PV) systems must be known. In the following, it is shown how the optimal tilt angle over Germany can be determined based on two radiation models: The analytical model by Klucher (1979) (KM) estimates the total solar flux on a PV panel by considering direct and diffuse radiation separately. In particular, it uses a geometrical approach to determine how much diffuse radiation is shaded and additionally received by surface reflections due to the tilting of the PV panel. The model by Perez et al. (1990) (PM) estimates radiation components mainly based on the tilt angle and on a look-up table depending on an empirically estimated clearness



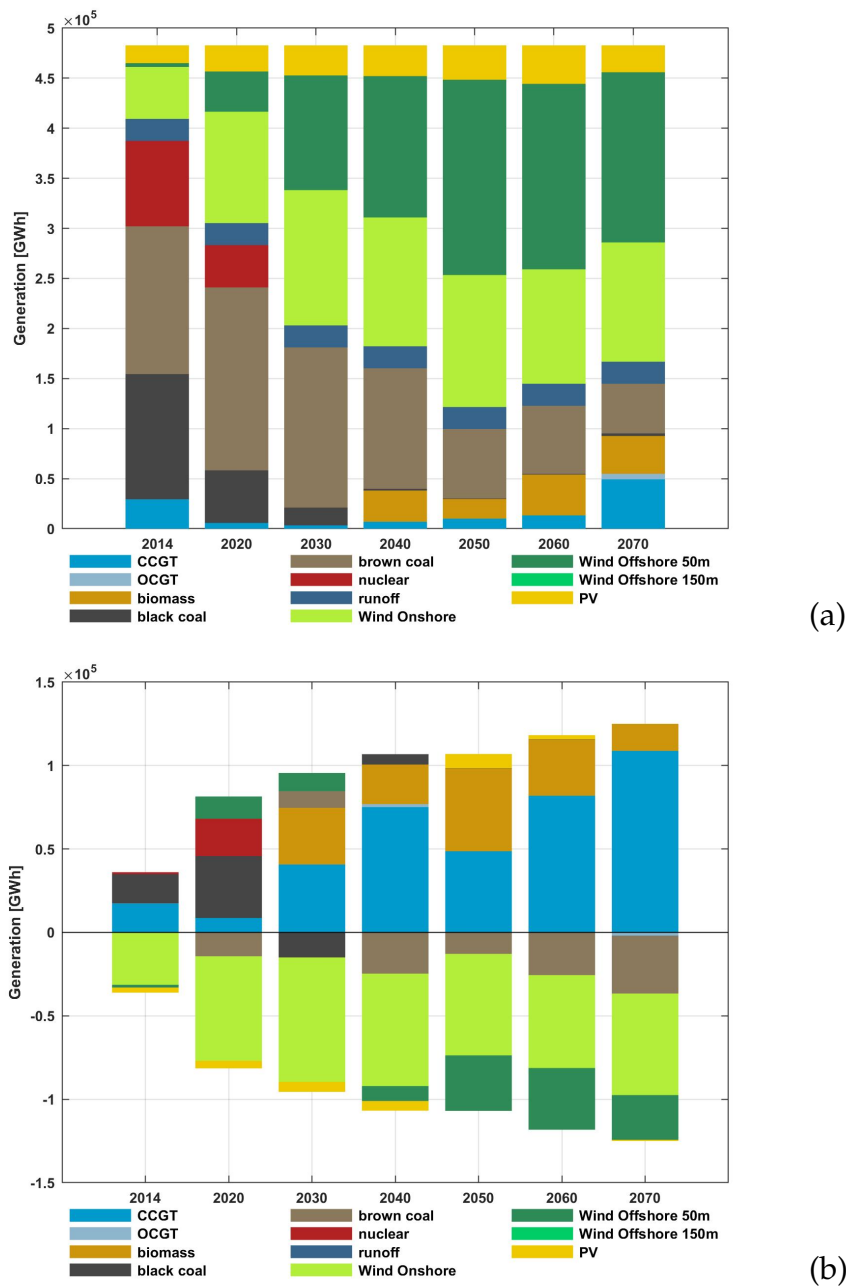


FIGURE 3.1: (a) Estimated contributions to the total energy generation in Germany of by different technologies for the 90%-scenario. CCGT, OCGT and PV are abbreviations for combined cycle gas turbine, open cycle gas turbine and photovoltaic, respectively. Runoff represents water power. The results are obtained from the Renewable Power System Model (RPSM) by Henckes et al. (2018b) that is coupled with the Renewable Energy Output Model (Henckes et al., 2018a) whose meteorological input data is based on 20 years averaged reanalysis data. (b) Difference between RPSM output based on meteorological input data from (a) perturbed by its uncertainty and the results shown in (a). The perturbed case represents an underestimation of available wind and solar energy. Source Henckes et al. (2018b).

index.

## 3.2 Optimal Tilt Angles of Photovoltaic Systems in Germany

Based on the radiation data of COSMO-REA6, the optimal tilt angle, with respect to maximum producible energy, was determined for south-oriented PV systems at each location implemented in the solar energy model used by Henckes et al. (2018b). First, the COSMO-REA6 radiation data from 1995 to 2015 was averaged to a one year time series for every location. Then, the total solar flux on a tilted plane was calculated for various tilt angles. In the final step, the tilt angle providing the largest cumulative flux was selected. The total flux  $S_{tot}$  [ $\text{W m}^{-2}$ ] is determined by

$$S_{tot} = S_{dir} + S_{dif} + S_{ref} \quad (3.1)$$

whereas  $S_{dir}$  is the direct incident radiation depending on the sun's zenith and azimuth angle, and the tilt angle  $\theta_{tilt}$  of the plane. For comparison, the diffuse contribution  $S_{dif}$  was determined using KM and PM.  $S_{ref}$  is the radiation that reaches the panel after being reflected by the surface and depends on  $\theta_{tilt}$  and the surface albedo  $A$ .

Figure 3.2 shows the optimal tilt angle for entire Germany for both models and their differences. In both models the tilt angles are about  $10^\circ$  smaller than the latitude, which is due to the contribution of diffuse radiation.  $S_{dif}$  contributes on average between 25 to 75% to the total radiation in Germany, depending on the location. The models differ on average by  $4^\circ$ . How these differences translate into uncertainties in available energy will be discussed in the next section.

Significant patterns, such as the stripe of low tilt angles at about  $48.5^\circ$  North  $9-12^\circ$  East in the KM, correspond to patterns found in the averaged direct radiation on an horizontal plane. Hence, the horizontal stripe corresponds to an area of low direct solar radiation.

## 3.3 Sensitivity of Radiation Models

The amount of modeled energy that can be produced by a PV panel is constrained by the physical properties of the panel and the environmental input

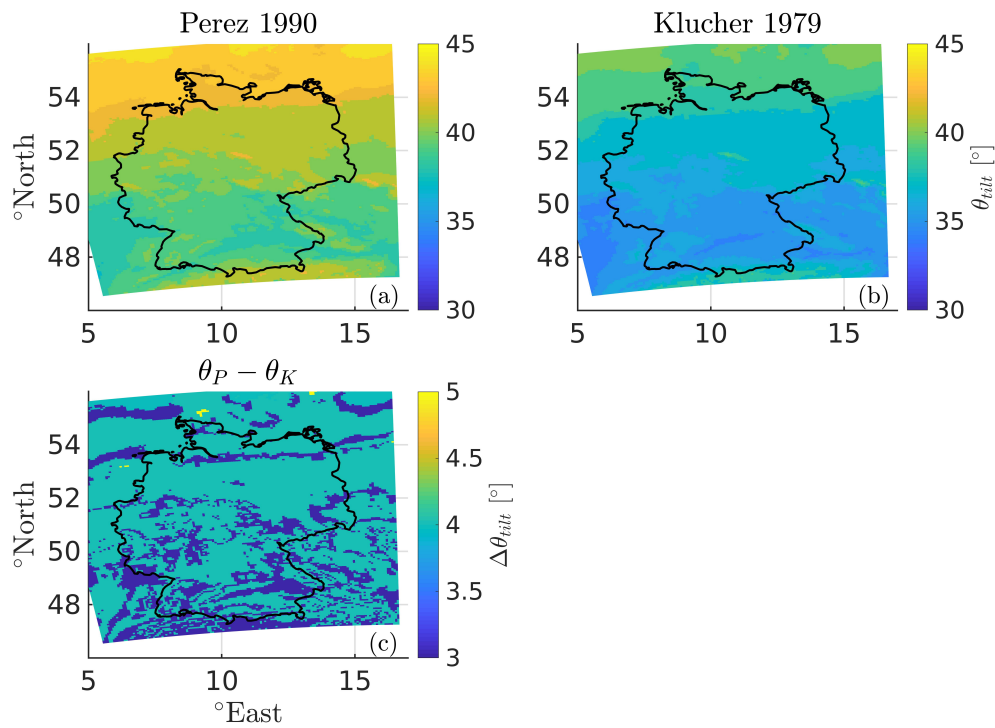


FIGURE 3.2: Optimal tilt angle for southerly oriented PV panels in Germany determined using COSMO-REA6 radiation and surface albedo data with two different radiation models: (a) PM (Perez 1990) and (b) KM (Klucher 1979). (c) Difference  $\Delta\theta$  between the two models' output angles  $\theta_P$  and  $\theta_K$  of PM and KM model, respectively.

parameters, being the direct and diffuse radiation, surface albedo, and panel tilt angle. To investigate the sensitivity of the KM and PM with respect to energy produced per year to the environmental parameters, a total efficiency<sup>1</sup> of PV panels of 10 % and an area of 1 m<sup>2</sup> is assumed. The analysis is done for an exemplary location at 50.9213°N and 6.4002°E that was arbitrarily chosen, because large sensitivity differences between any grid points in Germany are not expected due to the large time frame averaged.

Figure 3.3a shows the energy produced per year depending on the tilt angle and model for diffuse radiation. The maximums correspond to the optimal tilt angles illustrated in Fig. 3.2. The sensitivities, derived from these curves, are shown in Fig. 3.3b, i.e. how much does the produced energy change when changing the tilt angle. It is evident that the sensitivity is very low, being on the order of 0.1 kWh y<sup>-1</sup> deg<sup>-1</sup>, close to the maximums. Moreover, the difference of the maximum energies in Fig. 3.3a between KM and PM is smaller than 1%.

In the next step, all model input parameters are disturbed by their uncertainties given by Henckes et al. (2018b) (see table 3.1), while all other parameters are kept constant and using the optimal tilt angles from section 3.2. Then, the energy difference  $\Delta E$  to the undisturbed case is calculated. It is found that the direct radiation, exhibiting 23 (24)% relative uncertainty for the KM (PM), is the largest uncertainty source and the absolute error is one order of magnitude larger than the error of all other input parameters. An overview is given in table 3.1.

The results of the sensitivity study suggest that the choice of the radiation model does not significantly change the amount of producible energy compared to the uncertainty of  $S_{dir}$ . Therefore, the KM is used by Henckes et al. (2018b), because it is an analytical model and is not based on empirical findings like the PM. The second conclusion is that the direct solar radiation represents the major uncertainty source exhibiting an uncertainty of one order of magnitude larger than all other model input parameters. Therefore the uncertainties of the latter are neglected and only the  $S_{dir}$  is used by Henckes et al. (2018b) to estimate the error in available solar energy.

---

<sup>1</sup>that depends also on environmental parameters such as air temperature

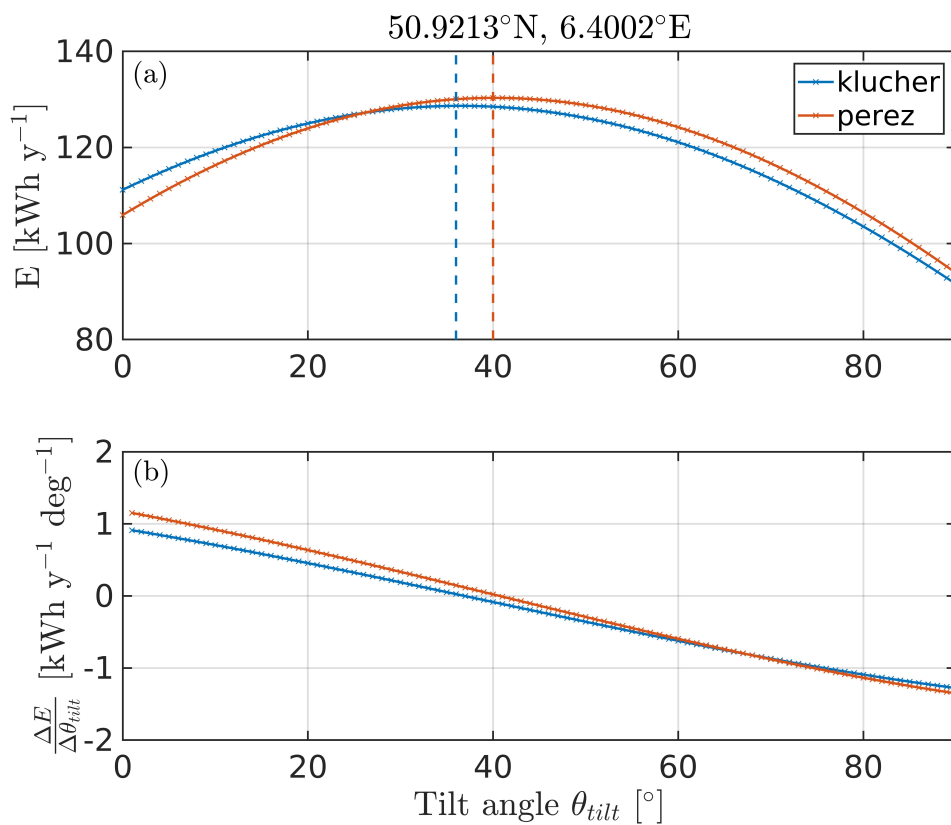


FIGURE 3.3: (a) Produced energy, depending on the tilt angle and the radiation model (KM and PM), by a PV system of  $1 \text{ m s}^{-2}$  area with an efficiency of 10 %. (b) Sensitivity of energy production in  $\text{kWh y}^{-1} \text{ deg}^{-1}$  depending on the tilt angle.

TABLE 3.1: Sensitivity of radiation models KM and PM with respect to the uncertainties of the input parameters, being the direct radiation  $S_{dir}$ , the diffuse radiation  $S_{dif}$  and the surface albedo  $A$ . Each input parameter was disturbed by its uncertainty determined by Henckes et al. (2018b) (first column), while all others were kept constant. Given are absolute and relative energy differences [ $\text{kWh y}^{-1}$ ] to a reference PV panel having an area of  $1 \text{ m}^2$ , an efficiency of 10 % and a tilt angle of  $36^\circ$  and  $40^\circ$  for the KM and PM, respectively. The reference energies  $E_{opt}$ , determined using the optimal tilt angles, are 129 and  $130 \text{ kWh y}^{-1}$  for the KM and PM, respectively. Note potential energy loss induced by an uncertainty of the surface albedo is smaller than  $0.5 \text{ kWh y}^{-1}$ .

|           | Uncertainties after<br>Henckes et al. (2018b)  | KM                      |                            | PM                      |                            |
|-----------|--|-------------------------|----------------------------|-------------------------|----------------------------|
|           |  | $\Delta E$              | $\frac{\Delta E}{E_{opt}}$ | $\Delta E$              | $\frac{\Delta E}{E_{opt}}$ |
| $S_{dir}$ | $123 \text{ W m}^{-2}$                         | $30 \text{ kWh y}^{-1}$ | 23 %                       | $31 \text{ kWh y}^{-1}$ | 24 %                       |
| $S_{dif}$ | $(0.26 \cdot S_{dif} + 20.5) \text{ W m}^{-2}$ | $3 \text{ kWh y}^{-1}$  | 2 %                        | $3 \text{ kWh y}^{-1}$  | 2 %                        |
| $A$       | 0.03   | $0 \text{ kWh y}^{-1}$  | 0 %                        | $0 \text{ kWh y}^{-1}$  | 0 %                        |

## Chapter 4

# New Opportunities for Ground-Based Remote Sensing of Clouds

### 4.1 Publication I

N. Kuchler et al. (2017). "A W-Band Radar–Radiometer System for Accurate and Continuous Monitoring of Clouds and Precipitation". In: *Journal of Atmospheric and Oceanic Technology* 34.11, pp. 2375–2392. ISSN: 0739-0572. DOI: [10.1175/JTECH-D-17-0019.1](https://doi.org/10.1175/JTECH-D-17-0019.1). URL: <http://journals.ametsoc.org/doi/10.1175/JTECH-D-17-0019.1> ©American Meteorological Society. Used with permission.

## A W-Band Radar–Radiometer System for Accurate and Continuous Monitoring of Clouds and Precipitation

NILS KÜCHLER, STEFAN KNEIFEL, AND ULRICH LÖHNERT

*Institute for Geophysics and Meteorology, University of Cologne, Cologne, Germany*

PAVLOS KOLLIAS

*School of Marine and Atmospheric Sciences, Stony Brook University, State University of New York, Stony Brook, New York*

HARALD CZEKALA AND THOMAS ROSE

*Radiometer Physics, Meckenheim, Germany*

(Manuscript received 23 January 2017, in final form 26 July 2017)

### ABSTRACT

A new 94-GHz frequency-modulated continuous wave (FMCW) Doppler radar–radiometer system [Jülich Observatory for Cloud Evolution (JOYCE) Radar–94 GHz (JOYRAD-94)] is presented that is suitable for long-term continuous observations of cloud and precipitation processes. New features of the system include an optimally beam-matched radar–radiometer; a vertical resolution of up to 5 m with sensitivities down to  $-62$  dBZ at 100-m distance; adjustable measurement configurations within the vertical column to account for different observational requirements; an automatic regulation of the transmitter power to avoid receiver saturation; and a high-powered blowing system that prevents hydrometeors from adhering to the radome. JOYRAD-94 has been calibrated with an uncertainty of 0.5 dB that was assessed by observing a metal sphere in the radar’s far field and by comparing radar reflectivities to a collocated 35-GHz radar. The calibrations of the radar receiver and the radiometric receiver are performed via a two-point calibration with liquid nitrogen. The passive channel at 89 GHz is particularly useful for deriving an estimate of the liquid water path (LWP). The developed retrieval shows that the LWP can be retrieved with an RMS uncertainty (not including potential calibration offsets) of about  $\pm 15$  g m $^{-2}$  when constraining the integrated water vapor from an external source with an uncertainty of  $\pm 2$  kg m $^{-2}$ . Finally, a dealiasing method [dual-radar dealiasing method (DRDM)] for FMCW Doppler spectra is introduced that combines measurements of two collocated radars with different measurement setups. The DRDM ensures high range resolution with a wide unambiguous Doppler velocity range.


### 1. Introduction

Clouds play a major role in Earth’s hydrological cycle and radiation budget (Boucher et al. 2013); thus, it is important to characterize them with high accuracy and spatial resolution. Reliable and robust ground-based Doppler radars and radiometers are key instruments for detailed observations of cloud processes, long-term data collection, and model and satellite evaluations. Here, we

present a system [Jülich Observatory for Cloud Evolution (JOYCE) Radar-94 GHz (JOYRAD-94)] that combines frequency-modulated continuous wave (FMCW) Doppler radar with passive radiometer observations at millimeter wavelengths (94 and 89 GHz, respectively), providing new opportunities for cloud observations.

Radars operating at millimeter-wavelength can be used—among other applications—to determine cloud microphysical processes (e.g., Kollias et al. 2007a; Luke and Kollias 2013; Kneifel et al. 2011; Acquistapace et al. 2017; Tridon and Battaglia 2015) to estimate rain rates (Maahn et al. 2015), or to obtain information about in-cloud turbulence (e.g., Kollias et al. 2002; Borque et al. 2016).

Moreover, radars are combined with other remote sensors in order to enhance the sensitivity and the

 Denotes content that is immediately available upon publication as open access.

Corresponding author: Nils Küchler, nkuech@meteo.uni-koeln.de



accuracy of the derived cloud properties. For example, Frisch et al. (1998) used microwave radiometer (MWR) and radar data to retrieve the liquid water content (LWC) profile of a cloud. The vertically integrated amount of liquid water [also liquid water path (LWP)] was constrained by the MWR, and the range-resolved radar signal was used to reconstruct the liquid water vertical distribution. Illingworth et al. (2007) exploited the synergy of collocated radar, microwave radiometer, and lidar observations to obtain further refined cloud properties, such as the hydrometeor phase, type, and position in the vertical column (Cloudnet algorithm).

Currently, the majority of cloud radars—especially at comprehensive observatories (e.g., Löhnert et al. 2015; Kollias et al. 2007b; Haeffelin et al. 2005)—are pulsed systems. Illingworth et al. (2015) pointed out that FMCW radars can be a more economical solution, which then could further increase the number of observatories for comprehensive cloud studies that are needed for climate monitoring. However, FMCW radar requires two antennas, which could in turn increase system costs, especially when considering low-frequency radars where larger antenna diameters are required (Heijnen et al. 2000).

A further disadvantage of FMCW technology is that it requires a large bandwidth at great distance to sustain vertical and temporal resolution, which increases the background noise. Nevertheless, several publications showed that FMCW W-band radars are suitable for both ground-based (Yamaguchi et al. 2009; Huggard et al. 2008; Bennett et al. 2009; Thies et al. 2010; Delanoë et al. 2016) and airborne fog and cloud studies (Pazmany et al. 1994; Mead et al. 2003).

FMCW radars often allow greater flexibility of varying vertical resolution. For JOYRAD-94 a vertical resolution of 5 m can be used (note that in principal, even finer vertical resolutions are possible), which is beneficial for evaluating high-resolution model simulations such as large-eddy simulations (LES) (e.g., van der Dussen et al. 2013) or for investigating processes with strong vertical gradients (e.g., melting layer).

The increased time on target, because of continuous transmission, provides similar average output powers as pulsed systems and leads to comparable sensitivities. In general, FMCW systems are cheaper to build because of their simpler electronic design and lack of high-voltage components (Lighthart and Nieuwkerk 1980), which further leads to better long-term stability and easier calibration. Also, their smaller instrument dimensions and lower transmitter power facilitate their installation in various environments.

High-frequency radars operating in the W-band provide greater sensitivity to small hydrometeors, which

allow, for example, for investigating thin liquid or ice clouds and their microphysical processes (Lhermitte 1987). The disadvantage of using high frequencies is increasing signal attenuation as a result of dry gases, water vapor, and frozen and liquid hydrometeors.

Figure 1 shows the W-band radar radiometer at JOYCE (Löhnert et al. 2015) in Jülich, Germany, and at the Alfred Wegener Institute for Polar and Marine Research and the French Polar Institute Paul Emile Victor (AWIPEV) Arctic Research Base in Ny-Ålesund, Norway. At JOYCE ([www.joyce.cloud](http://www.joyce.cloud)) it is located next to a pulsed 35-GHz system (JOYRAD-35) for high-accuracy dual-frequency retrievals of liquid water content. The Arctic deployment (2016/2017) took place within the German research initiative Arctic Amplification: Climate Relevant Atmospheric and Surface Processes and Feedback Mechanisms [(AC)<sup>3</sup>] (<http://www.ac3-tr.de/>), where the objective is to detect, quantify, and model the feedback mechanism leading to the observed accelerated warming in the Arctic compared to global mean.

JOYRAD-94 is a very compact system with a horizontal extent of  $1.0 \times 1.1 \text{ m}^2$ , a height of 1.3 m, and is installed and recoverable with two persons. It operates under all weather conditions as a result of two high-powered blowing systems that nominally keep the radomes free of liquid and ice. A dry radome is important because a thin liquid layer can contaminate the radar and radiometer measurements significantly; for example, Hogan et al. (2003) observed a two-way radome attenuation of 15 dB. Also, a thin liquid layer on the receiver radome can affect the radiometer brightness temperature measurements by several kelvins, biasing the retrieval of LWP.

As will be explained in detail later in the manuscript, the vertical resolution of JOYRAD-94 is adjustable within up to 10 different layers, making it possible to adapt the resolution and sensitivity to different measurement objectives at different heights. JOYRAD-94 receives the passive and active signals over the same antenna—that is, both sensors observe the same scene and have the same beamwidth of  $0.53^\circ$ —which reduces the uncertainty of retrievals when combining radar and radiometer measurements (Frisch et al. 1998). Such a synergetic instrument was design by Skou (1995) for airborne observations; however, it has not yet been used for ground-based studies.

Common radiometers have beamwidths between  $3^\circ$  and  $6^\circ$ , and therefore smooth out horizontally varying cloud structures (Huang et al. 2014). The passive channel of JOYRAD-94 provides new opportunities for observing spatial and temporal cloud variability, for example, questioning Taylor's hypothesis of "frozen" turbulence, which was found to be valid for radiometers

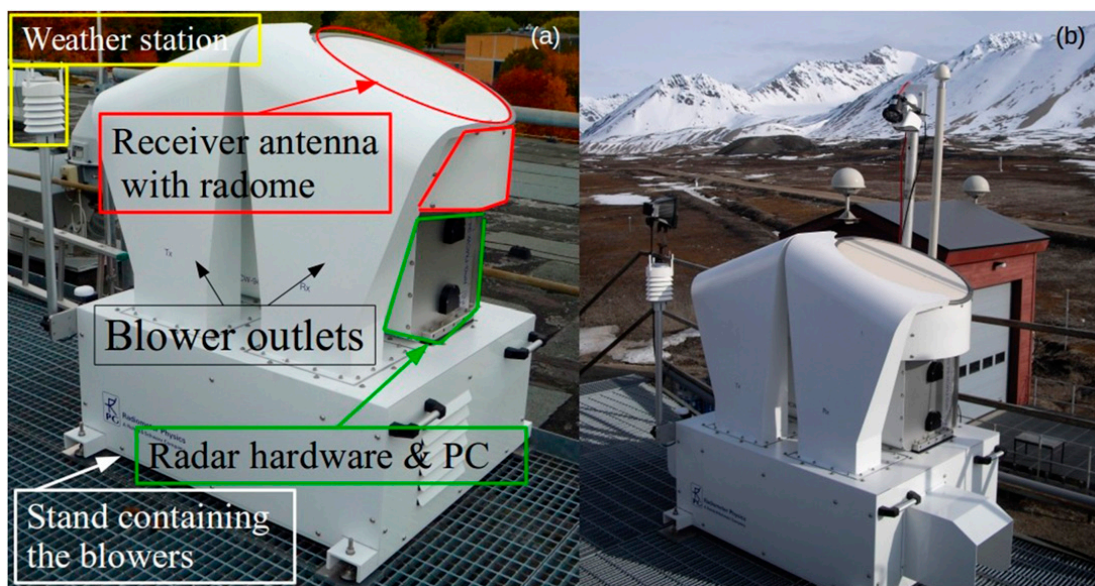


FIG. 1. JOYRAD-94 at (a) JOYCE and (b) AWIPEV station in Ny-Ålesund.

with beamwidths larger than  $1^\circ$  (e.g., [Huang et al. 2008](#)). Moreover, combining matched radar–radiometer measurements with small beamwidths and high vertical resolution can add information on processes at cloud edges, such as turbulence and evaporation induced by lateral entrainment ([Heus and Jonker 2008](#)). However, the latter and LWP variability will not be part of the following discussion; but it is left as a topic for future research.

In the following, we will introduce the instrument’s design, which enables continuous and unattended observations while receiving both the active and passive signals with the same antenna. In [section 3](#), the signal processing is discussed, including the adjustable measurement setup for different atmospheric layers. The performance of the instrument is shown in [section 4](#) followed by a comparison to a 35-GHz pulsed radar. In [section 6](#), we introduce the novelties of JOYRAD-94 for cloud observations. The last section gives a summary and an outlook considering software and hardware updates that will be or have already been included in the system.

## 2. Instrument design

The instrument is designed for long-term unattended observations of cloud macro- and microphysical properties by combining passive and active microwave radiometry at center frequencies of 89 and 94 GHz, respectively. FMCW radar is used to provide high flexibility of range and Doppler resolution variation along the ranging path. Moreover, low transmitter power

(typically 1.5 W) allows for solid-state technology, leading to a long lifetime and low costs.

The main components of the radar–radiometer are the transmitter with adjustable power to protect the receiver from saturation, the Cassegrain two-antenna system, and the receiver containing both the radar receiver channel at 94 GHz and the passive broadband channel at 89 GHz. Both channels are thermally stabilized within a few millikelvin (mK) to ensure accurate output power measurement and radiometric accuracy. A block diagram of the full system and technical specifications are given in [Fig. 2](#) and [Table 1](#), respectively.

### a. Antenna

The Cassegrain antenna, which was recently measured using the solar sun scan technique ([Reimann and Hagen 2016](#)), produces a beam of 95% Gaussian shape. Moreover, the modeled and measured half-power beamwidths (HPWB) are  $0.48^\circ$  and  $0.53^\circ$ , respectively. The modeled and measured antenna gains are 51.8 and 51.5 dB, respectively. JOYRAD-94 was calibrated with the modeled values, which leads to an overestimation of reflectivity of 0.26 dB that has been accounted for in the data analysis. Future versions will use the measured parameters instead. The two antenna systems protect the receiver from saturation, as during continuous transmitter operation it is not possible to separate transmitted and received power. Transmitting and receiving antennas are separated by 568 mm, which leads to a signal loss of 10% at 300 m distance as a result of imperfect beam overlap. Because of the small antenna separation, backscattering theory is still fully

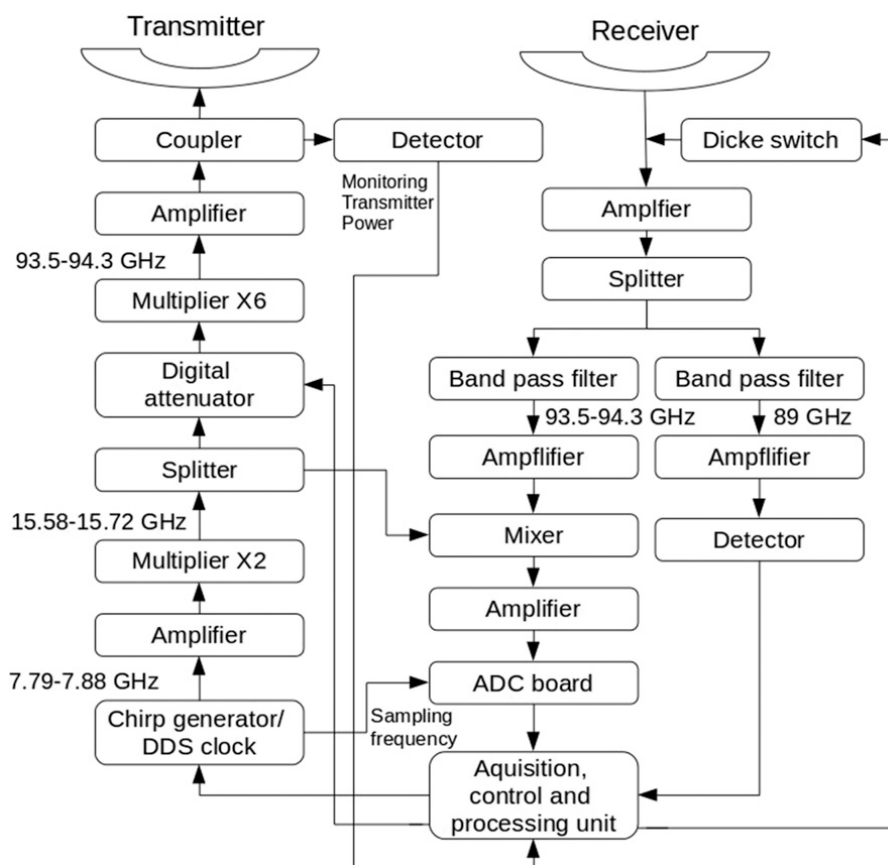


FIG. 2. Block diagram of JOYRAD-94.

applicable. The far field of the antenna begins at about 50 m. The antenna system losses are dominated by subreflector blocking—that is, the subreflector shading the output beam—which was found to cause a power loss of 11%.

### b. Transmitter

The maximum output power is continuously monitored by the radar with a retraceable precision Rhode and Schwarz W-band power head (accuracy of 0.1 dB). The feedhorn insertion loss is  $0.3 \pm 0.05$  dB, which was determined by a Rhode and Schwarz network analyzer (accuracy of 0.05 W). To ensure linear detection while observing a high dynamic range of input power signals (from thin cirrus to precipitating liquid clouds), the radar's transmitter power can be reduced in digital steps by a maximum of 16 dB. Sawtooth chirps are generated by a chirp generator module based on a direct digital synthesizer (DDS) that is clocked by a fundamental oscillator of frequency of 916 MHz. The chirp generator produces an output signal in the range of 7.79–7.88 GHz that is then multiplied by 12 to become the transmitter signal between 94.48 and 94.56 GHz.

### c. Receiver calibration

The radar receiver calibration maps the power at the analog-to-digital converter (ADC) board  $P_n$  (W; for  $n$  range gates) to the power spectrum incident on the radar antenna  $P_m$ —that is, it determines the receiver gain  $G_m$  of the system—so that

$$P_n = G_m P_m. \quad (1)$$

TABLE 1. Radar specifications.

| Frequency             | 94 GHz $\pm$ 100 MHz                |
|-----------------------|-------------------------------------|
| Transmitter power     | 1.5 W (solid-state amplifier)       |
| HPWB                  | 0.53°                               |
| Antenna type          | Two antennas with 500-mm aperture   |
| Antenna separation    | 568 mm                              |
| Antenna gain          | 51.5 dB                             |
| System noise figure   | 3 dB                                |
| A/D sampling rate     | 8.2 MHz                             |
| Profile sampling rate | 0.2–30 s                            |
| Vertical resolution   | 1–100 m                             |
| Doppler range         | $\pm 10 \text{ m s}^{-1}$           |
| Size                  | 1.0 m $\times$ 1.1 m $\times$ 1.3 m |
| Weight                | 80 kg (without stand)               |

Therefore, a so-called hot–cold calibration is performed using a blackbody at environmental temperatures as a “hot” reference and a liquid nitrogen–cooled blackbody as a “cold” reference. The integration time during the calibration is 60 s. Using the radiometer formula (Ulaby and Long 2014, p. 279), a single intermediate frequency (IF) bin of typically 4-kHz bandwidth and about 500-K system noise temperature has a root-mean-square (RMS) noise of 1 K, that is, a peak-to-peak noise of about 4 K.

During the “hot–cold” calibration, the radiometer channel at 89 GHz is calibrated too. The 89-GHz channel has an RMS noise smaller than 0.5 K when integrating on the hot calibration target for any integration times between 5 and 100 s. Küchler et al. (2016) found an uncertainty of  $\pm 0.5$  K for direct detection radiometers of a similar type that were calibrated with liquid nitrogen. Maschwitz et al. (2013) suggested repeating absolute calibrations every 3–6 months to sustain measurement accuracy.

#### d. Calibration cross-check

A calibration cross-check with a metal sphere reflector showed an agreement within 0.5 dB between the expected power ratio of the transmitted and received signals and the measured power ratio. The sphere had a diameter of 48 mm; was lifted by a helium balloon to 104 m above ground at a horizontal distance of approximately 950 m to the radar, resulting in a radial distance of 960 m; and was strapped to the ground by three strings. The distance between the balloon and the metal sphere was about 10 m. The radar was mounted on a positioner that was manually operated using a telescope for precise pointing. To account for the horizontal swinging of the sphere, the integration time was set to 0.2 s and a peak-hold function in the radar software was run, which samples the maximum value observed within 60 s. The procedure was repeated 100 times, resulting in a standard deviation of 0.15 dB of the return signal. Atmospheric attenuation was found to be 0.6 dB over a path of 1920 m, which was determined from radiative transfer calculations assuming homogeneity on the radiation’s path and using surface data from the radar’s meteorological weather station.

#### e. Blowers

A high-powered blower system was installed on JOYRAD-94 for both antennas (Fig. 1, white fixtures) to prevent the adherence of hydrometeors on the radome. The volume flux is  $2000 \text{ m}^3 \text{ h}^{-1}$ , corresponding to approximately  $20 \text{ m s}^{-1}$  wind speed in full-power mode. The blowers are triggered by a Vaisala rain sensor that is part of the meteorological weather

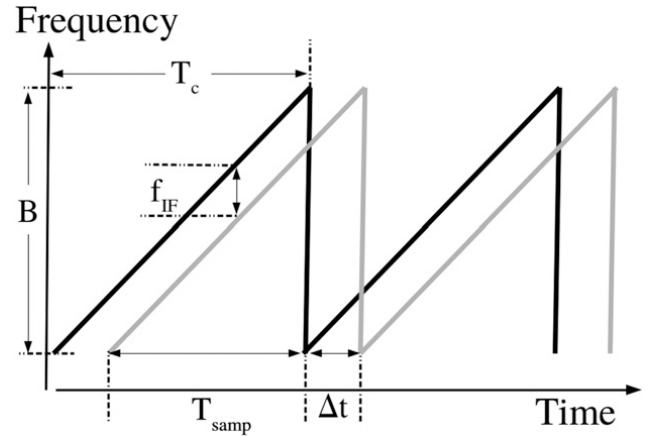


FIG. 3. Example of a sawtooth chirp  $T_c$ . Transmitted frequencies over  $B$  (black line). Received frequencies delayed by  $\Delta t$  (gray line). The backscattering particle’s distance and velocity determine  $f_{\text{IF}}$ . The sampling time  $T_{\text{samp}}$  is determined by the maximum distance that is sampled.

station attached to the radar (Fig. 1, yellow). Moreover, the radome material has a hydrophobic coating and is tilted so that condensate nominally runs off. Therefore, JOYRAD-94 can operate continuously during all weather conditions.

### 3. Signal processing

In this section we briefly describe only the main processing steps and refer the reader to the cited literature (e.g., Strauch 1976; Delanoë et al. 2016; Ulaby and Long 2014, 615–621) for details of FMCW signal processing.

#### a. FMCW principle

Figure 3 illustrates the basic principle of a transmitted sawtooth chirp sequence over the bandwidth  $B$  (Hz), which is backscattered by a single steady particle at distance  $R$  (m). The delay  $\Delta t$  (s) between the transmitted and received signals is determined by the particle’s distance and the propagation speed  $c$  ( $\text{m s}^{-1}$ ) of the transmitted electromagnetic wave:

$$\Delta t = \frac{2R}{c}. \quad (2)$$

Using  $B$  and the chirp duration  $T_c$  (s),  $\Delta t$  is mapped to the measured intermediate frequency  $f_{\text{IF}}$  (Hz; i.e., the difference between the transmitted and received signals) to

$$f_{\text{IF}} = R \frac{2B}{cT_c}. \quad (3)$$

Furthermore, the range resolution  $\delta R$  (m) is determined by  $B$  over

$$\delta R = \frac{c}{2B}. \quad (4)$$

If the particle moves, there will be an additional frequency shift  $f_d$  (Hz; called Doppler shift) between the transmitted and received signals. This shift is much smaller than the IF difference between two range gates (e.g., [Strauch 1976](#)) and is determined by the transmitted frequency  $f_t$  (Hz) and the particle's radial velocities  $v_d$  ( $\text{m s}^{-1}$ ):

$$f_d = \frac{2f_t v_d}{c}. \quad (5)$$

The maximum Doppler shift  $f_{\text{dm}}$  (Hz) is related to  $T_c$  via

$$f_{\text{dm}} = \frac{1}{2T_c}. \quad (6)$$

As several parameters above depend on each other and cannot be chosen arbitrarily because of physical and technical restrictions, certain trade-offs must be considered when defining a measurement setup. This can be illustrated by the so-called Doppler dilemma: the maximum range to be sampled determines the minimum chirp duration; for example, the two-way propagation time of a transmitted signal backscattered at 10 km height is about  $70 \mu\text{s}$ . For a full ranging via a fast Fourier transform (see the next subsection), additional sampling time is required (approximately  $30 \mu\text{s}$ ). Using Eqs. (6) and (5), the maximum unambiguous velocity  $v_N$  (also called Nyquist velocity) is about  $8 \text{ m s}^{-1}$  at 94 GHz. With a given minimum  $T_c$ ,  $B$  is also restricted by Eq. (3) and vice versa, since  $f_{\text{IF}}$  must not exceed certain limits for any  $R$  as a result of technical limitations (see [section 3d](#)). Therefore, increasing  $\delta R$  requires an increase of  $B$  [see Eq. (4)], which requires an increase of  $T_c$ , leading to a decrease of  $v_N$ .

### b. Acquisition and processing

The IF signal from the mixer output is sampled by a fast ADC board, whereas the sampling clock of the ADC is also generated by the chirp generator to ensure an optimal synchronization of ramp generation and sampling. The ADC's maximum sampling rate is 28.625 MHz. According to Parsivel's theorem ([Hughes 1965](#)), the mean power of the voltage time series, being the sum of the squared sample voltages, equals the sum of the power spectrum over the sampling interval. Thus, applying a Fourier transform to the digitized mixer output voltage provides the power spectrum  $P_n$ , where  $n$  corresponds to a certain IF that is linearly related to  $R$  where the scattering targets are located [see Eq. (3)].

A second Fourier transform of the time series of  $P_n$ , at  $N_{\text{fft}}$  samples, yields the Doppler velocity spectrum  $S_n(v_d)$  (W) depending on the radial velocity  $v_d$  of the scattering targets. The spectrum contains  $N_{\text{fft}}$  points ranging between  $\pm v_N$  ( $\text{m s}^{-1}$ ). The integral over the Doppler power spectrum equals  $P_n$ :

$$P_n = \sum_{v_d=-v_N}^{v_N} S_n(v_d), \quad (7)$$

where  $P_n$  is then converted into the power incident on the antenna  $P_m$  using Eq. (1). The equivalent radar reflectivity factor  $Z_e$  ( $\text{mm}^6 \text{ m}^{-3}$ ; called reflectivity) is obtained from the ratio between  $P_m$  and transmitted power  $P_T$  (W) using the radar equation

$$Z_e = \frac{P_m}{P_T} \frac{5.12 \times 10^{20} \ln(2) \lambda^2 R^2}{G_T^2 \theta^2 \pi^3 |K_w|^2 \delta R}, \quad (8)$$

where  $K_w$  is related to the dielectric constant of liquid water and is assumed to be 0.86 at 90 GHz. Furthermore,  $Z_e$  depends on the half-power beamwidth  $\theta$  (rad), the transmitter gain  $G_T$ , the transmitted wavelength  $\lambda$  (m), and  $\delta R$ . After subtracting the noise power from the spectrum, the moments, such as the reflectivity, the mean Doppler velocity  $v_m$  ( $\text{m s}^{-1}$ ), and the spectral width  $\sigma$  ( $\text{m s}^{-1}$ ), can be calculated (e.g., [Acquistapace et al. 2017](#)).

The radar software conducts "level 1" processing, that is, it determines the noise level of the spectra and calculates spectral moments. Moreover, visualization tools are available for instantaneous data monitoring. The detection threshold for a valid sample is a multiple of the noise density standard deviation above the mean noise density of the Doppler spectrum, which must be exceeded in the spectrum. For more details, we refer the reader to [Görsdorf et al. \[2015, parameter  \$Q\$  in Eq. \(14\) is the "noise filter"\]](#).

### c. Doppler spectra

Example spectra are shown in [Fig. 4](#) at three different heights of a precipitating cloud. Particles moving toward the radar have a negative velocity. The noise level was determined using the Hildebrand–Sekhon scheme ([Hildebrand and Sekhon 1974](#)). The top panel illustrates a Gaussian-shaped power spectrum of a sample volume that contained ice particles exhibiting a mean Doppler velocity of  $-1 \text{ m s}^{-1}$ . The second power spectrum was sampled within the melting layer showing a negative skewness, a broadening of the spectrum, and a shift to more negative velocities, which indicate the acceleration of melting ice particles. The third panel exhibits a broad spectrum that is

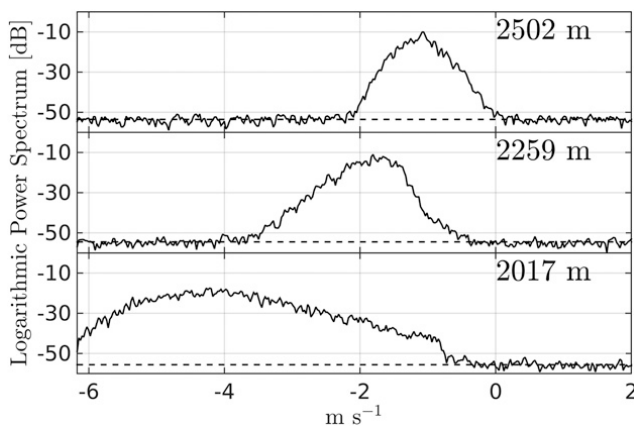


FIG. 4. Example Doppler spectra of JOYRAD-94 (top) above, (middle) within, and (bottom) below the melting layer. Negative velocities indicate motion toward the radar. The integration time was 0.5 s. The mean noise level is indicated (dashed line).

typical for regions below the melting layer, where a mixture of liquid particles with different velocities was present.

The lhs of the third panel indicates that the sample volume contained particles whose fall velocities were close to the Nyquist velocity. At lower range gates, particles were present that exceeded the Nyquist velocity (not shown here). If particles move faster than  $v_N$ , then their spectral signal will occur in the upper or lower range gates at the opposite side of spectrum (folding of velocities), depending on whether their motions are toward or away from the radar. This process is the so-called aliasing. The spectra were recorded in a measurement mode that was not defined for precipitation studies. If studying precipitation is the main objective, then either the settings can be adjusted to increase  $v_N$  or the Doppler spectrum can be dealiased in the postprocessing (e.g., Maahn et al. 2015). Moreover, in section 6 we will introduce a new method to dealias Doppler spectra that combines measurements of two collocated radars providing spectra in high vertical resolution (5 m) while enhancing the limits of  $v_N$ .

#### d. The chirp table

The current measurement modes that are operated on the radar run with a sampling rate of approximately 8 MHz. The Nyquist limit restricts the maximum IF, which can be sampled distinctly, to 4 MHz. Moreover, the chirp generator's phase noise contaminates IFs below 300 kHz. Therefore, the usable IF signal band is limited to frequencies between 300 and 4 MHz. Because the IF bandwidth determines the maximum unambiguous range, a range from 0 to 12 km cannot be covered by a single chirp sequence. Therefore, several chirp sequences are executed consecutively, whereas for each chirp sequence the IFs between 300 kHz and

4 MHz span different ranges, for example, 100–400 m in the first chirp sequence, 400–2000 m in the second chirp sequence, etc. As a consequence, the final profile is a composite of several chirp sequences.

On the one hand, this is a disadvantage, since the data in different chirp sequences were recorded at different times. On the other hand, the sequence of different chirps provides the opportunity to define several parameters, such as  $\delta R$  and  $v_N$ , for each chirp sequence individually. Thus, the observational settings can be adjusted to several atmospheric regions, for example, a large  $v_N$  in the lower boundary layer to capture precipitation events and a high vertical resolution in regions where the melting layer is expected for studying phase conversion processes. The radar software allows for defining up to 10 different chirp sequences. The total duration of one full measurement cycle is mainly determined by the duration of the individual chirp sequences.

Currently, the radar is operated in two modes: the standard mode (SM) and the high-vertical-resolution mode (HRM). The former operates with vertical resolutions between 16 and 34 m, with Doppler velocity resolutions ( $\Delta v$ ) between 3.9 and 1.7  $\text{cm s}^{-1}$  and with  $v_N$  from  $\pm 9.7$  to  $\pm 4.2 \text{ m s}^{-1}$ . The latter runs with a vertical resolution of about 5 m between 100 and 3000 m, whereas the  $v_N$  is minimum at  $\pm 4.2 \text{ m s}^{-1}$  in the lowest 1200 m. The parameter  $\Delta v$  is about 2  $\text{cm s}^{-1}$  in all ranges. In both modes the maximum unambiguous range is 10 km, and the time differences between the first and last chirp sequences is smaller than 2 s. An overview is given in Table 2.

To avoid second-trip echoes, the maximum unambiguous range must be sufficiently large. However, increasing the maximum unambiguous range decreases the maximum unambiguous velocity (see section 3a). On the one hand, this can be a disadvantage, as aliasing becomes likely in lower layers, though it can be corrected, as will be shown in section 6b. On the other hand, it is likely that the transmitted signal at 94 GHz will be attenuated entirely before reaching regions above 10 km, if a convective precipitating cloud system is present. Nevertheless, there is the opportunity to define a measurement mode with two different chirp tables being executed alternately to enable observations of both high clouds and precipitation.

## 4. Radar–radiometer performance

Note that the data presented in the following were collected over a time frame (October 2015–May 2017) in which the sensitivity of JOYRAD-94 was decreased by two reasons: (i) the transmitter power chip

TABLE 2. Main attributes of two radar operation programs: SM and HRM. Several parameters, such as range resolution,  $\Delta v$ , and  $v_N$ , are adjustable for defined range gates. The selection of the former determines other parameters, such as  $N_{\text{fft}}$ , the number of spectral averages ( $n_{\text{Avg}}$ ), and integration time  $\tau$ . The HRM sensitivity was obtained from data collected in Ny-Ålesund. Total sample time for SM is 3 s and HRM 2.5 s. The maximum unambiguous range is in both modes: 10 km.

| The standard mode (SM)                  |                |                                  |                            |                   |                  |                  |            |
|---|----------------|----------------------------------|----------------------------|-------------------|------------------|------------------|------------|
| Range (m)                               | $\Delta R$ (m) | $\Delta v$ (cm s <sup>-1</sup> ) | $v_N$ (m s <sup>-1</sup> ) | Sensitivity (dBZ) | $N_{\text{fft}}$ | $n_{\text{Avg}}$ | $\tau$ (s) |
| 100 to 400                              | 16             | 3.9                              | 9.7                        | -67 to -59        | 128              | 8                | 0.34       |
| 400 to 1200                             | 21.3           | 3.3                              | 8.1                        | -59 to -51        | 256              | 8                | 0.40       |
| 1200 to 3000                            | 26.9           | 2.5                              | 6.2                        | -51 to -43        | 512              | 8                | 0.53       |
| 3000 to 10 000                          | 34.1           | 1.7                              | 4.2                        | -48 to -38        | 1024             | 16               | 1.77       |
| The high vertical resolution mode (HRM) |                |                                  |                            |                   |                  |                  |            |
| 100 to 400                              | 4              | 2.5                              | 6.2                        | -62 to -53        | 512              | 8                | 0.53       |
| 400 to 1200                             | 5.3            | 1.7                              | 4.2                        | -56 to -48        | 512              | 6                | 0.59       |
| 1200 to 3000                            | 6.7            | 2.1                              | 2.5                        | -49 to -42        | 256              | 9                | 0.73       |
| 3000 to 10 000                          | 17             | 2.1                              | 2.5                        | -45 to -35        | 256              | 7                | 0.57       |

degraded rapidly because of a production failure until it was replaced in April 2016, which caused a decrease in sensitivity; and (ii) the detection threshold (see section 3b) was calculated wrongly in the first software version, by not considering coherent averaging, which led to an additional loss of sensitivity by about 3 dB. The software was updated in February 2017.

#### a. Case study

The performance of the radar–radiometer is evaluated using a 24-h measurement period of 5 November 2015, which is shown in Fig. 5. Several precipitation events passed JOYCE during this day. These were mainly triggered by the southwesterly inflow of warm and moist air over central Europe during the days before and an overpass of an elongated trough at 500 hPa from 4 to 6 November. The precipitation event in the morning was the tail of a convective system occurring the night before. The intensification of precipitation between 0100 and 0200 UTC is clearly visible by the increasing reflectivities in Fig. 5 (top).

The overlay of the ceilometer cloud-base height reveals a liquid cloud layer at the top of the cloud that was present between 0300 and 0500 UTC. It also shows the advantage of a radar in comparison to a ceilometer, as the radar captured ice particles below that were not detected by the ceilometer. JOYRAD-94 even detects clouds having a thickness of a few tens of meters; however, very thin liquid layers—for example, between 0800 and 0900 UTC—were beyond the sensitivity of the radar, mainly because of the too-conservative detection threshold in the first software version.

The second precipitating system crossed JOYCE between 2000 and 0200 UTC in night from 5 to 6 November. The transmitter power is automatically

regulated to prevent the receiver from saturation when high reflecting particles, such as large raindrops, are present. Such events involve strong attenuation so that complete attenuation is possible at low altitudes, for example, as visible in Fig. 5 at 2230 UTC, where the reflectivity is significantly reduced after 2 km (yellow vertical stripe). Here, the transmitted power was decreased from 1.5 to 0.2 W between 2200 and 2300 UTC when precipitation produced an increased reflectivity signal. On the one hand, this causes a loss of information from higher cloud levels; on the other hand, it keeps the detector in its linear regime, thus, it increases data quality in lower levels.

The brightness temperature  $T_B$ , being the Planck equivalent temperature for the measured radiation, of the 89-GHz radiometer channel is also shown in the bottom panel of Fig. 5. The correlation between the liquid layers detected by the ceilometer and  $T_B$  is evident. Even very thin clouds, such as occurring at 0530 and 0630 UTC, give a signature in the 89-GHz channel (because the y axis of the brightness temperature plot spans a range of 250 K, small signatures of a few kelvins cannot be recognized in this illustration).

The  $T_B$  signal responds strongest to the two precipitation events: (i) between 0100 and 0200 UTC and (ii) between 2200 and 2300 UTC. The amplitudes of  $T_B$  suggest that the early morning event carried more liquid than the evening event. This is confirmed by the rain gauge measurement 100 m next to JOYRAD-94, which detected a peak rain rate of 1.2 mm (10 min)<sup>-1</sup> at 0200 UTC and only 0.2 mm (10 min)<sup>-1</sup> at 2300 UTC.

In this section, we showed that the passive channel complements the radar measurements while observing the same scene. In section 6, we will further discuss the performance of LWP retrievals using  $T_B$  at 89 GHz.

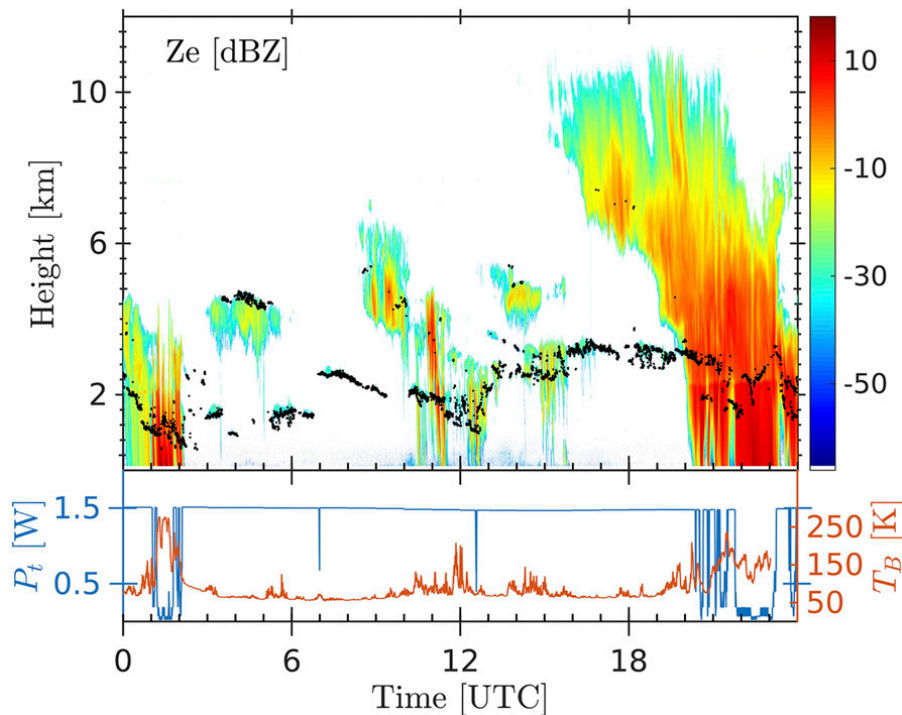


FIG. 5. The 24-h time series of JOYRAD-94 measurements at JOYCE on 5 Nov 2015. (top) Radar reflectivity. Cloud-base height from a collocated ceilometer at 3-m distance (black dots). (bottom) Brightness Temperature  $T_B$  at 89 GHz (red) and transmitter power  $P_T$  (blue).

### b. Sensitivity

The sensitivity of JOYRAD-94 is illustrated in Fig. 6a. It shows the occurrence frequencies of observed reflectivities at each range bin when the radar has operated in the SM at JOYCE. Only signals that exceeded the reflectivity threshold were taken into account. The figure reveals several features that correspond to certain cloud types or specific positions within the cloud.

The area around the maximum at about 8.5 km and  $-25$  dBZ corresponds to high-altitude ice clouds that were often connected to precipitating systems (e.g., as shown in Fig. 5) that occurred frequently during the observation period between November 2015 and March 2016. The occurrence of precipitating systems is reflected in the area around 10 dBZ between 0- and 2-km height when precipitation caused strong echoes. While combining Cloudnet data and synoptic maps, we found that the region of increased occurrences, connecting the maximum at the ground and at about 8.5 km, is mainly caused by cumulonimbus clouds associated with frontal passages over western Germany. Further cloud types that occurred frequently during the observation period were nonprecipitating cumulus and stratocumulus containing hydrometeors in the liquid phase. The fingerprints of these cloud events

are evident in the local maximum between 500- and 2000-m altitude, exhibiting typical values from  $-40$  to  $-20$  dBZ (e.g., Frisch et al. 1995; Wang and Geerts 2003). The distinct bimodal signature in this region was also observed by a collocated 35-GHz pulsed radar, which is an interesting meteorological feature; however, a detailed analysis of the data and the synoptic conditions used to explain the bimodality is not part of this study.

A gap is visible at the sensitivity limit of JOYRAD-94 at about 7.8 km. It was found that a signal originating from ADC board electronics contaminates the signal processing. The signal's frequency is equal to the IF frequency that corresponds to the range gate at about 7.8 km. To remove this contamination, the intrinsic noise underground in each IF bin was determined and stored. During operation, the contamination's amplitude is subtracted from the monitored signal, which causes the gap in Fig. 6a, indicating that the logged value of the contamination signal was overestimated.

Fitting a curve to the lowest detected reflectivities (Fig. 6a) provides the sensitivity of the radar for the SM at JOYCE after filtering the data with the detection threshold discussed in section 3b. Moreover, the sensitivity was determined for each month of operation individually, showing a shift of the sensitivity curve toward larger reflectivities with advancing time. The loss of



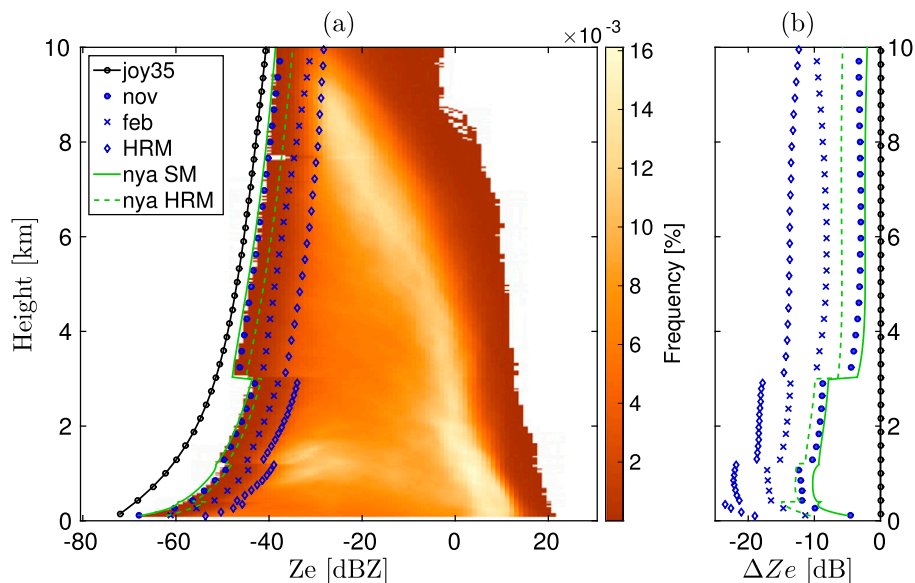


FIG. 6. (a) Histogram of  $Z_e$  from 20 Oct 2015 until 23 Mar 2016, for the SM of JOYRAD-94 with sensitivity fit (blue filled dots). Additionally, fits to histograms of different months, the HRM, and JOYRAD-35 for the period 20 Oct 2015–23 Mar 2016 are shown: the blue curves show the sensitivity of JOYRAD-94 derived (i) from data collected in the SM during November 2015 (blue filled dots); (ii) from data collected during February 2016 (blue crosses); and (iii) from data recorded in the HRM during March 2016 (blue diamonds). The green lines show the sensitivities for JOYRAD-94 after replacing the transmitter power chip and installing JOYRAD-94 at NyA. The black curve indicates the sensitivity of JOYRAD-35. (b) Sensitivity difference with respect to JOYRAD-35.

sensitivity is due to the degradation of an erroneous transmitter power chip implemented in the prototype. The transmitter power chip was replaced in April 2016 and since then the transmitter power has been stable. Note that the curve of the HRM is also influenced by sensitivity losses caused by a higher vertical resolution.

In June 2016, the radar was installed in Ny-Ålesund (NyA), where the radar operated in the HRM and the SM. A software update in February 2017, with improved signal detection thresholds, further increased the sensitivity by 3 dB. The comparison of the resulting sensitivity profiles before and after the replacement, and the software update in Fig. 6a reveals that the sensitivity in the SM has improved with respect to the early time of installation at JOYCE when the power chip was still working properly. We find that the sensitivity loss in the HRM observed at JOYCE is mainly a result of the chip degradation and a too conservative detection threshold; the differences of the HRM and the SM with the new chip are smaller than 6 dB in the lowest 500 m and smaller than 4 dB above.

As clearly visible in Fig. 6a, jumps in the sensitivity occur at several heights. These are caused by different chirp sequences used for probing different altitude regions. In general, a finer vertical resolution leads to a lower sensitivity and vice versa. Because the vertical

resolution often changes from chirp to chirp, the sensitivity changes accordingly. The sensitivity limits for all layers in both operation modes are summarized in Table 2.

We further assess the performance of JOYRAD-94 by comparing it to a pulsed 35-GHz radar (JOYRAD-35), as described by Görtsdorf et al. (2015), which was located at 3 m distance to JOYRAD-94 at JOYCE. The sensitivity curve of JOYRAD-35 is also included in Fig. 6 as a reference. Clearly evident is the higher sensitivity of JOYRAD-35 in the lowest 3 km (Fig. 6b), which is due to the much higher average transmitter power of 24 W (Acquistapace et al. 2017, their Table 2) and the short integration times in the HRM and SM in the lowest layer. These differences in sensitivity are on the order of 10 dB (15 dB) in the lowest kilometer for the SM (HRM) but reduce to 3 dB (8 dB) above 3 km. These sensitivity differences also affect the analysis in the following section. Note that increasing the integration time of JOYRAD-94 by 0.5 s in the lowest layer would increase the sensitivity by about 3 dB.

## 5. Assessment of cloud detection

The following analysis is based on the Cloudnet product of Illingworth et al. (2007), combining several

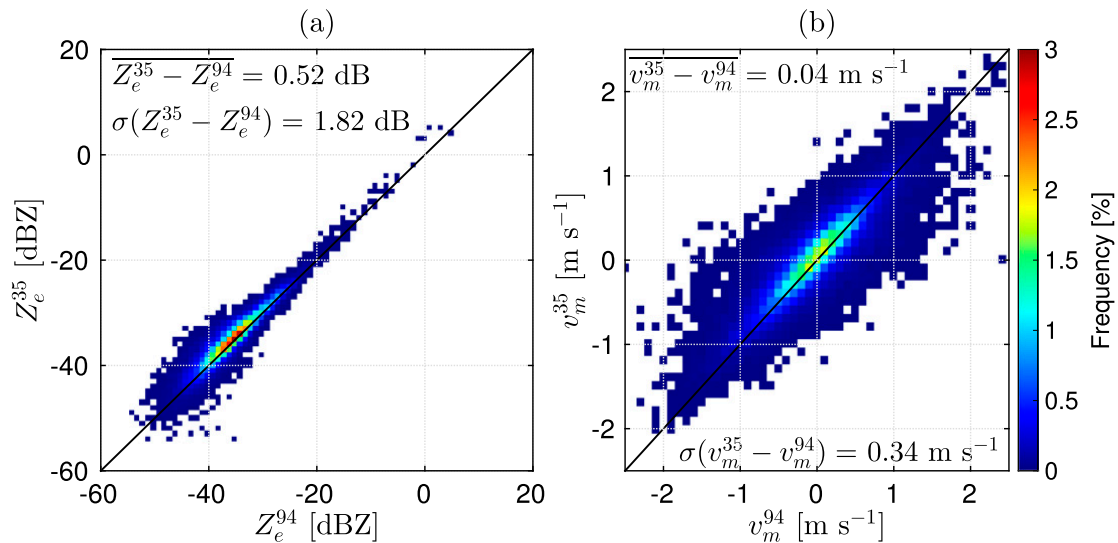


FIG. 7. Scatter histograms of (a) reflectivities and (b) mean Doppler velocities of JOYRAD-94 and JOYRAD-35, which were observed at the cloud center of single-layer liquid clouds having a cloud base above 200 m.

remote sensing instruments (e.g., radar, lidar, and MWR) and reanalysis data to classify cloud properties such as vertical thickness, phase, and hydrometeor type. Cloudnet provides a target classification with a vertical resolution of 30 m, allowing for checking which hydrometeor types are present in the observed atmospheric column. We compared the performances of JOYRAD-94 and JOYRAD-35 for two cloud types: (i) single-layer nonprecipitating liquid clouds with a cloud base higher than 200 m and (ii) single-layer nonprecipitating ice clouds with a cloud base higher than 200 m. These cloud types were selected to ensure that both radars operate in the Rayleigh regime so that a comparison of reflectivities is reasonable.

The minimum cloud base was selected to ensure that the clouds were observed in the far field of both radars. A cloud was considered to be precipitating if either drizzle, rain, or melting ice particles, or a combination of these three, were connected to the cloud or were detected within the cloud. Falling ice particles were not defined as precipitation (Illingworth et al. 2007).

The Cloudnet product is derived with 30-s temporal and 30-m vertical resolution. We considered only data that were recorded by both radars simultaneously and within  $\pm 10$  s of a Cloudnet data point while either a single-layer liquid cloud or a single-layer ice cloud was present. The vertical resolution of JOYRAD-35 was 29 m. JOYRAD-94 was operated in the SM; that is, the resolution varied between 16 and 34 m (see Table 2). Height matching was performed using nearest neighbor comparison. The integration time of JOYRAD-35 was 2 s. The integration time of JOYRAD-94 varied with height between 0.34 and 1.77 s (see Table 2). No

corrections concerning gaseous and liquid or ice attenuation were applied to the data, since neither measurements of humidity and temperature profiles nor measurements of integrated water vapor (IWV) are available for this period at JOYCE.

#### a. Liquid clouds

After selecting single-layer liquid clouds using the Cloudnet classification scheme (a total of 41 791 cases), we investigated the performance of both radars at the cloud center. The cloud center was chosen to exclude the effects of partial beamfilling at cloud edges. The position of the cloud center was calculated from the Cloudnet cloud base and cloud top. Only in 73% of the cases was a signal simultaneously detected by both radars. This is due to the higher sensitivity of JOYRAD-35 compared to JOYRAD-94, especially because of transmitter chip degradation in JOYRAD-94 during the initial deployment at JOYCE and the too conservative detection threshold. If JOYRAD-94 had observed continuously with its nominal reflectivity (see Fig. 6a, “NyA SM”), liquid clouds would have been detected simultaneously in 97% of the cases.

Figure 7 shows scatter histograms of the radar reflectivity and the mean Doppler velocity for simultaneously detected single-layer liquid clouds. Most cases reveal reflectivities between  $-40$  and  $-30$  dBZ, corresponding to the area of enhanced occurrence between 1 and 2 km in Fig. 6a. Both radars agree with a mean difference of 0.52 dB and a standard deviation of 1.82 dB. The mean Doppler velocities agree well, showing a mean difference of  $0.04 \text{ m s}^{-1}$  with a standard deviation of  $0.34 \text{ m s}^{-1}$ .

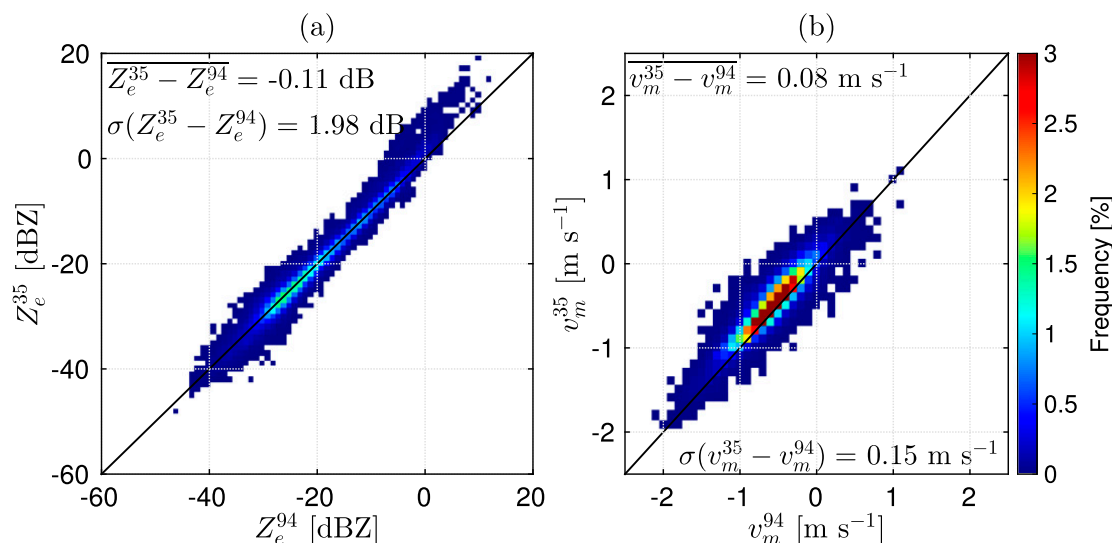


FIG. 8. Scatter histograms of (a) reflectivities and (b) mean Doppler velocities of JOYRAD-94 and JOYRAD-35, which were observed at the cloud center of single-layer ice clouds having a cloud base above 200 m.

### b. Ice clouds

We classified 49 556 cases as single-layer ice clouds; 93% of the cases were observed simultaneously by JOYRAD-35 and JOYRAD-94. The higher percentage with respect to liquid clouds is due to higher reflectivities that are associated with these clouds, as can be seen in Fig. 8a; that is, the sensitivity limit of JOYRAD-94 was mostly exceeded. If JOYRAD-94 had measured with its nominal reflectivity, ice clouds would have been detected simultaneously in 99% of the cases.

The majority of reflectivities are found between  $-30$  and  $-20$  dBZ, which corresponds to the area of enhanced occurrence in Fig. 6a between 6 and 8 km. The values between  $-20$  and  $-5$  dBZ predominantly originate from the area in Fig. 6a connecting the maximum at 8.5 km and at the ground. The distribution in the scatterplot in Fig. 8a starts to deviate from the 1:1 line for  $Z_e$  values larger than  $-10$  or  $-5$  dBZ. Here, the resonance-scattering regime is reached at 94 GHz, while the Rayleigh approximation is still valid at 35 GHz. The mean difference between the two radars is  $-0.11$  dB with a standard deviation of 1.98 dB.

The mean Doppler velocities are concentrated between  $-1$  and  $0$   $\text{m s}^{-1}$ , which are characteristic for ice particles in high altitudes (e.g., Heymsfield and Iaquinta 2000). Again, a positive offset is evident, but still both radars agree with a mean difference of  $0.08 \pm 0.15$   $\text{m s}^{-1}$ .

### c. Comparative uncertainty estimate

The velocity offset has the same sign for liquid and ice clouds. This indicates that the velocity offset is due to a relative mispointing, that is, either one of the radars or

both were not exactly aligned to zenith. Kneifel et al. (2016) found that a slight relative mispointing of  $1^\circ$  elevation produces a velocity offset of  $0.1$   $\text{m s}^{-1}$ , which is already larger than the offset found here.

Since corrections for gaseous and liquid attenuation could not be applied, a quantitative estimate for calibration accuracies cannot be drawn from the comparison of the radars' reflectivities. All attenuating effects—that is, liquid and gaseous attenuation effects, as well as differential scattering at large particles—cause positive reflectivity offsets, that is,  $Z_e^{35} - Z_e^{94} > 0$ . Hence, a negative offset, as revealed in Fig. 8a, must be due to an offset in calibration.

When comparing Fig. 8a to Fig. 7a, the differential attenuation becomes larger by about 0.6 dB; that is, the offset turns positive. On the one hand, this offset could be explained by attenuation by liquid water. At JOYCE, nonprecipitating single-layer liquid clouds exhibit averaged LWC values of about  $0.1$   $\text{g m}^{-3}$  and smaller while having vertical extents of about 500–1000 m (Löhnert et al. 2015). This induces a two-way attenuation from the cloud base to the cloud center of about 0.4–0.7 dB (Hogan et al. 2005). On the other hand, it is possible that the average magnitude of the gaseous attenuation differed between the liquid cloud and ice cloud cases. Because the mean altitudes of the cloud centers were 1.2 and 6.1 km for liquid and ice clouds, respectively, we assume that gaseous attenuation has been weaker during liquid cloud events, which could compensate for the differential attenuation by liquid water. The differential two-way attenuation by water vapor is about 1 dB for the lowest 5 km for values of about  $10$   $\text{kg m}^{-2}$  IWV (Kneifel et al. 2015), being typical for fall and winter at JOYCE

(Löhnert et al. 2015). Further, attenuation by oxygen can be up to 0.5 dB for the entire atmosphere. We estimate the decrease in reflectivity difference from Fig. 8a to Fig. 7a to be smaller than 1 dB, though sufficient to compensate attenuation effects by liquid water; that is, we would expect a similar value for  $Z_e^{35} - Z_e^{94}$  in both figures. Regarding the latter and that a calibration cross-check with a metal sphere was performed only for JOYRAD-94, the calibration offset between both radars is likely larger than 0.5 dB and perhaps as much as 2 dB.

## 6. New opportunities for cloud observations

This section presents the novelties for cloud observations that arise from JOYRAD-94 that have optimally matched active and passive components. Moreover, we show that it is possible to overcome the trade-off between Nyquist velocity and range resolution without losing temporal resolution when combining data from two radars with different settings.

### a. Liquid water path retrieval at 89 GHz

Optimal beam matching between a radar and a radiometer provides instantaneous signatures as was shown in section 4. To make use of these signatures, retrievals are necessary that add information to the radar measurement. Frisch et al. (1998) demonstrated that the vertical distribution of liquid water can be obtained when combining the LWP from a radiometer and radar reflectivity measurements. The liquid water path can be derived from a microwave radiometer at window frequencies, where clear-sky attenuation is low, for example, at 31 or 89 GHz. However, because of the water vapor absorption continuum in the microwave (Rosenkranz 1998), additional information on IWV is needed to constrain retrievals.

The retrievals, presented in the following, are quadratic models:

$$\text{LWP} = a_0 + \sum_{i=1}^k (a_{i,1}x_i + a_{i,2}x_i^2), \quad (9)$$

where  $x_i$  represents one of  $k$  input parameters (e.g., using  $T_B$  at 89 GHz and IWV:  $\text{LWP} = a_0 + a_{1,1}T_B + a_{1,2}T_B^2 + a_{2,1}\text{IWV} + a_{2,2}\text{IWV}^2$ ). The coefficients  $a_0$  and  $a_{i,j}$  were obtained from a least squares regression. The training dataset contains 15 175 radiosondes launched in De Bilt, the Netherlands, which is located 160 km northwest of JOYCE. Clouds were added by applying a relative humidity threshold of 95% for cloud presence and were modeled with a modified adiabatic approach as done by Löhnert and

Crewell (2003). The parameter  $T_B$  was modeled after Rosenkranz (1998) using the water vapor continuum correction by Turner et al. (2009). The retrievals were performed for clouds with LWPs smaller than  $1.5 \text{ kg m}^{-2}$ , since most single-layer liquid clouds at JOYCE have smaller LWPs (Löhnert et al. 2015). Note that the training datasets provide information representative of the atmospheric conditions close to the measurement location; however, it should not be considered as ground truth.

Figure 9 shows the performance of an LWP retrieval using only the 89-GHz channel as the input parameter in Eq. (9) (Fig. 9a) and using the 89-GHz channel with additional information on the integrated water vapor from an external source with a random uncertainty of  $\pm 2 \text{ kg m}^{-2}$  (e.g., short-term model forecast; Fig. 9b). We assumed an uncertainty of 0.5 K for  $T_B$  when deriving the regression coefficients, which accounts for the RMS uncertainty of the 89-GHz radiometric channel (see section 2c). The retrieval using only the 89-GHz channel has an RMS uncertainty (not including potential biases, i.e., calibration offsets) of about  $44 \text{ g m}^{-2}$ . When including the IWV in the retrieval algorithm, this uncertainty decreases to about  $15 \text{ g m}^{-2}$ .

For comparison we ran the retrieval algorithm using only seven frequencies between 20 and 31 GHz, which are commonly used for LWP (e.g., Löhnert and Crewell 2003). The RMS uncertainty of this retrieval was  $25 \text{ g m}^{-2}$ , being 60% larger than the RMS uncertainty of the retrieval combining 89 GHz and the IWV from an external source. This is due to the 89-GHz channel being more sensitive to liquid water than the 31-GHz channel. Combining  $T_B$  measurements along the water vapor absorption line at 22.235 GHz with measurements at 89 GHz would further improve the retrieval performance.

### b. Dual-radar dealiasing of Doppler spectra

On the one hand, operating JOYRAD-94 in the HRM provides vertical highly resolved data; on the other hand, the Nyquist velocity is small; hence, aliasing is likely when observing strongly turbulent clouds or precipitation. Maahn and Kollias (2012) introduced a method to dealias Doppler spectra recorded by a rain FMCW radar operating at 24 GHz. A stand-alone pulsed radar must vary the pulse repetition frequency to obtain the real atmospheric signal, which decreases the effective observation time (e.g., Holleman and Beekhuis 2003; Sosnytskiy 2014). In FMCW radar data, aliasing produces a folding into the upper (lower) range gate for particles having an absolute radial velocity larger than  $v_N$  toward (away from) the radar. Hence, unfolding can be simply applied by

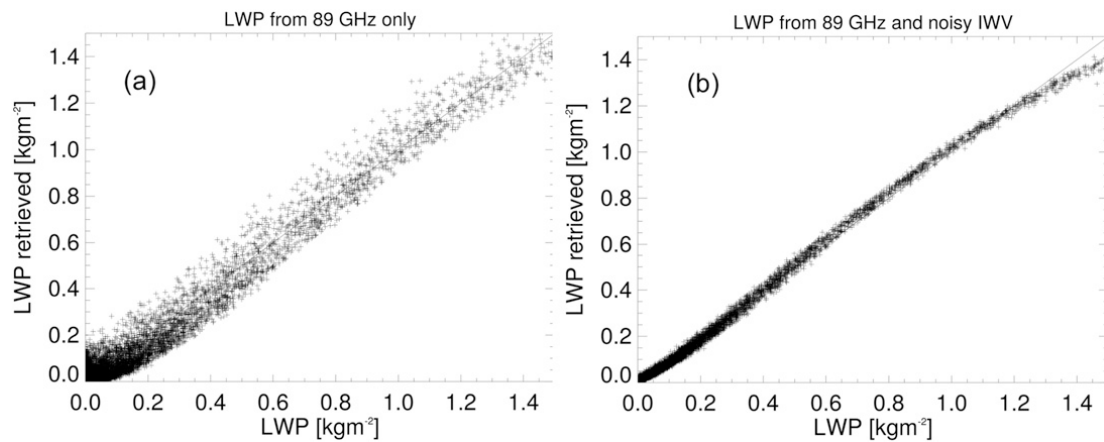


FIG. 9. (a) LWP retrieval using only 89 GHz deviates on average by  $118 \pm 44 \text{ g m}^{-2}$  from the model truth ( $x$  axis). (b) LWP retrieval using 89 GHz plus IWV from an external source with  $\pm 2 \text{ kg m}^{-2}$  accuracy (“noisy IWV”) deviates on average by  $118 \pm 15 \text{ g m}^{-2}$  from the model truth. Retrievals were performed with 15 175 radiosonde profiles to which clouds were added using a modified adiabatic approach.

concatenating spectra from neighboring range gates (Maahn and Kollias 2012). However, a robust first guess for the true radial velocity is needed, especially if  $v_N$  is small and double folding may have occurred.

Using two radars that operate simultaneously, having opposite settings with respect to  $v_N$  and vertical resolution, makes unfolding possible without creating a time mismatch (pulsed radars) and without selecting the wrong part of the concatenated spectrum (FMWC radar). Therefore, the mean Doppler velocities of JOYRAD-35 were used as an initial first guess when unfolding the spectra. Figure 10 shows a flowchart of the dual-radar dealiasing method (DRDM) that was applied to the HRM data of JOYRAD-94. First, the spectrum of JOYRAD-94 is quintupled, concatenating the spectra from the next two range gates on each side. In the next step, the maximum closest to the initial-guess velocity from JOYRAD-35 is identified. In the third and final step, the spectrum is centered so that the contributions of the neighboring range gates are minimized. Therefore, the center of the spectrum is shifted within  $\pm 0.25N_{\text{fit}}$  until the minimum sum of the first and last spectral entries is found.

Figure 11 shows two comparisons of mean Doppler velocities of JOYRAD-94 ( $v_m^{94}$ ) and JOYRAD-35 ( $v_m^{35}$ ) based on one month of HRM data. In Fig. 11a,  $v_m^{94}$  was calculated from raw spectra and in Fig. 11b from spectra that were preprocessed with the DRDM. The scatter around the one-to-one line is reduced so that mean Doppler velocities smaller than  $-5 \text{ m s}^{-1}$  can also be detected. However, the DRDM does not work perfectly, which is visible in Fig. 11b, when the DRDM overestimates the absolute fall velocity in some cases.

The DRDM is simple and computationally inexpensive. Moreover, a prior evaluation of signal quality

can further decrease the computing time (Maahn and Kollias 2012). The disadvantages are clearly that bimodal spectra with fully separated peaks could be cut when the third step of the DRDM is conducted. This can be compensated for when including a further processing step that looks for secondary peaks in the spectra. Moreover, if the spectrum is broader than the  $2v_N$ , a clean unfolding will not be possible anymore, since signal interference will occur in the neighboring range gates. Nevertheless, the results in Fig. 11 show that the DRDM improves the calculation of higher moments and therefore the quality of retrievals. Additionally, the DRDM now allows for obtaining vertically high resolved spectra while minimizing the restriction due to  $v_N$ .

The choice of the maximum unambiguous velocities ( $v_{Nw}$  and  $v_{Nn}$  with indexes “ $Nw$ ” and “ $Nn$ ” for wide and narrow mode, respectively) depends on the maximum mean Doppler velocities and the spectral widths that are expected at the observational site. To be able to reconstruct full spectra with the noise floor,  $2v_{Nn}$  has to be larger than the velocity range covered by the spectra that are expected, which depends both on the particle size distribution and turbulence. Parameter  $v_{Nw}$  should be chosen large enough to cover large fall velocities and small enough to have a range resolution that is not too coarse with respect to the  $Nn$  mode to avoid that mean Doppler velocities of the two instruments differ by more than  $v_{Nn}/2$  when comparing nearest range gates. Otherwise, dealiasing will not be unambiguous without additional information. In the dataset recorded in Ny-Ålesund, we found turbulence-induced changes in vertical velocity of more than  $5 \text{ m s}^{-1}$  within 30 m.

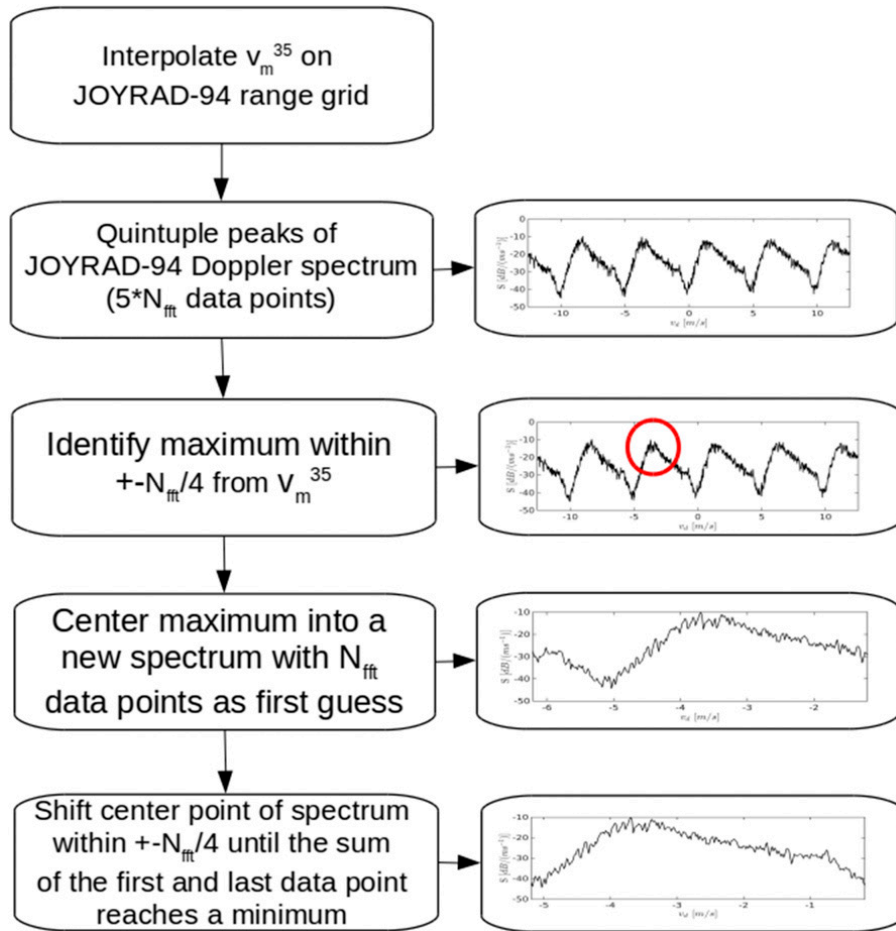


FIG. 10. Flowchart of the DRDM using  $v_m^{35}$  and the Doppler spectra of JOYRAD-94. A single spectrum contains  $N_{\text{fit}}$  points, which is concatenated with the next two range gates on each side. After identifying the maximum that is closest to  $v_m^{35}$ , the spectrum is centered so that, in case of a broad spectrum, contributions from neighboring range gates are minimized.

To get a copy of the MATLAB code of the DRDM, please contact the corresponding author of this manuscript.

## 7. Summary and outlook

We presented a new 94-GHz FMCW cloud radar-radiometer (JOYRAD-94) suited for studying cloud microphysical processes and cloud macrophysical properties. JOYRAD-94 is a compact instrument for unattended long-term measurements in all weather conditions. A strong blowing system minimizes adherence of liquid and ice particles on the radome and therefore attenuation effects are avoided. Additionally, the transmitter power can be regulated to prevent the detector from saturation and therefore provide accurate measurements also when strongly reflecting particles are present in the observed column, for example, during precipitation. A further novelty is that the active and

passive components receive over the same antenna; that is, optimal beam matching is accomplished.

The active component of JOYRAD-94 can be accurately calibrated with an uncertainty of  $\pm 0.5$  dBZ. This was shown by observing a metal sphere in the far field of the radar and by a relative comparison to a collocated 35-GHz radar. The calibration of the receiver should be repeated every 3–6 months. The passive broadband channel at 89 GHz has an uncertainty of about  $\pm 0.5$  K. JOYRAD-94 was tested in two different measurement configurations: a standard configuration (SM) with vertical resolutions between 16 and 34 m and a high-vertical-resolution mode (HRM) resolving the lowest 3 km with about 6-m range resolution. In both modes JOYRAD-94 is sensitive enough to capture the majority of clouds. The sensitivity ranges from  $-67$  ( $-61$ ) dBZ at 100 m to  $-38$  ( $-35$ ) dBZ at 10 km when operating in the SM (HRM). The HRM particularly allows for improving observations of small-scale microphysical processes

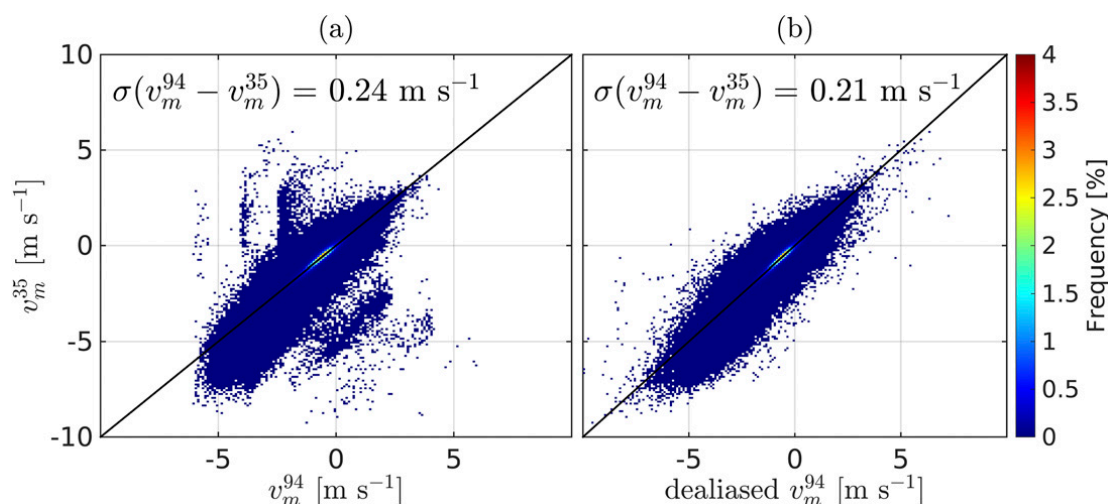


FIG. 11. Scatter histograms of mean Doppler velocities of JOYRAD-94 ( $v_m^{94}$ ) and JOYRAD-35 ( $v_m^{35}$ ) showing (a)  $v_m^{94}$  calculated from original spectra and (b)  $v_m^{94}$  calculated from spectra processed with the DRDM.

(e.g., processes affected by turbulence) and processes comprising a strong vertical gradient such as melting layer or riming within layers of supercooled liquid water.

It is also possible to adjust the measurement mode within up to 10 layers in the vertical column to account for different cloud particle properties at different heights. For example, it can be beneficial to run a coarse range resolution with a large unambiguous  $v_N$  in the lowest layer where precipitation is expected while measuring with 5-m vertical resolution in the region of the melting layer to study conversion processes with high vertical resolution.

It was shown that the passive channel can provide accurate LWP estimates. A model study revealed that the liquid water path can be retrieved with an RMS uncertainty of about  $15 \text{ g m}^{-2}$  when measuring brightness temperatures at 89 GHz and knowing the IWV from an external source with an uncertainty of  $\pm 2 \text{ kg m}^{-2}$ . In addition, systematic offsets—for example, as a result of calibration offsets—have to be taken into account. The information of the 89-GHz channel can be used to identify liquid constituents within the vertical column and to retrieve vertical profiles of liquid water when including radar measurements. The impact of optimally matched beams on the retrieval quality is content of a current study.

We presented a new method to dealias Doppler spectra (DRDM) without losing temporal resolution by using the data of the collocated radar as the initial guess. The DRDM provides vertically highly resolved spectra with an increased  $v_N$ . The next step will be to investigate how the vertically highly resolved profiles help to understand microphysical processes within the cloud but also at cloud edges.

As JOYRAD-94 is a prototype, future versions of this instrument will have to overcome initial teething

troubles: the first version of the transmitter power chip was degrading very fast, which caused a significant loss of sensitivity of 10 dB. However, this problem has already been solved and we showed that the new power chip produces a stable output power. Furthermore, the latest version of the manufacturer's software includes an update of the threshold detection procedure, the optimization of the suppression of the ADC board electronics' signal that contaminates the signal processing, and a dealiasing routine to provide accurate spectra. Next generations will also have the possibility of polarimetric detection and can be mounted on a scanner to derive three-dimensional cloud fields. Moreover, a frequent switching between the two measurement modes will be enabled so that the DRDM can also be applied to single radar measurements when assuming constant conditions within two data samples.

*Acknowledgments.* This work was funded by the project “Energy Transitions and Climate Change” (<http://et-cc.uni-koeln.de/project.html>) of the “Excellence Initiative” of the University of Cologne by the German Research Foundation (DFG) under Grant ZUK 81/1 and by the German research initiative (AC)<sup>3</sup> by the DFG under Grant TRR172/1 (<http://www.ac3-tr.de/>). Contributions by S. Kneifel were carried out within the Emmy-Noether Group OPTIMIce funded by the DFG under Grant KN 1112/2-1. We thank Rainer Haseneder-Lind, Pavel Krobot, Birger Bohn, Alexander Myagkov, and the AWIPEV team in Ny-Ålesund for the technical support; and in particular the three anonymous reviewers for their constructive comments, which helped to improve the manuscript.

## REFERENCES

- Acquistapace, C., S. Kneifel, U. Löhnert, P. Kollias, M. Maahn, and M. R. Bauer-Pfundstein, 2017: Optimizing observations of drizzle onset with millimeter-wavelength radars. *Atmos. Meas. Tech.*, **10**, 1783–1802, doi:10.5194/amt-10-1783-2017.
- Bennett, A., J. Nash, C. Gaffard, B. Moyna, M. Oldfield, and P. Huggard, 2009: Observations from the UK Met Office 94 GHz FMCW cloud radar. *Proceedings of the Eighth International Symposium on Tropospheric Profiling*, A. Apituley, H. W. J. Russchenberg, and W. A. A. Monna, Eds., Organizing Committee of the 8th International Symposium on Tropospheric Profiling, S06-O02, 4 pp., <http://www.cesar-observatory.nl/istp8/pages/index.htm>.
- Borque, P., E. Luke, and P. Kollias, 2016: On the unified estimation of turbulence eddy dissipation rate using Doppler cloud radars and lidars. *J. Geophys. Res. Atmos.*, **120**, 5972–5989, doi:10.1002/2015JD024543.
- Boucher, O., and Coauthors, 2013: Clouds and aerosols. *Climate Change 2013: The Physical Basis*, T. F. Stocker et al., Eds., Cambridge University Press, 571–657.
- Delanoë, J., and Coauthors, 2016: BASTA: A 95-GHz FMCW Doppler radar for cloud and fog studies. *J. Atmos. Oceanic Technol.*, **33**, 1023–1038, doi:10.1175/JTECH-D-15-0104.1.
- Frisch, A. S., C. W. Fairall, and J. B. Snider, 1995: Measurement of stratus cloud and drizzle parameters in ASTEX with a  $K_a$ -band Doppler radar and a microwave radiometer. *J. Atmos. Sci.*, **52**, 2788–2799, doi:10.1175/1520-0469(1995)052<2788:MOSCAD>2.0.CO;2.
- , G. Feingold, C. W. Fairall, T. Uttal, and J. B. Snider, 1998: On cloud radar and microwave radiometer measurements of stratus cloud liquid water profiles. *J. Geophys. Res.*, **103**, 23 195–23 197, doi:10.1029/98JD01827.
- Görsdorf, U., V. Lehmann, M. Bauer-Pfundstein, G. Peters, D. Vavriv, V. Vinogradov, and V. Volkov, 2015: A 35-GHz polarimetric doppler radar for long-term observations of cloud parameters—Description of system and data processing. *J. Atmos. Oceanic Technol.*, **32**, 675–690, doi:10.1175/JTECH-D-14-00066.1.
- Haeffelin, M., L. Barth, and J. Delano, 2005: SIRTa, a ground-based atmospheric observatory for cloud and aerosol research. *Ann. Geophys.*, **23**, 253–275, doi:10.5194/angeo-23-253-2005.
- Heijnen, S. H., L. P. Ligthart, and H. W. Russchenberg, 2000: First measurements with TARA; An S-band transportable atmospheric radar. *Phys. Chem. Earth*, **25B**, 995–998, doi:10.1016/S1464-1909(00)00140-4.
- Heus, T., and H. J. J. Jonker, 2008: Subsiding shells around shallow cumulus clouds. *J. Atmos. Sci.*, **65**, 1003–1018, doi:10.1175/2007JAS2322.1.
- Heymsfield, A. J., and J. Iaquinta, 2000: Cirrus crystal terminal velocities. *J. Atmos. Sci.*, **57**, 916–938, doi:10.1175/1520-0469(2000)057<0916:CCTV>2.0.CO;2.
- Hildebrand, P. H., and R. S. Sekhon, 1974: Objective determination of the noise level in Doppler spectra. *J. Atmos. Sci.*, **13**, 808–811, doi:10.1175/1520-0450(1974)013<0808:ODOTNL>2.0.CO;2.
- Hogan, R. J., D. Bouniol, D. N. Ladd, E. J. O'Connor, and A. J. Illingworth, 2003: Absolute calibration of 94/95-GHz radars using rain. *J. Atmos. Oceanic Technol.*, **20**, 572–580, doi:10.1175/1520-0426(2003)20<572:ACOGRU>2.0.CO;2.
- , N. Gaussiat, and A. J. Illingworth, 2005: Stratocumulus liquid water content from dual-wavelength radar. *J. Atmos. Oceanic Technol.*, **22**, 1207–1218, doi:10.1175/JTECH1768.1.
- Holleman, I., and H. Beekhuis, 2003: Analysis and correction of dual PRF velocity data. *J. Atmos. Oceanic Technol.*, **20**, 443–453, doi:10.1175/1520-0426(2003)20<443:AACODP>2.0.CO;2.
- Huang, D., Y. Liu, and W. Wiscombe, 2008: Determination of cloud liquid water distribution using 3D cloud tomography. *J. Geophys. Res.*, **113**, D13201, doi:10.1029/2007JD009133.
- , E. Campos, and Y. Liu, 2014: Statistical characteristics of cloud variability. Part 1: Retrieved cloud liquid water path at three ARM sites. *J. Geophys. Res. Atmos.*, **119**, 10 813–10 828, doi:10.1002/2014JD022001.
- Huggard, P. G., and Coauthors, 2008: 94 GHz FMCW cloud radar. *Millimetre Wave and Terahertz Sensors and Technology*, K. A. Krapels and N. A. Salmon, Eds., Society of Photo-Optical Instrumentation Engineers (SPIE Proceedings, Vol. 7117), 711704, doi:10.1117/12.800347.
- Hughes, H. K., 1965: The physical meaning of Parseval's theorem. *Amer. J. Phys.*, **33**, 99, doi:10.1119/1.1971337.
- Illingworth, A. J., and Coauthors, 2007: Cloudnet: Continuous evaluation of cloud profiles in seven operational models using ground-based observations. *Bull. Amer. Meteor. Soc.*, **88**, 883–898, doi:10.1175/BAMS-88-6-883.
- , D. Cimini, C. Gaffard, M. Haeffelin, V. Lehmann, U. Löhnert, E. J. O'Connor, and D. Ruffieux, 2015: Exploiting existing ground-based remote sensing networks to improve high resolution weather forecasts. *Bull. Amer. Meteor. Soc.*, **96**, 2107–2125, doi:10.1175/BAMS-D-13-00283.1.
- Kneifel, S., M. S. Kulie, and R. Bennartz, 2011: A triple-frequency approach to retrieve microphysical snowfall parameters. *J. Geophys. Res.*, **116**, D11203, doi:10.1029/2010JD015430.
- , A. von Lerber, J. Tiira, D. Moisseev, K. Kollias, and J. Leinonen, 2015: Observed relations between snowfall microphysics and triple-frequency radar measurements. *J. Geophys. Res. Atmos.*, **120**, 6034–6055, doi:10.1002/2015JD023156.
- , P. Kollias, A. Battaglia, J. Leinonen, M. Maahn, H. Kalesse, and F. Tridon, 2016: First observations of triple-frequency radar Doppler spectra in snowfall: Interpretation and applications. *Geophys. Res. Lett.*, **43**, 2225–2233, doi:10.1002/2015GL067618.
- Kollias, P., B. A. Albrecht, and F. Marks, 2002: Why Mie? *Bull. Amer. Meteor. Soc.*, **83**, 1471–1483, doi:10.1175/BAMS-83-10-1471.
- , E. E. Clothiaux, M. A. Miller, B. A. Albrecht, G. L. Stephens, and T. P. Ackerman, 2007a: Millimeter-wavelength radars: New frontier in atmospheric cloud and precipitation research. *Bull. Amer. Meteor. Soc.*, **88**, 1608–1624, doi:10.1175/BAMS-88-10-1608.
- , —, —, E. P. Luke, K. L. Johnson, K. P. Moran, K. B. Widener, and B. A. Albrecht, 2007b: The atmospheric radiation measurement program cloud profiling radars: Second-generation sampling strategies, processing, and cloud data products. *J. Atmos. Oceanic Technol.*, **24**, 1199–1214, doi:10.1175/JTECH2033.1.
- Küchler, N., D. D. Turner, U. Löhnert, and S. Crewell, 2016: Calibrating ground-based microwave radiometers: Uncertainty and drifts. *Radio Sci.*, **51**, 311–327, doi:10.1002/2015RS005826.
- Lhermitte, R. M., 1987: A 94-GHz Doppler radar for cloud observations. *J. Atmos. Oceanic Technol.*, **4**, 36–48, doi:10.1175/1520-0426(1987)004<0036:AGDRFC>2.0.CO;2.
- Ligthart, L. P., and L. R. Nieuwkerk, 1980: F.M.-C.W. Delft atmospheric research radar. *IEE Proc.*, **127F**, 421–426, doi:10.1049/ip-f-1:19800061.
- Löhnert, U., and S. Crewell, 2003: Accuracy of cloud liquid water path from ground-based microwave radiometry 1.



- Dependency on cloud model statistics. *Radio Sci.*, **38**, 8041, doi:10.1029/2002RS002654.
- , and Coauthors, 2015: JOYCE: Jülich Observatory for Cloud Evolution. *Bull. Amer. Meteor. Soc.*, **96**, 1157–1174, doi:10.1175/BAMS-D-14-00105.1.
- Luke, E. P., and P. Kollias, 2013: Separating cloud and drizzle radar moments during precipitation onset using Doppler spectra. *J. Atmos. Oceanic Technol.*, **30**, 1656–1671, doi:10.1175/JTECH-D-11-00195.1.
- Maahn, M., and P. Kollias, 2012: Improved Micro Rain Radar snow measurements using Doppler spectra post-processing. *Atmos. Meas. Tech.*, **5**, 2661–2673, doi:10.5194/amt-5-2661-2012.
- , U. Löhnert, P. Kollias, R. C. Jackson, and G. M. McFarquhar, 2015: Developing and evaluating ice cloud parameterizations for forward modeling of radar moments using in situ aircraft observations. *J. Atmos. Oceanic Technol.*, **32**, 880–903, doi:10.1175/JTECH-D-14-00112.1.
- Maschwitz, G., U. Löhnert, S. Crewell, T. Rose, and D. D. Turner, 2013: Investigation of ground-based microwave radiometer calibration techniques at 530 hPa. *Atmos. Meas. Tech.*, **6**, 2641–2658, doi:10.5194/amt-6-2641-2013.
- Mead, J. B., I. PopStefanija, P. Kollias, B. A. Albrecht, and R. Bluth, 2003: Compact airborne solid-state 95 GHz FMCW radar system. *31st Int. Conf. on Radar Meteorology*, Seattle, WA, Amer. Meteor. Soc., 4A.3, <https://ams.confex.com/ams/32BC31R5C/webprogram/Paper63494.html>.
- Pazmany, A. L., R. E. McIntosh, R. D. Kelly, and G. Vali, 1994: A 94-GHz Doppler radar for cloud observations. *IEEE Trans. Geosci. Remote Sens.*, **32**, 731–739, doi:10.1109/36.298002.
- Reimann, J., and M. Hagen, 2016: Antenna pattern measurements of weather radars using the sun and a point source. *J. Atmos. Oceanic Technol.*, **33**, 891–898, doi:10.1175/JTECH-D-15-0185.1.
- Rosenkranz, P. W., 1998: Water vapor microwave continuum absorption: A comparison of measurements and models. *Radio Sci.*, **33**, 919–928, doi:10.1029/98RS01182.
- Skou, N., 1995: A Scanning Microwave Radar and Radiometer. *Conference Proceedings: Second Topical Symposium on Combined Optical-Microwave Earth and Atmosphere Sensing*, IEEE, 215–216, doi:10.1109/COMEAS.1995.472318.
- Sosnytskiy, S. V., 2014: Restoration of aliased average Doppler spectra. *2014 20th International Conference on Microwaves, Radar and Wireless Communications; MIKON-2014*, A. Bikonis and K. Nyka, Eds., IEEE, 4 pp., doi:10.1109/MIKON.2014.6899960.
- Strauch, R. G., 1976: Theory and application of the FM-CW Doppler radar. Ph.D. thesis, University of Colorado Boulder, 24 pp.
- Thies, B., K. Müller, F. Maier, and J. Bendix, 2010: Fog monitoring using a new 94 GHz FMCW cloud radar. *Proc. Fifth Int. Conf. on Fog, Fog Collection and Dew*, Münster, Germany, Copernicus Gesellschaft mbH, FOGDEW2010-103, <http://meetingorganizer.copernicus.org/FOGDEW2010/FOGDEW2010-103.pdf>.
- Tridon, F., and A. Battaglia, 2015: Dual-frequency radar Doppler spectral retrieval of rain drop size distributions and entangled dynamics variables. *J. Geophys. Res. Atmos.*, **120**, 5585–5601, doi:10.1002/2014JD023023.
- Turner, D. D., M. P. Cadeddu, U. Löhnert, S. Crewell, and A. M. Vogelmann, 2009: Modifications to the water vapor continuum in the microwave suggested by ground-based 150-GHz observations. *IEEE Trans. Geosci. Remote Sens.*, **47**, 3326–3337, doi:10.1109/TGRS.2009.2022262.
- Ulaby, F. T., and D. G. Long, Eds., 2014: *Microwave Radar and Radiometric Remote Sensing*. 1st ed. University of Michigan Press, 984 pp.
- van der Dussen, J. J., and Coauthors, 2013: The GASS/EUCLIPSE model intercomparison of the stratocumulus transition as observed during ASTEX: LES results. *J. Adv. Model. Earth Syst.*, **5**, 483–499, doi:10.1002/jame.20033.
- Wang, J., and B. Geerts, 2003: Identifying drizzle within marine stratus with W-band radar reflectivity. *Atmos. Res.*, **69**, 1–27, doi:10.1016/j.atmosres.2003.08.001.
- Yamaguchi, J., and Coauthors, 2009: Evaluation of radar reflectivity (Z) for FMCW millimeter-wave cloud radar “FALCON-I.” *IEEJ Trans. Fundam. Mater.*, **129**, 183–189, doi:10.1541/ieejfms.129.183.

## 4.2 Measurement Uncertainties due to Sequential Chirp Sampling

On the one hand, JOYRAD-94 has optimally matched beams of passive and active radiometric components, which decreases uncertainties in retrievals combining passive radiometry and radar. This is further discussed in [Publication II](#). On other hand, JOYRAD-94 executes several chirp sequences consecutively to account for a limited IF bandwidth that does not allow sampling of the entire vertical column with one chirp sequence. This leads to a delay between the individual chirp sequences. Therefore, different atmospheric layers are sampled at different times, i.e. the sampled vertical profile will be a composite of different scenes, if the physical conditions of the observed volumes changes on time scales smaller than the time difference between the chirps.

Figure 4.1 shows a comparison between JOYRAD-94 and JOYRAD-35 of single-layer ice-clouds that are classified by CLOUDNET (Illingworth et al., 2007). CLOUDNET provides data with 30 s temporal resolution. The maximum  $Z_e$ s that are detected by JOYRAD-35 and JOYRAD-94 within this time frame and their sampling times are compared. The data is separated into three layers in which cloud base heights (CBH) occur. As both instruments agree in terms of  $Z_e$  measurements (see [Publication I](#)), the difference of maximum detected reflectivities ( $\Delta_{max}(Z_e)$ ) is distributed around zero. However, the time difference of when the maximums are sampled increases with height from 0 s below 1200 m to 1 s between 1200 and 3000 m and to 2 s above 3000 m. These differences coincide with the (cumulative) sampling times of JOYRAD-94 at the respective layers, which are given in table 2 in [Publication I](#). This implies that the accuracy of temporally high-resolved (a few seconds resolution) retrievals that focus on the entire vertical column will degrade if the scene changes on time scales smaller than the sampling time of an entire chirp sequence. However, retrieving cloud properties from clouds with a few hundred meters thickness, such as those investigated in [Publication II](#) and [Publication III](#), will be affected much less as long as the cloud is located within only one (chirp) layer. If data of JOYRAD-94 is used in combination with other instruments, e.g. for comprehensive retrieval approaches (e.g. Frisch et al., 1998), the sampling times of the instruments must be corrected accordingly. Hence, data processing of JOYRAD-94 data may be more laborious than for other instruments, e.g. JOYRAD-35, which probe

the entire column simultaneously<sup>1</sup>. The errors that can be expected due to delays in the sampling time will be as high as the variability of the measured property during this delay time.

### 4.3 Dealiasing Radar Doppler Spectra

In addition to the data processing conducted by the RPG-software, the data of JOYRAD-94 undergoes several further quality checks (henceforth *AddProc* for additional processing). The main check is the so-called *dealiasing* that is also discussed in [Publication II](#). In contrast to the *dual radar dealiasing method* introduced in [Publication II](#), *AddProc* does not use  $v_m$  from a co-located radar as initial guess, but uses  $v_m$  from a neighboring range gate that is aliasing-free or has already been dealiasied. *AddProc* starts dealiasing at cloud top, where Doppler velocities are in general small, i.e. close to zero, where no aliasing is expected. If no aliasing is evident, *AddProc* calculates radar moments for the considered range bin and uses the corresponding  $v_m$  as initial guess for the next lower range gate. The final spectrum is determined as described in [Publication II](#).

The assumption of aliasing-free cloud tops is not always valid, especially in very turbulent cloud and fog layers. As a consequence, the initial guess will be wrong, if the spectrum is shifted by a multiple of the twice the Nyquist velocity. Such a wrongly determined guess velocity propagates through the entire cloud layer. This is illustrated in [Fig. 4.2a](#) showing a dealiasied time-height field of  $v_m$  for a one-hour time series in a turbulent cloud. Clearly visible are vertical columns in which  $v_m$  is under- or overestimated by a multiple integer of the  $2v_N$ . *AddProc* identifies such columns by

1. calculating the difference between two consecutive bins in time;
2. calculating the mean difference for each vertical column;
3. taking the absolute value of point 2;
4. treating the absolute values as a signal and determining the peak noise level using Hildebrand and Sekhon (1974);
5. and finally identifying all values larger than the peak noise determined in (4).

---

<sup>1</sup>Actually, no active instrument can probe the entire column simultaneously - the signal from the first range gate will always return earlier than from any other range gate. However, the delay is usually so short (microseconds) that steady state can be assumed for the observed scene.

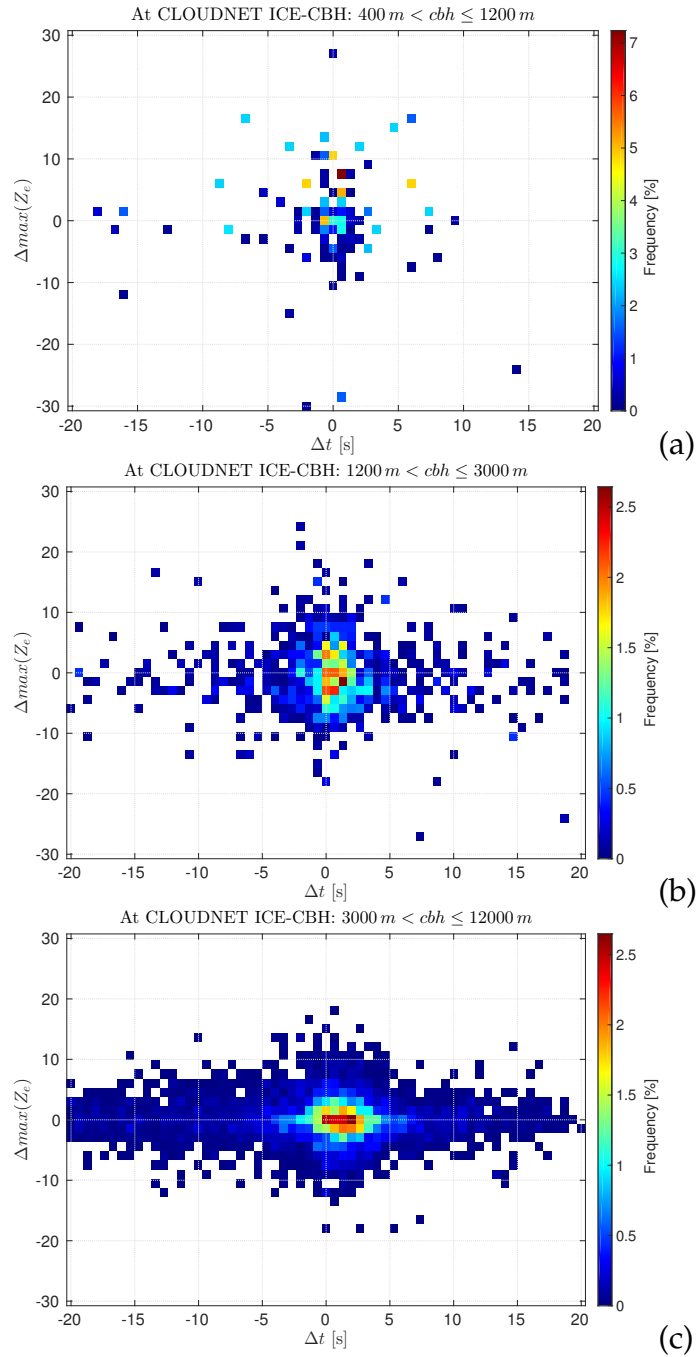


FIGURE 4.1: Occurrence frequency of the difference between the maximum reflectivities of JOYRAD-35 and JOYRAD-94 ( $\Delta max(Z_e) = max(Z_e^{35}) - max(Z_e^{94})$ ) that were observed during a time window of 30 seconds versus the time difference  $\Delta t$  when the two instruments detected the maximum. Only single-layer ice-clouds are considered. (a) For cloud base heights (CBH) between 400 and 1200 m. (b) For CBH between 1200 and 3000 m. (c) For CBH between 3000 and 12000 m. Note that the color scale is different in (a).

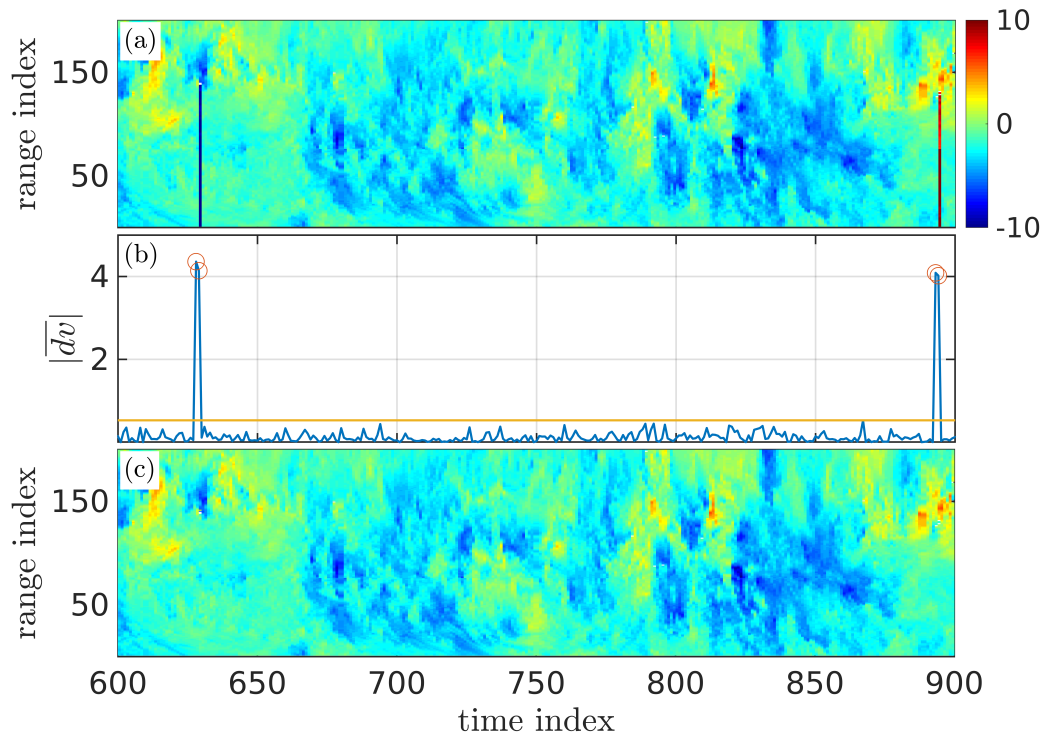


FIGURE 4.2: (a) Results of the dealiasing procedure of AddProc. Wrongly dealiased columns are visible at time indexes 630 and 894. (b) Absolute mean values of  $v_m$  (m s<sup>-1</sup>) differences of two timely adjacent bins ( $|\overline{dv}|$  (m s<sup>-1</sup>): blue). The peak noise level (yellow) of this signal was determined using Hildebrand and Sekhon, 1974. All values above the peak noise (red circles) are identified and corrected by AddProc. (c) Corrected velocity field of (a).

Figure 4.2b illustrates the procedure plotting the absolute column-means of  $v_m$  differences ( $|\overline{dv}|$ ). AddProc also takes into account that several consecutive columns can be dealiased wrongly. All values above the peak noise are corrected by shifting  $v_m$  by a multiple integer of  $2v_N$  depending on how much the individual values deviate from the correctly dealiased column. The result is given in Fig. 4.2c showing that the  $v_m$  field can be reconstructed in case of wrongly dealiased columns. However, in case of missing neighboring columns the quality check might fail.



## Chapter 5

# Retrieving Liquid Water Content of Warm Stratified Clouds

### 5.1 Publication II

N. Küchler and U. Löhnert (2018). “Radar-radiometer based liquid water content retrievals of warm low-level clouds: how the measurement setup affects retrieval uncertainties”. In: *IEEE Journal of Selected Topics in Applied Earth Observations and Remote Sensing* under review

# Radar-radiometer based liquid water content retrievals of warm low-level clouds: how the measurement setup affects retrieval uncertainties

Nils Kuchler and Ulrich Löhnert

**Abstract**—Here, we propose a new methodology that increases the understanding of uncertainty sources of liquid water content retrievals, which are caused by the combination of instruments having different beam widths and are horizontally displaced. Further, we give first quantitative uncertainty estimates. The work is based on a case study of a single-layer, warm, stratiform cloud observed at the Jülich Observatory for Cloud Evolution. The liquid water content profiles of this cloud have been forward-simulated with the Passive and Active Radiative Transfer Model providing radar and microwave radiometer observables for all cloud columns. These observables have been converted back into liquid water content profiles, whereas in this case the microwave radiometer and radar observables from different columns were combined, representing horizontal displacement. We investigate the influence of horizontal distance between a radar and a microwave radiometer on a commonly used retrieval for liquid water content, which scales radar reflectivity profiles with the liquid water path given by the microwave radiometer. We found that a displacement of only 10 m already introduces an additional relative uncertainty of 10 %. At 100 m displacement the relative error grows up to 30 %. Also different beam widths decrease the retrieval accuracy by a few percent; however, at large displacements, radiometers with larger beam widths slightly decrease the error due to the displacement. Finally, we show that cloud edge studies require optimally matched beams between the radar and the radiometer, and already a displacement of 10 m leads to unreasonable results.

**Index Terms**—Ground-based remote sensing, liquid water content retrievals, uncertainty, sensor synergy, microwave radiometer, radar

## I. INTRODUCTION

LOW level clouds, such as stratus and stratocumulus, cover a large area of the planet and thereby strongly influence the Earth’s radiation budget [1]. In general, clouds are a major uncertainty source in numerical weather and climate prediction models [2] and therefore clouds must be correctly characterized by observations to enable accurate model validation. Furthermore, advancing model resolutions in space and time [3] increase the demand for highly-resolved retrievals of cloud properties, such as liquid water content (LWC) with well quantified uncertainty estimates.

Long-term observations of LWC with temporal and spatial resolutions of a few seconds and meters, respectively, can be recorded using ground-based remote sensing. A common approach to retrieve LWC is to combine radar with microwave radiometer (MWR) measurements by scaling the vertical reflectivity profile ( $Z_e$ ) derived from a radar with the column liquid water path (LWP) derived from a MWR [4], [5]. Both instruments are standard equipment at measurement sites

observing cloud processes and properties [6]–[9] and are used mostly by the community to retrieve LWC profiles [10].

Retrievals are always associated with uncertainties that can be instrument specific, such as calibration bias, instrument noise and finite bandwidths [11], [12]; can be caused by inherent retrieval assumptions and algorithm uncertainties [5], [13]; and by combining two instruments, which may lead to mismatching sampling volumes [14]. The latter is often assumed to be of minor importance, especially, when temporal averaging to several seconds or minutes is applied. However, when conducting high frequency sampling (e.g. 1 Hz), different half power beamwidths (HPBW) and horizontal distance between two sensors (henceforth “sensor displacement  $\Delta X$ ”) can affect the retrieval accuracy.

Current state-of-the-art cloud radars have HPBWs varying between  $0.2^\circ$  and  $0.58^\circ$  [15]–[17], whereas state-of-the-art MWRs, retrieving LWP, span a range from  $0.58^\circ$  to  $6^\circ$  HPBW [17]–[19]. Information on  $\Delta X$  is often not discussed or not given at all in literature describing comprehensive observatories and campaigns [8], [20], although it can range from about 10 m [21] up to about 100 m [22], and which has significant influence on the retrieval accuracy.

When combining a radar and a radiometer, being displaced by 100 m and both vertically pointing, and having a HPBW of  $0.5^\circ$ , the observed volumes of the two instruments will intersect at 5.7 km the first time. Thus, if low-level clouds are present, also the sampling volumes will be horizontally displaced, i.e. the two sensors will observe different scenes, e.g. at 1.5 km height the volumes are displaced by 75 m. That radar and radiometer observe different scenes can also happen in case of overlapping beams, namely, if the sensors have very different HPBWs. A radar-radiometer combination having HPBWs of  $0.2^\circ$  and  $6^\circ$ , respectively, with  $\Delta X = 0$  m has overlapping beams; however, the footprint of the radiometer is 1000 times larger than the footprint of the radar at any height. Hence, any variability in the observed column will be less pronounced in the radiometer signal than in the column integrated radar signal.

Figure 1 illustrates the effect of  $\Delta X$  on a retrieval at the maximum of an LWC profile ( $LWC_{max}$ ) when combining a radar and a MWR having both a HPBW of  $0.6^\circ$ . The time series exhibits how much  $LWC_{max}$  differs from a reference  $LWC_{max}$ , i.e. at  $\Delta X = 0$  m, for different sensor displacements. Deviations above  $0.4 \text{ g m}^{-3}$  (about 300 % relative error) are visible, being on average larger for a larger  $\Delta X$ . Such under- or overestimations can lead to strong under-



or overestimations of cloud top radiative cooling of several Kelvin per hour [23].

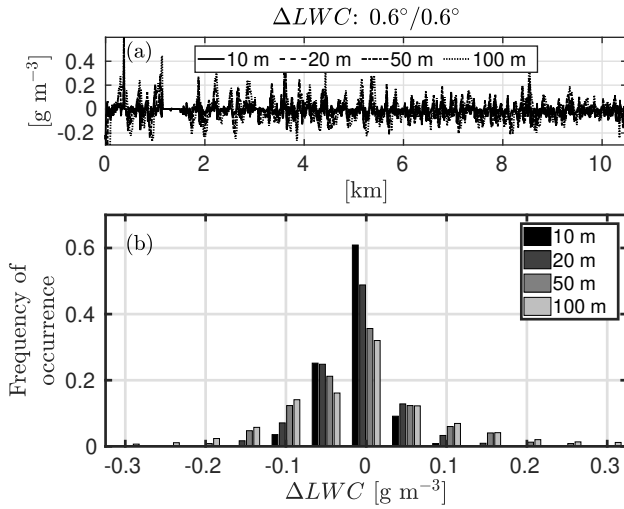


Fig. 1. Error of liquid water content retrieval ( $\Delta LWC$ ) combining radar and microwave radiometer measurements after [13] that was applied to the reference cloud in Fig. 2a. The error is caused by displacing (here 10, 20, 50, 100 m) radar and microwave radiometer from each other, both having a HPBW of  $0.6^\circ$ . (a) Error at maximum of the LWC profile in the cloud. (b) Frequency of occurrence of  $\Delta LWC$  shown in (a) depending on different displacements.

In the following, we will discuss the effects of  $\Delta X$  and differences in the HPBWs on LWC retrievals of warm low-level stratiform clouds, which combine radar and radiometer measurements. Thereby, it is assumed that the LWC can be correctly derived after [13] given that both instruments observe the identical field of view. We further investigate how these differences influence the retrieval at cloud edges and when broken cloud fields are present.

## II. METHODOLOGY

The following analysis is based on the LWC retrieval by [13] combining MWR and radar measurements. Thereby, the square root of  $Z_e$  is scaled with the LWP providing an LWC estimate for the  $i$ -th layer after

$$LWC_i = LWP \frac{\sqrt{Z_i}}{\sum_{j=1}^M \Delta h_j \sqrt{Z_j}}. \quad (1)$$

Each of the  $M$  layers is associated with a reflectivity  $Z_i$  and a vertical resolution  $\Delta h_i$ . Equation (1) can be applied as long as the cloud droplet number concentration is constant within the cloud and the third moment of the drop size distribution (DSD) is linearly related to the sixth moment of the DSD. Both assumptions were found to be valid in warm, non-drizzling stratus clouds [13].

Assuming that (1) holds, a reference cloud (henceforth ‘‘RefCloud’’), containing only cloud droplets, was created by converting a one-hour time series of  $Z_e$  and LWP into a two dimensional, spatial field of LWC (Fig. 2a). The  $Z_e$  and LWP time series have been recorded at the Jülich Observatory for Cloud Evolution - Core Facility (JOYCE-CF) [8] with a W-band radar-radiometer measuring with temporal and vertical

resolutions of about 3 s and about 20 m [17], respectively. At JOYCE-CF the so-called CLOUDNET classification product [7] is available, which classified the cloud as containing cloud droplets only.

While the data of the W-band radar-radiometer has been recorded every three seconds, the actual sampling time was 1 s. Cloud base was located at about 800 m within this hour exhibiting a wind speed of about  $10 \text{ m s}^{-1}$ . The footprint of the radar has a diameter of about 6 m at 800 m. Based on these values, we assumed that the radar averaged over approximately 10 m horizontal cloud extent, hence, one data point in time corresponds to about 10 m horizontal extent in Fig. 2a.

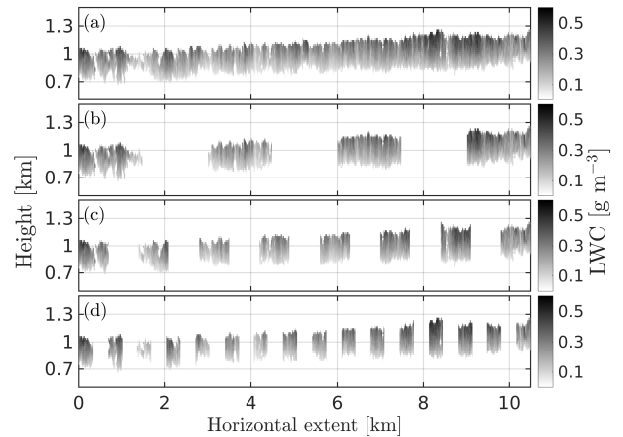


Fig. 2. (a) Reference cloud (RefCloud) that has been created applying reflectivity and liquid water path measurements to (1). The measurements were recorded by a W-band radar-radiometer at the Jülich Observatory for Cloud Evolution - Central Facility in Jülich, Germany. (b) Slices of RefCloud of (a) to mimic a broken cloud field. (c) Like in (b), but two times more and smaller slices. (d) Like in (c), but two times more and smaller slices.

Considering RefCloud as physical truth, observables such as  $Z_e$  and brightness temperatures (BT) can be forward simulated for any radar-MWR combination exhibiting different HPBW, frequencies and  $\Delta X$  when applying some further assumptions that will be introduced later in this section. After determining LWP combining the forward simulated BTs at several frequencies [24], LWC profiles can be determined again following (1).

Figure 3 illustrates the geometrical concept of our study: due to finite beam widths, the sensors receive signal from cloud regions not directly located in the vertical field of view of the sensor, which is typically the scene of interest. The larger the HPBW, the more regions out of interest contribute to the measured signal. Forward simulations were performed at 31 angles equally spaced (in radian) between  $-3.1^\circ$  and  $+3.1^\circ$  along slanted paths providing 31 BTs and  $Z_e$  profiles. Final (averaged)  $Z_e$  profiles and BTs were calculated for different HPBWs, i.e. averaging a different number of slanted path simulations while assuming a perfect Gaussian antenna pattern to weight contributions differently from different directions. Note that we neglected any effects due to antenna side lobes. Moreover, the radar HPBW used here corresponds to the gain-squared pattern, i.e. the pattern resulting from a two-way propagation of radiation through the antenna, which is not the case for the radiometer where the radiation passes only

once the antenna. Usually, radar HPBW are given in one-way HPBW. Comparing a one-way radar HPBW with a radiometer HPBW of the same value would lead to different fields of view because the actual radar HPBW, i.e. the gain-squared pattern, has a finer resolution than the one-way HPBW.

Instrument displacement was imitated by combining  $Z_e$  profiles and BTs from different horizontal positions ( $X$ ). The instruments were displaced in steps of 10 m varying from 0 to 100 m. Thereby, the radar beam was shifted towards larger values of  $X$  with respect to the MWR, i.e.  $X_{radar} > X_{MWR}$ , and the column above the radar was considered as truth ( $lwc_{true}$ ). Hence, the LWC profile for a displaced combination ( $lwc_{displaced}$ ) was calculated with the LWP derived at a horizontal distance of  $X_{MWR} = X_{radar} - \Delta X$  compared to the radar location.

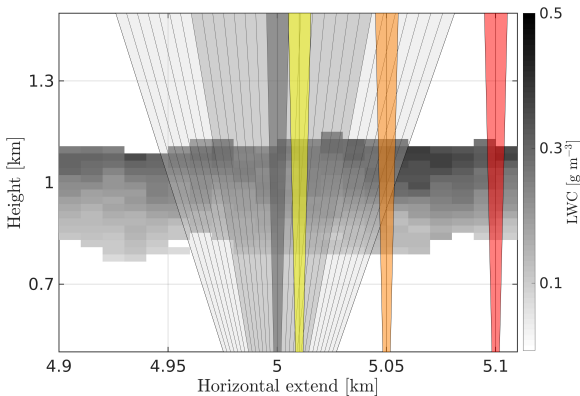


Fig. 3. Reference cloud with liquid water content (LWC). Fields of view from ground-based remote sensing instruments, here radar and radiometer, are shown in gray, red, orange and yellow. Gray areas represent half power beam widths (HPBW) of  $6.2^\circ$ ,  $3.5^\circ$  and  $0.6^\circ$ . Yellow, orange and red have a HPBW of  $0.6^\circ$ , too. Instruments with gray areas are located at the ground at 5 km horizontal extent. Yellow, orange and red represent the field of view of a radar that is displaced by 10 m, 20 m, and 50 m, respectively. Hence, a radar being displaced by 50 m observes a different scene than a radiometer with one of the gray fields of view. The solid lines within the beams indicate paths along which radar reflectivities and brightness temperatures were forward simulated using the Passive and Active Radiative Transfer Model [25]. Simulations were performed at all horizontal grid points, being spaced by 10 m. In addition to the LWC, a log-normal drop size distribution and an effective radius increasing from 5 to 9  $\mu\text{m}$  from cloud base to cloud top were assumed. Finally, these observables can be converted back into LWC profiles using (1) while assuming different displacements between radar (reflectivity) and microwave radiometer (brightness temperatures). The derived LWC profile can be then compared to the profiles of the reference cloud.

BTs and  $Z_e$  of RefCloud were forward simulated with the Passive and Active Microwave Radiative Transfer Model [25] for ground-based, zenith pointing instruments at several frequencies between 21 and 35 GHz. The radar frequency and the radar Doppler spectrum noise floor at 1 km radial distance were set to 35 GHz and -38 dBZ, respectively. We assumed a log-normal-DSD with a width of 0.38 having a random uncertainty of  $\pm 0.14$  [26] and an effective radius that linearly increases from 5  $\mu\text{m}$  at cloud base to 9  $\mu\text{m}$  at cloud top [14]. Note that RefCloud was constructed using data from a W-band radar without considering any attenuation effects. This might have indeed lead to an (over-) underestimation of LWC at cloud (base) top when constructing RefCloud with respect

to the actual cloud structure. However, constructing RefCloud using W-band radar data does not affect the following analysis, because  $Z_e$  profiles were simulated at 35 GHz where attenuation is negligible for an average LWP of RefCloud of about  $50 \text{ g m}^{-2}$ .

Based on the averaged BTs, LWP was retrieved using seven frequencies between 21 and 31 GHz, which are commonly used to derive LWP [27]. The retrieval is a quadratic model [17] and was developed with a training data set of 15175 radiosondes, in which the presence of a modified adiabatic cloud was assumed when the relative humidity exceeded 95 % [27]. A random uncertainty of  $\pm 1 \text{ K}$  was added to BTs before determining the retrieval coefficients. The uncertainty in the retrieval is characterized by a root-mean-square error (RMSE) of  $25 \text{ g m}^{-2}$ .

We used frequencies between 21 and 35 GHz to represent most accurate state-of-the-art retrievals of LWP and to minimize attenuation effects in the radar measurements. To investigate also how cloud patchiness influences the retrieval accuracy of two displaced instruments, RefCloud was sliced into broken cloud fields with different degrees of patchiness (Fig. 2b, c, d) before the forward simulations were performed.

### III. RESULTS

Based on the methodology explained in section II, we derived median profiles of the relative error of LWC

$$\Delta lwc_{rel} = \frac{lwc_{true} - lwc_{displaced}}{lwc_{true}}, \quad (2)$$

which will be used in the following to quantify the retrieval uncertainty depending on different measurement setups.

#### A. Sensor displacement and varying HPBWs

Figures 4a, c, e show the median of  $\Delta lwc_{rel}$

$$Md(\Delta lwc_{rel}) = \text{median}(\Delta lwc_{rel}) \quad (3)$$

for 10, 20 and 50 m displacement depending on the in-cloud position  $h^*$  ( $h^* = 0$  corresponds to cloud base and  $h^* = 1$  to cloud top) and four different combinations of MWR and radar HPBWs:  $0.6^\circ/0.6^\circ$  (MWR HPBW/ radar HPBW),  $1.5^\circ/0.6^\circ$ ,  $3.6^\circ/0.6^\circ$  and  $6^\circ/0.6^\circ$ . We do not show different radar HPBWs, since varying the HPBW between  $0.6^\circ$  and  $1^\circ$  has no significant effect on the retrieval performance.

The profile of  $Md(\Delta lwc_{rel})$  is approximately constant for  $h^*$  values between 0.2 and 0.8. This is what is expected, since any offset in  $Z_e$  cancels out in (1) [13], thus, the remaining uncertainty from the LWP measurement ( $\Delta LWP$ ) leads to a constant relative error when normalizing with the LWC profile. The influence of the random uncertainty of  $Z_e$  is small compared to the effect of  $\Delta LWP$  and vanishes when considering statistical averages as done in Fig. 4a, c, e. At cloud center,  $Md(\Delta lwc_{rel})$  is larger for larger MWR HPBW and increases with  $\Delta X$ . On average,  $Md(\Delta lwc_{rel})$  increases from about 3 % at  $\Delta X = 10 \text{ m}$  to 5 % at  $\Delta X = 50 \text{ m}$ .

Close to cloud base and cloud top,  $Md(\Delta lwc_{rel})$  increases strongly exhibiting values of up to 12 %. This is due to varying cloud base and cloud top from column to column (data point  $X$

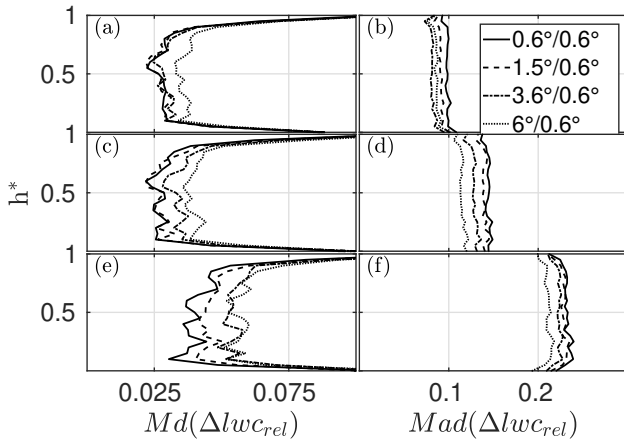


Fig. 4. Left column: Median relative error of liquid water content ( $Md(\Delta lwc_{rel})$ ) depending on position within the cloud  $h^*$  ( $h^* = 0$  ( $= 1$ ) corresponds to cloud base (top)) and different combinations of radiometer/radar half power beam widths. (a) 10 m displacement between radar and microwave radiometer. (c) 20 m displacement. (e) 50 m displacement. Right column: Same as left column but showing median absolute deviation of  $\Delta lwc_{rel}$  ( $Mad(\Delta lwc_{rel})$ ). (b), (d), (f) for 10 m, 20 m and 50 m displacement.

to data point  $X + \Delta X$ ). In the setup investigated here, a radar with a HPBW of  $0.6^\circ$  receives signals also from neighboring columns. Therefore, a higher (lower) cloud base (top) in the neighboring columns, i.e. volumes without signal, can lead to a strong underestimation of  $Z_e$  at cloud base (top) producing a large  $Md(\Delta lwc_{rel})$ .

The effect of different HPBWs has a magnitude similar to sensor displacement.  $Md(\Delta lwc_{rel})$  is about 2-3 % smaller when combining  $0.6^\circ/0.6^\circ$  than the combination of  $6^\circ/0.6^\circ$ . Henceforth, we refer to the HPBW combinations  $0.6^\circ/0.6^\circ$  and  $6^\circ/0.6^\circ$  as BC-NN (beam combination - narrow narrow) and BC-WN (beam combination - wide narrow), respectively.

When observing processes with a high temporal resolution, the median absolute deviation

$$Mad(\Delta lwc_{rel}) = \text{median}(|\Delta lwc_{rel} - Md(\Delta lwc_{rel})|), \quad (4)$$

which is similar to the root-mean-squared error, is a more reasonable choice as uncertainty estimate than  $Md(\Delta lwc_{rel})$ .  $Mad(\Delta lwc_{rel})$  is about 10 % at  $\Delta X = 10$  m and increases to about 20 % at  $\Delta X = 50$  m (Fig. 4b, d, f). In contrast to  $Md(\Delta lwc_{rel})$ ,  $Mad(\Delta lwc_{rel})$  is larger for BC-NN than for BC-WN, which is due to smoothing effects at larger MWR HPBWs. This will be further discussed in the following paragraph.

Figure 5 shows  $Mad(\Delta lwc_{rel})$  depending on  $\Delta X$  for BC-NN and BC-WN at the cloud's center. Since  $Mad(\Delta lwc_{rel})$  is approximately constant with height (Fig. 4b, d, f), the curve in Fig. 5 is representative for any cloud level not too close to cloud top or cloud base. For both combinations,  $Mad(\Delta lwc_{rel})$  increases from about 5 % at zero displacement to about 30 % at  $\Delta X = 100$  m. At  $\Delta X = 0$  m, BC-NN shows a much smaller uncertainty than BC-WN, which is due to the much wider MWR beam of BC-WN averaging over several data columns and thereby smoothing the LWP signal. However, the wider beam is beneficial once radar and MWR

are displaced from each other and the LWP varies on length scales of the displacement. Thus, the LWP retrieved from a MWR with a large HPBW will be on average closer to the LWP of the scene of interest than an LWP retrieved with a small HPBW. This can be seen in Fig. 5 where BC-NN has a greater  $Mad(\Delta lwc_{rel})$  than BC-WN for any  $\Delta X$  larger than zero.

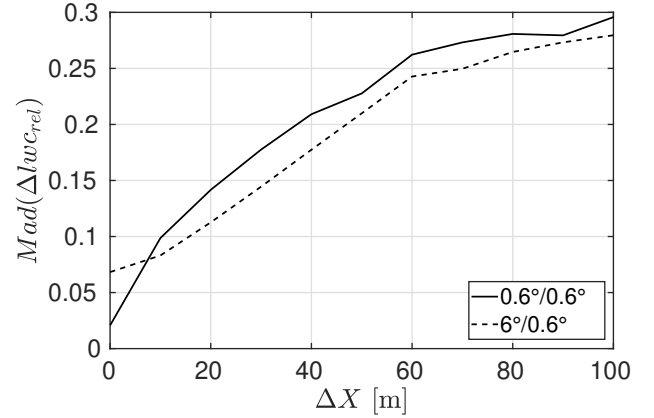


Fig. 5. Median absolute deviation of relative liquid water content error ( $Mad(\Delta lwc_{rel})$ ) at cloud center depending on sensor displacement  $\Delta X$  and different HPBW combinations (radiometer/radar).

A different way to assess the uncertainty of the retrieval following (1) is to investigate the correlation between the LWP and the sum of  $\sqrt{Z_e}$  ( $\sum \sqrt{Z_e}$ ) within the observed column. Both parameters are linearly related based on (1). Figure 6a shows the correlation between  $\sum \sqrt{Z_e}$  and LWP depending on  $\Delta X$  and the HPBW combinations. It is evident that the correlation decreases with increasing  $\Delta X$  which confirms the findings that  $Mad(\Delta lwc_{rel})$  increases with  $\Delta X$ . For any HPBW combination, the correlation drops from about 0.85 to 0.58, which implies that displacing instruments decreases the validity of (1). Also here, we see the same effect as in Fig. 5: a larger MWR HPBW shows lower uncertainty once  $\Delta X > 0$  m.

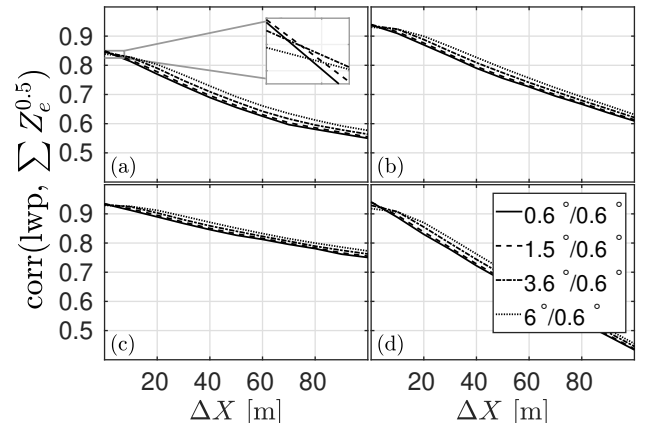


Fig. 6. Linear correlation coefficients ( $\text{corr}(\cdot, \cdot)$ ) between the liquid water path (LWP) and cumulative square root of reflectivity ( $\sum Z_e^{0.5}$ ) depending on sensor displacement  $\Delta X$  and different combinations of HPBW (radiometer/radar). (a, b, c, d)  $Z_e$  and LWP were determined from reference clouds in Fig. 2a, b, c, d.

### B. Cloud variability and cloud edges

To investigate the effect of cloud variability in terms of patchiness, we sliced RefCloud into three cloud fields with different degrees of variability (Fig. 2b, c, d). Also for these cloud fields, we determined the correlation between  $\sum \sqrt{Z_e}$  and LWP depending on  $\Delta X$  (Fig. 6b, c, d). When comparing Fig. 6b, c, d to Fig. 6a, one can see that the correlation at zero displacement is always larger in broken cloud fields, which is due to the clear sky periods where both  $\sum \sqrt{Z_e}$  and LWP are approximately zero. However, the correlation coefficients at  $\Delta X = 100$  m are larger in Fig. 2b/6b (0.62), much larger in Fig. 2c/6c (about 0.77), but smaller in Fig. 2d/6d (0.45). The effect of larger correlation at larger  $\Delta X$  in Fig. 2b/6b and Fig. 2c/6c does not reflect a decrease of retrieval uncertainty, rather an optimal matching between the window size of clear sky regions and  $\Delta X$ . Hence, Fig. 2b/6b and Fig. 2c/6c do not provide usable information. But, the strong decrease of the correlation in Fig. 2d/6d compared to Fig. 2a/6a tells the following: on the one hand, the retrieval by [13] is not applicable once the cloud field varies on length scales similar to  $\Delta X$  but on the other hand, as long as  $\Delta X$  is small, LWC can be retrieved also for very patchy cloud fields. Also here, beam width effects are small compared to sensor displacement.

As scattering of sunlight is very complex in broken cloud fields, it is important to accurately determine the microphysics at cloud edges. To gain a first estimate of how accurate cloud edges can be described in terms of LWC by (1), we determined  $\Delta lwc_{rel}$  at the left cloud edges ( $N = 16$ ) in Fig. 2d. Thereby, the radar position was fixed at the first cloudy column of each cloud edge and the radiometer was shifted towards lower values of  $X$ , i.e.  $X_{radar} \geq X_{MWR}$ . Since the LWC of the radar column was used to normalize the error (see (2)), we considered only left cloud edges to obtain non-infinite error estimates. Hence, the maximum possible value of  $\Delta lwc_{rel}$  is 1 (100 %). Figure 7 illustrates the median of  $\Delta lwc_{rel}$  ( $Md(\Delta lwc_{rel})$ ) depending on the HPBW of the MWR and  $\Delta X$  at cloud center, i.e. at  $h^* = 0.5$ .  $\Delta lwc_{rel}$  is 100 % once the MWR does not provide an estimate for LWP, hence, no LWC can be retrieved although the radar observes the cloud edge. One can see that almost for any combination of HPBW and  $\Delta X > 0$ , the retrieval does not provide any information. Only the MWR-HPBW of  $3.6^\circ$  and  $6^\circ$  provide information on LWP at  $\Delta X = 10$  m. Yet,  $Md(\Delta lwc_{rel})$  is larger than 70 % implying that in these cases the beam of the MWR is only partially filled by the cloud.

## IV. CONCLUSION

Our analysis provides relative uncertainty estimates of LWC after [13] for varying distances between radar and microwave radiometer and HPBWs of both, as well as the impact in overcast vs. broken cloudy scenes. A comprehensive analysis of all influencing variables was beyond the scope of this article, but it proposes a new methodology to investigate those uncertainties that have not been discussed in the literature to date.

The following limitations of this study show how difficult it is to assess the uncertainty that arises from the measurement

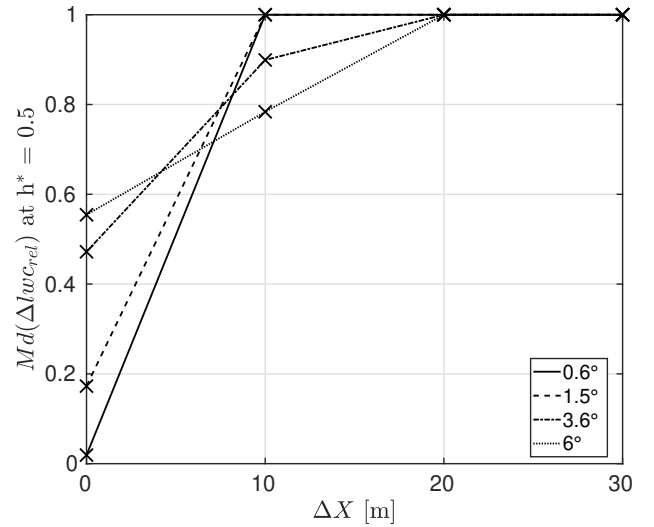


Fig. 7. Median relative error of liquid water content  $Md(\Delta lwc_{rel})$  at cloud edges from Fig. 2d depending on sensor displacement  $\Delta X$ . The error curve is determined at cloud center, i.e. at  $h^* = 0.5$ .  $Md(\Delta lwc_{rel}) = 1$  indicates that no LWC profile could be derived due to sensor displacement. The radar was located under the first cloudy column at the lateral cloud edge and the radiometer was shifted towards cloud free columns.

setup: the study is based on one case study that was associated with certain boundary conditions, e.g. a certain cloud base height that varied between 800-900 m. The yearly average cloud base height of low-level, single layer, liquid clouds at JOYCE-CF is about 1.2 km [17]. Increasing the cloud base height had the following effects: the uncertainty due to sensor displacement would decrease because of better beam overlap at larger altitudes. How the uncertainty changes due to different HPBW in this case depends on the ratio between the horizontal scale of cloud variability and the footprint of the instruments within the cloud. Additional parameters that can affect our analysis are the assumptions on DSD and effective radii, both influencing  $Z_e$ . Furthermore, we present uncertainty estimates in relative units. However, knowing the absolute uncertainty is important when calculating physical quantities that are not linearly related to LWC.

The case scenario shown here is an idealized case because both instruments observe always the same scene, yet, with a spatial shift (time delay in observations). Moreover, steady-state was assumed. Both aspects are very special cases, hence, cannot be generalized. It is likely that the uncertainties will be larger in a non-idealized case than the one presented here. One of the new findings of this study is that increasing the HPBW of the MWR increases the uncertainty of the retrieval by 3-5 %, as long as both sensors are located at the same position. If the instruments are displaced from each other, a wider MWR beam will be beneficial to sustain at least partial beam overlap, yet, the effect of displacement will contribute most to the retrieval error leading to uncertainties up to 30 % at 100 m displacement.

To put the results of this study into the context of state-of-the-art instrumentation, we discuss our results in the following with respect to currently available technology while neglecting uncertainties of the LWC retrieval after [13]. The latter will be

discussed at the end of this section. Combining a MWR, measuring between 20 and 31 GHz (K-band), with a co-located radar, measuring around 30 GHz, is a common approach to derive LWC profiles [8]. In the best case, both instruments are located within a few meters distance up to 10 m, which would lead to 10 % relative uncertainty. In addition to that, a further uncertainty of about 40 % due to the LWP retrieval must be considered, when assuming an uncertainty of 20 g m<sup>-2</sup> [27] and an average LWP of 50 g m<sup>-2</sup> (as given in the used case study). The latter was found to occur in various climate regimes [28]. The retrieval uncertainty of 20 g m<sup>-2</sup> refers to a bias-free LWP retrieval that includes a thorough offset correction [29].

To our knowledge, the W-band radar used here to construct the reference cloud case is the only instrument combining radar and MWR measurements using the same antenna. Thus, the retrieval uncertainty is determined by the accuracy of the LWP retrieval and the radar noise (neglecting LWC retrieval uncertainties). For the LWP retrieval combining BT at 89 GHz and an a priori determined integrated water vapor (IWV), an uncertainty of 15 g m<sup>-2</sup> was found by [17], when a thorough bias correction is applied. In this study, radar reflectivities were simulated only at 35 GHz for simplicity, so that attenuation effects could be neglected. However, at 94 GHz attenuation must be taken into account as further uncertainty source, which depends on LWC, IWV and cloud thickness. A back-of-the-envelope calculation yielded that the relative error of LWC varies between 0 and 15 % for LWP values between 25 and 250 g m<sup>-2</sup>, a cloud thickness of 300 m and an IWV of 10 kg m<sup>-2</sup>. Hence, a retrieval uncertainty between 30 and 45 %, depending on attenuation (corrections), is expected when using a W-band radar-radiometer with matched beams. Due to the uncertainties associated with attenuation effects, we cannot make a general statement about which of the two measurement setups, i.e. W-band radar-radiometer or MWR at K-band frequencies plus a co-located radar, is the better choice to retrieve LWC in stratified clouds. Yet, the results indicate that matched beams have the potential to decrease the retrieval uncertainty by 10 % and more compared to a two-instrument setup, depending on the distance between radar and MWR.

Note that the uncertainties found here are only based on the instrument setup; however, do not include any biases in the retrieval assumptions themselves such as that the third moment of the DSD must be linearly related to the sixth moment of the DSD and that the droplet number concentration must be constant with height [30]. This becomes even more important for retrievals that require more information than radar reflectivity profiles and brightness temperatures. For instance, it was shown by [31] that it is key to characterize a priori information correctly to ensure reliable retrieval results of LWC when using probabilistic approaches. The need for accurate a priori estimates leads back to the investigations presented here: we need to quantify the uncertainties of our measurement setups to be able to collect reliable data sets that can serve as a priori estimates.

Finally, we show that cloud edge studies require closely matched beams in case of sharp cloud edges. Already at a

displacement of 10 m, LWC profiles were associated with uncertainties larger than 75 % or couldn't be derived at all due to missing LWP estimates. How much this uncertainty is at smoother cloud edges will be part of future work. Future studies should also investigate the influence of vertical resolution on the retrieval accuracy, especially, in less homogeneous cloud conditions.

#### ACKNOWLEDGMENT

This work was funded by the project Energy Transitions and Climate Change (<http://et-cc.uni-koeln.de/project.html>) of the Excellence Initiative of the University of Cologne by the German Research Foundation (DFG) under Grant ZUK 81/1. Observations used in this study originate from DFG funded Core Facility (JOYCE-CF) under DFG research grant LO 901/7-1. The observational data used in this study is available at the Institute for Geophysics and Meteorology of the University of Cologne. Thanks to EMK for mental support.

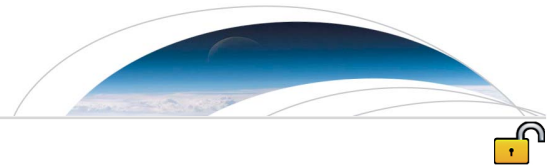
#### REFERENCES

- [1] W. B. Rossow and R. A. Schiffer, "Advances in Understanding Clouds from ISCCP," *B. Am. Meteorol. Soc.*, vol. 80, no. 11, pp. 2261–2287, 1999.
- [2] O. Boucher, D. Randall, P. Artaxo, C. Bretherton, G. Feingold, P. Forster, V.-M. Kerminen, Y. Kondo, H. Liao, U. Lohmann, P. Rasch, S. K. Satheesh, S. Sherwood, B. Stevens, and X. Y. Zhang, "7. Clouds and Aerosols," *Climate Change 2013: The Physical Science Basis. Contribution of Working Group I to the Fifth Assessment Report of the Intergovernmental Panel on Climate Change*, pp. 571–657, 2013.
- [3] R. A. J. Neggers, T. Heus, and A. P. Siebesma, "Overlap statistics of cumulus boundary-layer cloud fields in large-eddy simulations," *J. Geophys. Res. Atmos.*, vol. 116, no. 21, pp. 1–10, 2011.
- [4] A. S. Frisch, C. W. Fairall, and J. B. Snider, "Measurement of Stratus Cloud and Drizzle Parameters in ASTEX with a Ka-Band Doppler Radar and a Microwave Radiometer," *J. Atmos. Sci.*, vol. 52, no. 16, pp. 2788–2799, 1995.
- [5] U. Löhnert, S. Crewel, C. Simmer, and A. Macke, "Profiling cloud liquid water by combining active and passive microwave measurements with cloud model statistics," *J. Atmos. Ocean. Tech.*, vol. 18, no. 8, pp. 1354–1366, 2001.
- [6] T. P. Ackerman and G. M. Stokes, "The Atmospheric Radiation Measurement Program," *Phys. Today*, vol. 56, no. 1, p. 38, 2003. [Online]. Available: <http://link.aip.org/link/PHTOAD/v56/i1/p38/s1&Agg=doi>
- [7] A. J. Illingworth, R. J. Hogan, E. J. O'Connor, D. Bouniol, M. E. Brooks, J. Delanoë, D. P. Donovan, J. D. Eastment, N. Gaussiat, J. W. F. Goddard, M. Haefelin, H. Klein Baltinik, O. a. Krasnov, J. Pelon, J. M. Piriou, a. Protat, H. W. J. Russchenberg, a. Seifert, a. M. Tompkins, G. J. van Zadelhoff, F. Vinit, U. Willen, D. R. Wilson, and C. L. Wrench, "Cloudnet: Continuous evaluation of cloud profiles in seven operational models using ground-based observations," *B. Am. Meteorol. Soc.*, vol. 88, no. 6, pp. 883–898, 2007.
- [8] U. Löhnert, J. H. Schween, C. Acquistapace, K. Ebell, M. Maahn, M. Barrera-Verdejo, a. Hirsikko, B. Bohn, a. Knaps, E. O'Connor, C. Simmer, a. Wahner, and S. Crewel, "JOYCE: Jülich Observatory for Cloud Evolution," *B. Am. Meteorol. Soc.*, vol. 96, no. 7, pp. 1157–1174, 2015. [Online]. Available: <http://journals.ametsoc.org/doi/abs/10.1175/BAMS-D-14-00105.1>
- [9] B. Stevens, D. Farrell, L. Hirsch, F. Jansen, L. Nuijens, I. Serikov, B. Brüggemann, M. Forde, H. Linne, K. Lonitz, and J. M. Prospero, "The Barbados Cloud Observatory – Anchoring Investigations of Clouds and Circulation on the Edge of the ITCZ," *B. Am. Meteorol. Soc.*, 2015. [Online]. Available: <http://journals.ametsoc.org/doi/abs/10.1175/BAMS-D-14-00247.1>
- [10] C. Zhao, S. Xie, S. A. Klein, A. Protat, M. D. Shupe, S. A. McFarlane, J. M. Comstock, J. Delano, M. Deng, M. Dunn, R. J. Hogan, D. Huang, M. P. Jensen, G. G. MacE, R. McCoy, E. J. O'Connor, D. D. Turner, and Z. Wang, "Toward understanding of differences in current cloud retrievals of ARM ground-based measurements," *J. Geophys. Res. Atmos.*, vol. 117, no. 10, 2012.

- [11] G. Maschwitz, U. Löhnert, S. Crewell, T. Rose, and D. D. Turner, "Investigation of ground-based microwave radiometer calibration techniques at 530 hPa," *Atmos. Meas. Tech.*, vol. 6, no. 10, pp. 2641–2658, 2013.
- [12] V. Meunier, U. Löhnert, P. Kollias, and S. Crewell, "Biases caused by the instrument bandwidth and beam width on simulated brightness temperature measurements from scanning microwave radiometers," *Atmos. Meas. Tech.*, vol. 6, no. 5, pp. 1171–1187, 2013.
- [13] A. S. Frisch, G. Feingold, C. W. Fairall, T. Uttal, and J. B. Snider, "On cloud radar and microwave radiometer measurements of stratus cloud liquid water profiles," *J. Geophys. Res. Atmos.*, vol. 103, no. 18, pp. 23 195–23 197, 1998.
- [14] S. Frisch, M. Shupe, I. Djalalova, G. Feingold, and M. Poellot, "The retrieval of stratus cloud droplet effective radius with cloud radars," *J. Atmos. Ocean. Tech.*, vol. 19, no. 6, pp. 835–842, 2002.
- [15] U. Görndorf, V. Lehmann, M. Bauer-Pfundstein, G. Peters, D. Vavriv, V. Vinogradov, and V. Volkov, "A 35-GHz polarimetric doppler radar for long-term observations of cloud parameters-description of system and data processing," *J. Atmos. Ocean. Tech.*, vol. 32, no. 4, pp. 675–690, 2015.
- [16] J. Delanoë, A. Protat, J.-P. Vinson, W. Brett, C. Caudoux, F. Bertrand, J. P. du Chatelet, R. Hallali, L. Barthes, M. Haeffelin, and J.-C. Dupont, "BASTA: A 95-GHz FMCW Doppler Radar for Cloud and Fog Studies," *J. Atmos. Ocean. Tech.*, vol. 33, no. 5, pp. 1023–1038, 2016. [Online]. Available: <http://dx.doi.org/10.1175/JTECH-D-15-0104.1>
- [17] N. Küchler, S. Kneifel, U. Löhnert, P. Kollias, H. Czekala, and T. Rose, "A W-Band RadarRadiometer System for Accurate and Continuous Monitoring of Clouds and Precipitation," *J. Atmos. Ocean. Tech.*, vol. 34, no. 11, pp. 2375–2392, 2017. [Online]. Available: <http://journals.ametsoc.org/doi/10.1175/JTECH-D-17-0019.1>
- [18] T. Rose, S. Crewell, U. Löhnert, and C. Simmer, "A network suitable microwave radiometer for operational monitoring of the cloudy atmosphere," *Atmo. Res.*, vol. 75, no. 3, pp. 183–200, 2005.
- [19] R. Ware, R. Carpenter, J. Güldner, J. Liljegren, T. Nehr Korn, F. Solheim, and F. Vandenbergh, "A multichannel radiometric profiler of temperature, humidity, and cloud liquid," *Radio Sci.*, vol. 38, no. 4, pp. n/a–n/a, 2003. [Online]. Available: <http://doi.wiley.com/10.1029/2002RS002856>
- [20] A. Macke, P. Seifert, H. Baars, C. Barthlott, C. Beekmans, A. Behrendt, B. Bohn, M. Brueck, J. Bühl, S. Crewell, T. Damian, H. Deneke, S. Düsing, A. Foth, P. Di Girolamo, E. Hamann, R. Heinze, A. Hirsikko, J. Kalisch, N. Kalthoff, S. Kinne, M. Kohler, U. Löhnert, B. Lakshmi Madhavani, V. Maurer, S. Kumar Muppa, J. Schween, I. Serikov, H. Siebert, C. Simmer, F. Späth, S. Steinke, K. Trümmer, S. Trömel, B. Wehner, A. Wieser, V. Wulfmeyer, and X. Xie, "The HD(CP)2 Observational Prototype Experiment (HOPE) - An overview," *Atmos. Chem. Phys.*, vol. 17, no. 7, pp. 4887–4914, 2017.
- [21] S. Kneifel, A. Lerber, J. Tiira, D. Moisseev, P. Kollias, and J. Leinonen, "Observed relations between snowfall microphysics and triple-frequency radar measurements," *J. Geophys. Res. Atmos.*, vol. 120, no. 12, pp. 6034–6055, 2015.
- [22] D. L. Sisterson, R. A. Peppler, T. S. Cress, P. J. Lamb, and D. D. Turner, "The ARM Southern Great Plains (SGP) Site," *Meteor. Mon.*, vol. 57, pp. 6.1–6.14, 2016. [Online]. Available: <http://journals.ametsoc.org/doi/10.1175/AMSMONOGRAPHIS-D-16-0004.1>
- [23] G. L. Stephens, G. W. Paltridge, and C. M. R. Platt, "Radiation Profiles in Extended Water Clouds. III: Observations," *J. Atmos. Sci.*, vol. 35, no. 11, pp. 2133–2141, 1978. [Online]. Available: <http://journals.ametsoc.org/doi/abs/10.1175/1520-0469%281978%29035%3C2133%3ARPIEWC%3E2.0.CO%3B2>
- [24] S. Crewell, H. Czekala, U. Löhnert, C. Simmer, T. Rose, R. Zimmermann, and R. Zimmermann, "Microwave Radiometer for Cloud Cartography: A 22-channel ground-based microwave radiometer for atmospheric research," *Radio Sci.*, vol. 36, no. 4, pp. 621–638, 2001. [Online]. Available: [10.1029/2000RS002396](https://doi.org/10.1029/2000RS002396)
- [25] M. Maahn, U. Löhnert, P. Kollias, R. C. Jackson, and G. M. McFarquhar, "Developing and Evaluating Ice Cloud Parameterizations for Forward Modeling of Radar Moments Using In Situ Aircraft Observations," *J. Atmos. Ocean. Tech.*, vol. 32, no. 5, pp. 880–903, 2015. [Online]. Available: <http://journals.ametsoc.org/doi/abs/10.1175/JTECH-D-14-00112.1>
- [26] N. L. Miles, J. Verlinde, and E. E. Clothiaux, "Cloud Droplet Size Distributions in Low-Level Stratiform Clouds," *J. Atmos. Sci.*, vol. 57, no. 2, pp. 295–311, 2000.
- [27] U. Löhnert and S. Crewell, "Accuracy of cloud liquid water path from ground-based microwave radiometry 1. Dependency on cloud model statistics," *Radio Sci.*, vol. 38, no. 3, pp. 1–11, 2003.
- [28] D. D. Turner, S. A. Clough, J. C. Liljegren, E. E. Clothiaux, K. E. Cady-Pereira, and K. L. Gaustad, "Retrieving Liquid Water Path and Precipitable Water Vapor From the Atmospheric Radiation Measurement (ARM) Microwave Radiometers," *Trans. Geosci. Remote Sens.*, vol. 45, no. 11, pp. 3680–3690, 2007.
- [29] K. Ebell, U. Löhnert, E. Päsche, E. Orlandi, J. H. Schween, and S. Crewell, "A 1-D variational retrieval of temperature, humidity, and liquid cloud properties: performance under idealized and real conditions," *J. Geophys. Res. Atmos.*, vol. 122, no. 3, pp. 1746–1766, 2017. [Online]. Available: <https://doi.org/10.1002/2016JD025945>
- [30] N. Küchler, S. Kneifel, U. Löhnert, and P. Kollias, "Revisiting Liquid Water Content Retrievals in Warm Stratified Clouds: The Modified Frisch," *Geophys. Res. Lett.*, vol. 45, no. 17, pp. 9323–9330, 2018. [Online]. Available: <https://doi.org/10.1029/2018GL079845>
- [31] K. Ebell, U. Löhnert, S. Crewell, and D. D. Turner, "On characterizing the error in a remotely sensed liquid water content profile," *Atmos. Res.*, vol. 98, no. 1, pp. 57–68, 2009. [Online]. Available: <https://doi.org/10.1016/j.atmosres.2010.06.002>

## 5.2 Publication III

N. Kuchler et al. (2018). "Revisiting liquid water content retrievals in warm stratified clouds: The modified Frisch". In: *Geophysical Research Letters* 45.17. DOI: <https://doi.org/10.1029/2018GL079845>



**RESEARCH LETTER**

10.1029/2018GL079845

**Revisiting Liquid Water Content Retrievals in Warm Stratified Clouds: The Modified Frisch**

**N. K uchler<sup>1</sup>, S. Kneifel<sup>1</sup>, P. Kollias<sup>1,2</sup>, and U. L ohnert<sup>1</sup>**

<sup>1</sup>Institute for Geophysics and Meteorology, University of Cologne, Cologne, Germany, <sup>2</sup>School of Marine and Atmospheric Sciences, State University of New York at Stony Brook, NY, USA

**Key Points:**

- Determining the liquid water content in nondrizzling and drizzling stratified clouds using radar and microwave radiometry
- The retrieval separates the cloud into a drizzling and a quasi nondrizzling region using radar Doppler spectra processing
- The retrieval uncertainty is by up to a factor of four smaller than current retrieval techniques under drizzling and nondrizzling conditions

**Supporting Information:**

- Supporting information S1
- Figure S1
- Figure S2

**Correspondence to:**

N. K uchler,  
nkuech@meteo.uni-koeln.de

**Citation:**

K uchler, N., Kneifel, S., Kollias, P., & L ohnert, U. (2018). Revisiting liquid water content retrievals in warm stratified clouds: The modified Frisch. *Geophysical Research Letters*, 45, 9323–9330. <https://doi.org/10.1029/2018GL079845>

Received 5 APR 2018

Accepted 28 AUG 2018

Accepted article online 4 SEP 2018

Published online 14 SEP 2018

**Abstract** Accurate observations of liquid water content (LWC) in warm stratiform clouds are important for quantifying their radiative and hydrological effects and for studying aerosol-cloud interactions. Retrieving LWC from radar reflectivity under drizzling or nondrizzling conditions has been investigated for several decades by the cloud remote sensing community. However, no physically plausible framework exists to address the biases introduced by drizzle on existing retrieval techniques. We present the *modified Frisch* retrieval (ModFrisch), which combines radar and microwave radiometer measurements to retrieve LWC in both nondrizzling and drizzling conditions. It is shown, using a 1-D steady state microphysical model and a radar simulator, that the uncertainty of ModFrisch is up to four times smaller than the uncertainty of similar retrievals under drizzling conditions, enabling LWC profiling with an accuracy of 20%. The performance of the ModFrisch technique is evaluated using 1 year of observations.

**Plain Language Summary** It is important to measure the vertical structure of clouds accurately to create reliable climatological records and to investigate how well clouds can be predicted by weather and climate models. A commonly used technique to determine the liquid water content of stratified clouds is based on two standard instruments: a radar, providing profile information, and a microwave radiometer providing the total amount of liquid in the cloud. However, if the cloud droplets are too big (larger than about 50–70  $\mu\text{m}$ ), the vertical profile of the radar measurement cannot be related to the profile of liquid water content. Unfortunately, most stratus clouds contain liquid drops (drizzle) that exceed that critical size leading to a big lack of accurate data. In our study, we separate the cloud into two regions: the upper part of the cloud where drizzle has no significant influence and the lower part where drizzle is present. In the upper part, we apply a commonly used retrieval while assuming a linearly increasing liquid water content in the lower part, which has been shown to be valid in previous studies. Thus, we can potentially provide a more reliable basis of observational liquid water contents to constrain model simulations.

**1. Introduction**

We present a new retrieval approach that contributes to solving a problem that has been present in remote sensing of stratiform clouds for several decades: the retrieval of liquid water content (LWC) profiles under both nondrizzling and drizzling conditions using radar reflectivity measurements (e.g., Atlas, 1954; Kogan et al., 2007).

Stratocumulus clouds cover on average about 20% of the planet and thereby strongly influence the radiation budget of the Earth (Wood, 2012). These stratiform warm layers are challenging to represent in global circulation models (Boucher et al., 2013), and their formation, maintenance, and dissipation depend on several processes that control and depend on the vertical structure of LWC in these cloud systems (Wood, 2012). Therefore, accurate observations of LWC are desirable to evaluate models and their parameterizations.

Retrieving LWC in warm stratiform clouds requires information on the vertical structure of the hydrometeors, thus, often, is based on radar measurements (e.g., Atlas, 1954; Fox & Illingworth, 1997; Kogan et al., 2007; Sauvageot & Omar, 1987; Wang & Geerts, 2003) or a combination of radar with one or several additional instruments (e.g., Dong & Mace, 2003; Fielding et al., 2014; Frisch et al., 1995; Hogan et al., 2005; Huang et al., 2009; Li & Min, 2013; L ohnert et al., 2001; O’Connor et al., 2005; Rusli et al., 2017). A radar-independent method is the so-called *linear-scaled* approach distributing the column-integrated liquid water path (LWP) from a microwave radiometer (MWR) linearly, so that LWC is zero at cloud base and maximal at cloud top. This technique is widely used for cloud data products based on ground-based observations (e.g., CLOUDNET; Illingworth et al., 2007).

 2018. The Authors.

This is an open access article under the terms of the Creative Commons Attribution-NonCommercial-NoDerivs License, which permits use and distribution in any medium, provided the original work is properly cited, the use is non-commercial and no modifications or adaptations are made.



The most commonly applied cloud retrievals combine radar and MWR to derive LWC profiles (Zhao et al., 2012): The LWP from a MWR constrains the retrieval, while the radar reflectivity ( $Z_e$ ) determines the shape of the LWC profile (Frisch et al., 1995). As a few drizzle drops can dominate  $Z_e$  while negligibly contributing to LWC (Fox & Illingworth, 1997), the accuracy of those retrievals deteriorates once drizzle is present in the cloud (Khain et al., 2008; Pujol et al., 2007). This is particularly unfortunate as drizzle is often found in marine stratocumulus clouds (Stevens et al., 2003).

Here we introduce the *modified Frisch* retrieval (henceforth: ModFrisch). ModFrisch is a modified version of the LWC retrieval according to Frisch et al. (1998; henceforth: StandFrisch for *standard Frisch*), combining radar and MWR to retrieve LWC profiles. In contrast to StandFrisch, ModFrisch can determine LWC profiles in both nondrizzling and drizzling clouds. Thereby, ModFrisch identifies the region in the cloud where the main assumptions of StandFrisch are still valid: the droplet number concentration ( $N$ ) is approximately constant with height (Nicholls, 1987), and the third and the sixth moments of drop size distribution (DSD) are linearly related (Atlas, 1954). In that case, the LWC is a function of LWP and  $Z_e$  only.

Section 2 provides an overview of the theory and the models that were used to develop ModFrisch. Section 3 is the core of this study describing ModFrisch by presenting the algorithm, evaluating its performance, and giving uncertainty estimates. In the last section, we conclude and give an outlook.

## 2. Methodology

ModFrisch was developed using a modified version of the microphysical model by Kollias, Szyrmer, et al. (2011; henceforth: MiMo) and a radar forward simulator that is embedded in the Passive and Active Microwave Radiative Transfer Model (PAMTRA; Maahn et al., 2015). MiMo is a steady state, 1-D microphysical model that parameterizes autoconversion and explicitly resolves the accretion process using DSDs of cloud and drizzle particles. MiMo output includes profiles of cloud and drizzle DSDs for different LWP and  $N$ . MiMo permits different types of LWC profiles, one near-adiabatic with a maximum LWC at 0.9 normalized cloud depth height and one with considerable cloud-top mixing where the maximum LWC is deeper in the cloud at 0.75 normalized cloud depth height. In total, 360 LWC profiles were generated by MiMo for a wide range of warm stratiform cloud conditions. Details for the model setup can be found in the Appendix A. The DSDs produced by MiMo were used as input for PAMTRA to calculate radar Doppler spectra and their moments, such as  $Z_e$  and skewness. Finally, LWC profiles were obtained with StandFrisch (Frisch et al., 1998) by using the forward-modeled  $Z_e$  and LWP from MiMo (which implies the assumption of an accurate LWP retrieval):

$$LWC(i) = \frac{LWP \sqrt{Z_e(i)}}{\sum_{j=1}^m \Delta z(j) \sqrt{Z_e(j)}}. \quad (1)$$

Indexes  $i$  and  $j$  indicate respective cloud layers,  $\Delta z(j)$  is the radar vertical grid size, and  $m$  is the number of layers. Once a LWC profile is retrieved with equation (1), it can be directly compared to the reference profile from MiMo. Equation (1) is unaffected by any calibration offset in  $Z_e$ . Any relative bias of LWP translates into the same relative bias in LWC at any level.

In the Rayleigh backscattering regime,  $Z_e$  is proportional to the sixth power of the particle diameter (Petty, 2006, p. 378), while LWC scales with the third power. Therefore, a small amount of drizzle can significantly increase  $Z_e$  while barely contributing to the LWC. That is, the assumption of StandFrisch, that the third moment of the observed DSD is linearly related to its sixth moment, does not apply. Thus, the shape of  $Z_e$  does not represent the shape of the LWC profile. ModFrisch, which we will introduce in the following, is unaffected by drizzle contamination and works under both nondrizzling and drizzling conditions.

## 3. The ModFrisch

ModFrisch combines StandFrisch with the linear-scaled method in an optimal way: the linear-scaled method is resilient against drizzle contamination because it assumes a linearly increasing LWC, which is valid for example in marine stratocumulus (Wood, 2012). As drizzle typically affects the bottom half of the  $Z_e$  profiles, the linear-scaled method is applied in those regions, where StandFrisch cannot provide reasonable estimates of LWC. In drizzle-free regions (the upper part of the cloud), the LWC profile is scaled with  $Z_e$  according to StandFrisch.

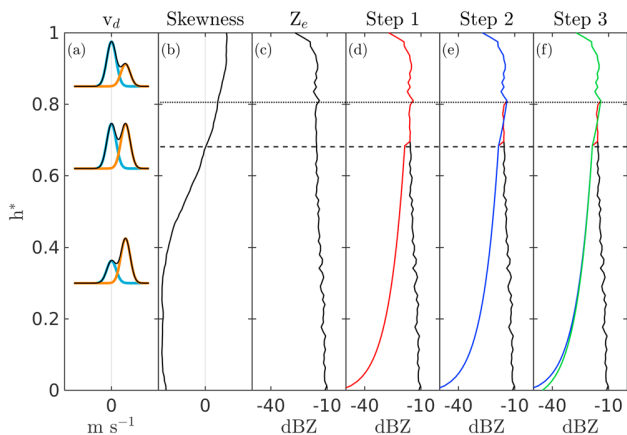


**Figure 1.** Sketch of modified Frisch.  $h^*$  indicates the height above cloud base normalized with the cloud thickness. (a) Typical Doppler spectra (black) of a warm cloud with cloud droplets (light blue) and developing drizzle (orange). (b) Corresponding skewness profile of the (black) Doppler spectra. (c) Reflectivity  $Z_e$  of Doppler spectra. (d) Step 1: Modified  $Z_e$  signal (red) using the original signal above the ZSH (dashed horizontal line) and assuming a linear decrease of  $\sqrt{Z_e}$  to zero at cloud base. (e) Step 2: To smooth the kink introduced at ZSH,  $\sqrt{Z_e}$  is interpolated between ZSH and the maximum of the  $Z_e$  profile (dotted horizontal line) obtained in step 1. (f) If cloud base liquid water content is available independently, the retrieval is constrained by increasing  $Z_e$  at cloud base (green line) while all values above ZSH stay fixed until the retrieval agrees with the independent liquid water content estimate at cloud base. ZSH = zero-skewness-height.

### 3.1. Separating Drizzle and Cloud Mode Using Skewness

Figures 1a and 1b illustrate the concept of ModFrisch by exhibiting profiles of typical Doppler spectra and the corresponding skewness profile of a cloud that contains drizzle initiated at cloud top.  $Z_e$  is dominated by cloud droplets at cloud top, although the initialized drizzle already shows up in the Doppler spectrum at larger velocities due to its larger sedimentation velocity (note that positive velocity values correspond to motion toward the ground). As a result, the Doppler spectrum deviates from a bell-shaped distribution at the right tail, which is reflected in the positive skewness of the spectrum at cloud top. At cloud base, drizzle drops have significantly grown by accretion while sedimenting through the cloud and dominate the Doppler spectrum leading to a negative skewness (Kollias, Rémillard, et al., 2011; Kollias, Szyrmer et al., 2011).

ModFrisch assumes that both spectra, that is, for cloud droplets and drizzle, are symmetric and bell-shaped, which was found to be a valid approximation for the data used here. This has also been found in observations (Luke & Kollias, 2013). Thus, the nondrizzling and drizzling regions can be separated if the transition zone of the skewness, that is, the point where the skewness turns from positive to negative (henceforth ZSH for zero-skewness-height), can be identified. At this point, ideally both spectra contribute equally to  $Z_e$ , thus, the ratio between drizzle-mode reflectivity  $Z_d$  and cloud-mode reflectivity  $Z_c$  equals one (henceforth  $Z_d/Z_c$ ). In other words,  $Z_c$  can be obtained by taking half of the measured  $Z_e$  where ZSH is zero.

Note that Figure 1 is based on the assumption of low turbulence. Luke and Kollias (2013) showed that in the presence of turbulence, the skewness of

a Doppler spectrum can be equal to zero, although containing both drizzle and cloud droplets. In such cases, determining the height where  $Z_d/Z_c$  equals one from the skewness profile becomes difficult. This will be further discussed in section 3.3.

### 3.2. Retrieval Algorithm

In the first step, ModFrisch uses  $Z_c$ , determined at ZSH, as reference point in the cloud. Above ZSH, the original  $Z_e$  signal is considered to be linearly related to  $LWC^2$ , that is, StandFrisch is valid and  $Z_e$  remains unchanged. The part below ZSH is modified by assuming a linear increase of LWC that corresponds to a linear increase of the square root of  $Z_e$ , being zero at cloud base and  $\sqrt{Z_c}$  at ZSH (according to equation (1)). The resulting first-order modified profile is illustrated in Figure 1d. Note that drizzle also contributes to  $Z_e$  above ZSH. However, assuming a decrease of  $Z_d$  toward cloud top, the maximum uncertainty in  $Z_e$  associated with the presence of drizzle is 3 dB and decreases toward cloud top. In the second step (Figure 1e), the artificially introduced kink in the  $Z_e$  profile (at ZSH) is smoothed out by linearly interpolating between  $\sqrt{Z_c}$  and the square root of the maximum reflectivity ( $\sqrt{Z_e^{max}}$ ) of the first-order modified profile. The third step is only performed when LWC at cloud base ( $LWC_b$ ) can be estimated (e.g., O'Connor et al., 2005): ModFrisch still assumes a linearly increasing profile; however, while  $Z_c$  is fixed at ZSH,  $Z_e$  is iteratively increased at cloud base until the retrieved LWC at cloud base agrees with  $LWC_b$ . Note that O'Connor et al. (2005) retrieve drizzle-LWC below cloud base. We assumed that  $LWC_b$  is dominated by drizzle and thereby similar to the value obtained after O'Connor et al. (2005). Thus, ModFrisch uses  $LWC_b$  to construct a reflectivity profile that corresponds to a nondrizzling cloud with linearly increasing LWC that is equal to  $LWC_b$  at cloud base. Note further that if no transition from positive to negative skewness is detected in the first place, the StandFrisch will be applied.

### 3.3. Model Study

We clustered the 360 LWC profiles in two steps: first, the profiles were separated into cloud type 1 and cloud type 2 (see section 2); and in the second step, the data set was divided into nondrizzling/low-drizzling and drizzling cases by looking for the location of  $Z_e^{max}$  in the profile. If  $Z_e^{max}$  was above cloud center, the profile was classified as nondrizzling/low-drizzling. We found that this worked well for our model study; however, investigations whether that applies also to observations are beyond the scope of this work.

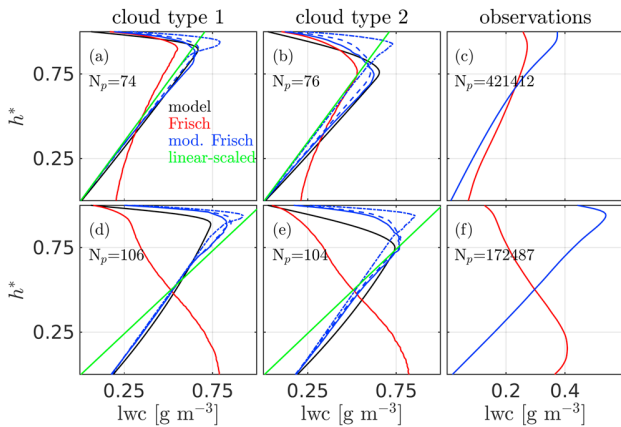


**Figure 2.** (a) Comparison (74 profiles) between microphysical model mean profiles (black) and several LWC retrievals for model cloud type 1 and nondrizzling/low-drizzling cases: the linear-scaled method (green), standard Frisch (red), and ModFrisch (blue; under low- [solid], medium- [dashed], and high-turbulent [dotted-dashed] conditions). (b) Like (a) but for cloud type 2. (c) Mean values of standard Frisch and ModFrisch applied to 421,412 observations of nondrizzling single-layer liquid-clouds classified by CLOUDNET (Illingworth et al., 2007). The observations were recorded at the Jülich Observatory for Cloud Evolution - Central Facility between 2012 and 2013. (d) Like (a) but for drizzling cases. (e) Like (b) but for drizzling cases. (f) Like (c) but for 172,487 drizzling cases. LWC = liquid water content; ModFrisch = modified Frisch.

Figure 2 shows averaged LWC profiles that were retrieved with the linear-scaled method, StandFrisch and ModFrisch under low-, medium-, and high-turbulent conditions in comparison to the averaged reference profiles from MiMo. Note that only ModFrisch is influenced by turbulence. In nondrizzling/low-drizzling cases and cloud type 1 (Figure 2a), the linear-scaled method follows closely the averaged reference profile until the latter reaches its maximum and then decreases toward cloud top. This clearly shows the limitation of the linear-scaled method exhibiting a large uncertainty when the maximum LWC is located at larger distance from cloud top (Figure 2b). StandFrisch captures the location of the profile's maximum and agrees well with the reference above the maximum for both cloud types. Drizzle at cloud base, which does not contribute much to LWC but to  $Z_e$ , leads to an overestimation of LWC at cloud base and an underestimation of the maximum. In low-turbulent cases, ModFrisch captures the shape of the reference profile at cloud top and is not affected by drizzle occurring at cloud base. Therefore, not only can the shape be reconstructed, but also a good estimate of the maximum is provided for both cloud types in nondrizzling/low-drizzling cases. In medium-turbulent cases, the retrieval still provides reasonable estimates, whereas the maximum LWC is slightly shifted toward cloud top. This shift is caused by cases where ZSH is estimated to be located above the maximum LWC. In case of high turbulence, ZSH is strongly overestimated, leading to the retrieved maximum being located close to cloud top. Additionally, the maximum LWC is overestimated too.

In drizzling cases, the linear-scaled method does not provide LWC at cloud base due to the inherent assumption of the retrieval. As a consequence, the LWC at cloud top is highly overestimated. However, the linear-scaled method yields still more reasonable results than StandFrisch. StandFrisch does not recover the shapes of LWC profiles at all, because drizzle dominates  $Z_e$ . In contrast, ModFrisch fits the reference profiles for both cloud types in low-turbulent cases, though, slightly underestimates (overestimates) LWC below (at and above) the maximum. As in nondrizzling/low-drizzling cases, ModFrisch provides similar results for medium turbulence as for low turbulence. When turbulence is high, ModFrisch overestimates the location of the maximum of the LWC profile. Nevertheless, ModFrisch still provides better estimates of LWC than both StandFrisch and the linear-scaled method. Note that if LWC at cloud base cannot be determined a priori the profile of ModFrisch will indeed conserve the shape, but it will underestimate (overestimate) LWC at cloud base (at the maximum). For simplicity, we constrained ModFrisch using  $LWC_b$  from MiMo, that is, the reference *truth*, instead of retrieving  $LWC_b$  following, for example, O'Connor et al. (2005).

### 3.4. Uncertainty Estimates

To provide a first estimate of the retrieval uncertainty, we define the normalized LWP error

$$\Delta LWP_{norm} = \frac{\sum_{i=1}^m \Delta z_i |\Delta LWC_i|}{LWP}, \quad (2)$$

with the absolute LWC deviation  $|\Delta LWC_i|$  between the retrieval and the model reference and the measured LWP (here taken from MiMo). Note that in this study, the drizzle LWP below cloud base is less than 10% (1%) of the total LWP in 100% (83%) of all cases, thus, the normalized error due to LWP below cloud base is always smaller than 10%.

Figure 3a, based on a low turbulence, shows  $\Delta LWP_{norm}$  as a function of  $Z_e^{max}$  of the original profile,  $N$ , and LWP of the cloud mode. The latter was used because it is conserved in MiMo and therefore simplifies the illustration. The uncertainty of the linear-scaled method is reflected in two lines with a constant offset until  $-10$  dBZ. The two lines correspond to the two different cloud types, that is, the two different heights of maximum LWC above which the reference profile decreases, while the LWC profile of the linear-scaled method constantly increases. Beyond  $-10$  dBZ, the contribution of drizzle to LWC increases, being the strongest at cloud base, further increasing  $\Delta LWP_{norm}$ .

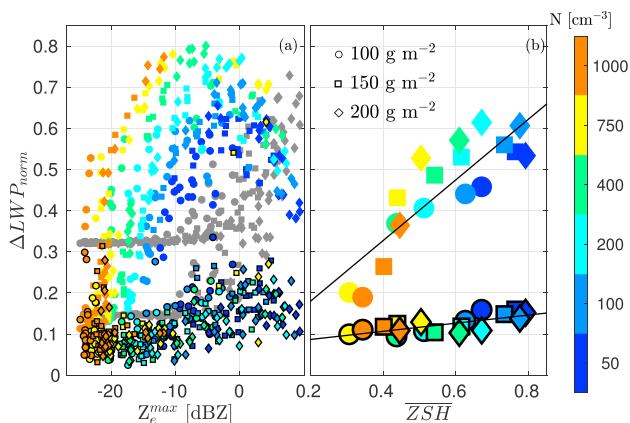


**Figure 3.** (a) Normalized uncertainty ( $\Delta LWP_{norm}$ ) of the linear-scaled method (gray), standard Frisch (colored points) and modified Frisch (colored points with black edges) as a function of the maximum reflectivity ( $Z_e^{max}$ ) observed in the original profile, cloud droplet number concentration  $N$  (colors), and the cloud LWP (symbol shape). (b) Mean  $\Delta LWP_{norm}$  versus mean ZSH for standard Frisch and modified Frisch. Symbols and colors like in (a). Low turbulence was assumed in (a) and (b). LWP = liquid water path; ZSH = zero-skewness-height.

The uncertainty of StandFrisch increases almost linearly up to  $-10$  dBZ; however, exhibiting a large scatter when considering  $\Delta LWP_{norm}$  as a function of  $Z_e^{max}$  only. By including  $N$ , a clear separation is apparent: the lower  $N$ , the larger  $Z_e^{max}$  found in the profile and the larger  $N$ , the smaller the average uncertainty (Figure 3b). Furthermore, the uncertainty also increases with increasing LWP. The maximum of  $\Delta LWP_{norm}$  for StandFrisch is found at around  $-8$  dBZ. The decrease after that point is associated with an increasing amount of drizzle at cloud base that contributes to LWC and therefore compensates the strong overestimation by StandFrisch. ModFrisch significantly decreases  $\Delta LWP_{norm}$  (by up to a factor of 4) in comparison to StandFrisch. Moreover,  $\Delta LWP_{norm}$  is smaller than 35% for any turbulent condition. At high turbulence,  $\Delta LWP_{norm}$  exhibits a structure similar to the linear-scaled method (not shown) for  $Z_e$  smaller than  $-5$  dBZ due to the overestimation of the magnitude and location of the maximum LWC, and slightly decreases toward larger  $Z_e$ .

Figure 3b illustrates the mean uncertainty as a function of mean ZSH. It shows three main features: first, the uncertainty of LWC increases with decreasing  $N$ . This can be explained by the development of larger (drizzle) droplets increasing  $Z_e$  while LWC is conserved. Second, the uncertainty of LWC increases with increasing LWP. This is due to the parameterization of the accretion rate, being a function of LWP, increasing the growth rate. And third, ZSH is negatively correlated with  $N$ . The smaller  $N$  leads to a more

effective generation of larger drizzle drops closer to cloud top, which dominate  $Z_e$ . The mean of  $\Delta LWP_{norm}$  of ModFrisch is below 20% for any combination of  $N$ , LWP, and cloud type.  $\Delta LWP_{norm}$  slightly increases with turbulence, but remains below 20% for both medium and high turbulence.

The results show that ModFrisch performs significantly better than StandFrisch and the linear-scaled method, especially when drizzle is present. We found that the mean uncertainty of ModFrisch stays below 20%, independent of LWP and  $N$ . In contrast, the uncertainty of StandFrisch strongly increases with decreasing  $N$  and increasing LWP.

### 3.5. Case Study

ModFrisch and StandFrisch were applied to observations recorded at the *Jülich Observatory for Cloud Evolution - Central Facility* (Löhnert et al., 2015) between March 2012 and March 2013. The data set contains only single-layer liquid-clouds classified by the CLOUDNET algorithm (Illingworth et al., 2007), composed of 421,124 nondrizzling and 172,487 drizzling cases. The retrieved mean profiles in Figures 2c and 2f show structures very similar to the model study in section 3.3 for nondrizzling and drizzling conditions, respectively. This suggests that ModFrisch improves the derivation of LWC profiles when drizzle is present. Note that drizzle-LWC below cloud base after O'Connor et al. (2005) could not be determined, because calibrated lidar data were not available. Thus, step 3 of ModFrisch could not be performed. Yet LWC at cloud base is on average larger than zero in both Figures 2c and 2f, which is due to cases where StandFrisch had to be applied because ModFrisch could not determine a ZSH (1% and 10% of drizzling and nondrizzling cases, respectively).

The mean ZSHs in drizzling and nondrizzling cases are 0.75 and 0.71, respectively. In the model study, values of 0.80 (0.88 and 0.90) and 0.37 (0.46 and 0.90) were found under low (medium and high) turbulence for drizzling and nondrizzling cases, respectively. The larger values in nondrizzling clouds are caused by cases with low  $Z_e^{max}$ , in which the skewness is close to zero in the entire profile. Thus, turbulence, increasing the noise of the skewness, causes transitions that are close to cloud top. In general, both studies show similar results. Comparing the mean ZSHs found in the model study under nondrizzling conditions with the 0.71 found in the observations indicate the prevalence of medium-turbulent to highly turbulent conditions during the observation period.

## 4. Conclusion and Outlook

The ModFrisch is a generalization of the LWC retrieval by Frisch et al. (1998; StandFrisch) combining radar and MWR measurements. StandFrisch only works as long as drizzle does not contribute significantly to the radar reflectivity signal ( $Z_e$ ). ModFrisch identifies at which height above cloud base drizzle starts to affect  $Z_e$  by analyzing the radar Doppler spectra skewness profile. It was found that where the skewness turns from

positive to negative (ZSH), starting at cloud top, drizzle already makes half of  $Z_e$ . Hence, StandFrisch is not applicable below ZSH, and ModFrisch assumes a linearly increasing LWC profile. Above ZSH, the LWC profile is scaled by  $Z_e$  following StandFrisch. A model study and an observational study revealed that ModFrisch provides reasonable estimates of LWC also when drizzle dominates  $Z_e$  in the lower part of the cloud. This is an improvement to StandFrisch that fails once the cloud contains drizzle.

In the model study, drizzling and nondrizzling/low-drizzling cases could be clearly separated by the location of the maximum  $Z_e$  ( $Z_e^{max}$ ) in the profile:  $Z_e^{max}$  was found close to cloud base (cloud top) in drizzling (non-/low-) drizzling cases. This clear signature is a result of the setup of the microphysical model used in this study: once drizzle is initiated at cloud top, it grows by accretion while sedimenting toward cloud base. However, we do not expect to find such an ideal process in observations. ModFrisch reduced the cumulative retrieval error by up to a factor of four being below 20% for all drizzle loads and turbulence scenarios that were simulated in this study. The retrieval error increases slightly with turbulence that enhances the noise of the skewness signal impeding the separation between drizzle-dominated and quasi drizzle-free regions. Note that the  $Z_e$  signal, being identified as quasi drizzle free, is associated with a maximum uncertainty of 3 dB.

ModFrisch was applied to observations of drizzling and nondrizzling single-layer liquid-clouds classified by the CLOUDNET algorithm (Illingworth et al., 2007). The results show large similarity with the findings of the model study and therefore indicate that ModFrisch can be used to determine LWC profiles under drizzling conditions. In nondrizzling cases, ModFrisch determines ZSH closer to cloud top than expected (similar in the model study under increased turbulence). This can be avoided if the ModFrisch is only applied above a certain  $Z_e$ -threshold indicating the presence of drizzle. Nevertheless, we expect that the overestimation of ZSH does not affect the retrieval uncertainty as long as the LWC profile has a linear-like shape, is close to zero at cloud base, and has its maximum close to cloud top. However, due to a missing independent observational reference, a final conclusion on the accuracy of ModFrisch is left for future studies.

In general, the correct estimation of LWC at cloud base once drizzle contributes significantly to the LWC must be considered as further uncertainty source, as well as the uncertainty of the LWP estimate by the MWR. Moreover, the quality of the retrieved LWC profile decreases with increasing turbulence and is therefore a crucial part in the algorithm of ModFrisch, especially as eddy dissipation rates of about typically  $10^{-3} \text{ m}^2/\text{s}^3$  (corresponding to medium to high turbulence used here) occur in stratiform clouds (e.g., Fang et al., 2014). However, the general concept of identifying drizzling and drizzle-free regions in the cloud using skewness has high potential to increase the accuracy of LWC retrievals. This study yielded promising results, though, further research is needed to evaluate ModFrisch with independent references, such as Large Eddy Simulations or in situ measurements. How to localize drizzle correctly remains a key question whose answer would not only improve ModFrisch but also other retrieval algorithms.

## Appendix A: Model Setups

MiMo is a 1-D steady state model that approximates the evolution of drizzle spectra depending on the distance fallen through a cloud (Acquistapace, 2016). Cloud droplets are log-normal distributed and  $N$  is constant. The DSDs are provided with a 5-m vertical resolution. Drizzle initiation was calculated with five different parameterizations (Franklin, 2008; Khairoutdinov & Kogan, 2000; Seifert et al., 2010; Tripoli & Cotton, 1980; Xie & Liu, 2009), while two different minimum initial drizzle sizes of 60 and 80  $\mu\text{m}$  were used. Once the respective minimum drizzle drop size is reached, the model calculates further growth using the accretion scheme by Long (1974) assuming fall velocities according to Beard (1976). To represent variable cloud conditions, several values for  $N$  (50, 100, 200, 400, 750, and 1,000  $\text{cm}^{-3}$ ) and cloud LWP (100, 150, and 200  $\text{g}/\text{m}^2$ ) were used. Due to steady state conditions, the cloud LWP is permanently replenished once cloud droplets transition to drizzle, that is, the cloud LWP is constant while the drizzle LWP increases by accretion.

In PAMTRA, spectral width broadening (Doviak et al., 1979) was accounted for by assuming a half power beam width of  $0.6^\circ$ , a radar frequency of 35 GHz, a horizontal wind of 10 m/s, and three different eddy dissipation rates, that is,  $10^{-6}$  (low),  $10^{-4}$  (medium),  $10^{-2} \text{ m}^2/\text{s}^3$  (high; Borque et al., 2016). The radar noise floor was set to  $-38 \text{ dBZ}$  at 1 km distance and cloud base was assumed to be located at 1,400 m radial distance to a zenith-pointing radar. No spatial averaging was applied to the simulated radar profiles of 5-m resolution in order to avoid smearing effects due to finite pulse length; recently available cloud radars are already able to provide such high resolution observations (e.g., K uchler et al., 2017).

## Acronyms

**DSD** = drop size distribution  
 $h^*$  = normalized height above cloud base  
**LWC** = liquid water content  
**LWC<sub>b</sub>** = liquid water content at cloud base  
**LWP** = liquid water path  
 $\Delta LWP_{norm}$  = cumulative retrieval error  
**MiMo** = 1-D steady state microphysical model  
**ModFrisch** = modified Frisch  
**MWR** = microwave radiometer  
 $N$  = droplet number concentration  
**PAMTRA** = Passive and Active Microwave Radiative Transfer Model  
**PDF** = probability density function  
**StandFrisch** = standard Frisch  
 $\Delta z$  = radar range resolution  
 $Z_c$  = radar reflectivity of cloud droplets  
 $Z_d$  = radar reflectivity of drizzle  
 $Z_e$  = radar reflectivity  
 $Z_e^{max}$  = maximum of radar reflectivity profile  
**ZSH** = zero-skewness-height

## Acknowledgments

We thank C. Acquistapace for technical support. We thank in particular the two anonymous reviewers for their constructive comments, which helped to improve the manuscript. This work was funded by the project *Energy Transitions and Climate Change* (<http://et-cc.uni-koeln.de/project.html>) of the *Excellence Initiative* of the University of Cologne by the German Research Foundation (DFG) under Grant ZUK 81/1. Contributions by S. Kneifel were carried out within the Emmy-Noether Group OPTIMice funded by the DFG under Grant KN 1112/2-1. The data used in this study are available at the Institute for Geophysics and Meteorology of the University of Cologne. Observations originate from the DFG-funded Core Facility (JOYCE-CF) under DFG research grant LO 901/7-1. This project has received funding from the European Union's Horizon 2020 research and innovation program under grant agreement No 654109.

## References

- Acquistapace, C. (2016). Investigation of drizzle onset in liquid clouds using ground based active and passive remote sensing instruments (PhD thesis), Universität zu Köln.
- Atlas, D. (1954). The estimation of cloud parameters by radar. *Journal of Meteorology*, 11(4), 309–317. [https://doi.org/10.1175/1520-0469\(1954\)011<0309:TEOCPB>2.0.CO;2](https://doi.org/10.1175/1520-0469(1954)011<0309:TEOCPB>2.0.CO;2)
- Beard, K. V. (1976). Terminal velocity adjustment for cloud and precipitation drops aloft. *Journal of the Atmospheric Sciences*, 33(5), 851–864. [https://doi.org/10.1175/1520-0469\(1977\)034<1293:TVAFCA>2.0.CO;2](https://doi.org/10.1175/1520-0469(1977)034<1293:TVAFCA>2.0.CO;2)
- Borque, P., Luke, E., & Kollias, P. (2016). On the unified estimation of turbulence eddy dissipation rate using Doppler cloud radars and lidars. *Journal of Geophysical Research: Atmospheres*, 121, 5972–5989. <https://doi.org/10.1002/2015JD024543>
- Boucher, O., Randall, D., Artaxo, P., Bretherton, C., Feingold, G., Forster, P., et al. (2013). 7. Clouds and aerosols. In T. F. Stocker, et al. (Eds.), *Climate Change 2013: The Physical Science Basis, Contribution of Working Group I to the Fifth Assessment Report of the Intergovernmental Panel on Climate Change* (pp. 571–657). Cambridge, UK: Cambridge University Press. <https://doi.org/10.1017/CBO9781107415324.016>
- Dong, X., & Mace, G. G. (2003). Profiles of low-level stratus cloud microphysics deduced from ground-based measurements. *Journal of Atmospheric and Oceanic Technology*, 20(1), 42–53. [https://doi.org/10.1175/1520-0426\(2003\)020<0042:POLLSC>2.0.CO;2](https://doi.org/10.1175/1520-0426(2003)020<0042:POLLSC>2.0.CO;2)
- Doviak, R., Zrnić, D., & Sirmans, D. S. (1979). Doppler weather radar. *Proceedings of the IEEE*, 67, 1522–1553. [https://doi.org/10.1109/1100-1522\\$00.75](https://doi.org/10.1109/1100-1522$00.75)
- Fang, M., Albrecht, B. A., Ghate, V. P., & Kollias, P. (2014). Turbulence in continental stratocumulus, Part II: Eddy dissipation rates and large-eddy coherent structures. *Boundary-Layer Meteorology*, 150(3), 361–380. <https://doi.org/10.1007/s10546-013-9872-4>
- Felding, M. D., Chiu, J. C., Hogan, R. J., & Feingold, G. (2014). A novel ensemble method for retrieving properties of warm cloud in 3-D using ground-based scanning radar and zenith radiances. *Journal of Geophysical Research: Atmospheres*, 119, 10,912–10,930. <https://doi.org/10.1002/2014JD021742>
- Fox, N. I., & Illingworth, A. J. (1997). The retrieval of stratocumulus cloud properties by ground-based cloud radar. *Journal of Applied Meteorology*, 36(5), 485–492. [https://doi.org/10.1175/1520-0450\(1997\)036<0485:TROSCP>2.0.CO;2](https://doi.org/10.1175/1520-0450(1997)036<0485:TROSCP>2.0.CO;2)
- Franklin, C. N. (2008). A warm rain microphysics parameterization that includes the effect of turbulence. *Journal of the Atmospheric Sciences*, 65(6), 1795–1816. <https://doi.org/10.1175/2007JAS2556.1>
- Frisch, A. S., Fairall, C. W., & Snider, J. B. (1995). Measurement of stratus cloud and drizzle parameters in ASTEX with a Ka-band Doppler radar and a microwave radiometer. *Journal of the Atmospheric Sciences*, 52(16), 2788–2799. [https://doi.org/10.1175/1520-0469\(1995\)052<2788:MOSCAD>2.0.CO;2](https://doi.org/10.1175/1520-0469(1995)052<2788:MOSCAD>2.0.CO;2)
- Frisch, A. S., Feingold, G., Fairall, C. W., Uttal, T., & Snider, J. B. (1998). On cloud radar and microwave radiometer measurements of stratus cloud liquid water profiles. *Journal of Geophysical Research*, 103(18), 23,195–23,197. <https://doi.org/10.1029/1998JD01827509.00>
- Hogan, R. J., Gaussiat, N., & Illingworth, A. J. (2005). Stratocumulus liquid water content from dual-wavelength radar. *Journal of Atmospheric and Oceanic Technology*, 22(8), 1207–1218. <https://doi.org/10.1175/JTECH1768.1>
- Huang, D., Johnson, K., Liu, Y., & Wiscombe, W. (2009). High resolution retrieval of liquid water vertical distributions using collocated Ka-band and W-band cloud radars. *Geophysical Research Letters*, 36, L24807. <https://doi.org/10.1029/2009GL041364>
- Illingworth, A. J., Hogan, R. J., O'Connor, E. J., Bouniol, D., Brooks, M. E., Delanoë, J., et al. (2007). Cloudnet: Continuous evaluation of cloud profiles in seven operational models using ground-based observations. *Bulletin of the American Meteorological Society*, 88(6), 883–898. <https://doi.org/10.1175/BAMS-88-6-883>
- Khain, A., Pinsky, M., Magaritz, L., Krasnov, O., & Russchenberg, H. W. (2008). Combined observational and model investigations of the Z-LWC relationship in stratocumulus clouds. *Journal of Applied Meteorology and Climatology*, 47(2), 591–606. <https://doi.org/10.1175/2007JAMC1701.1>
- Khairoutdinov, M., & Kogan, Y. (2000). A new cloud physics parameterization in a large-eddy simulation model of marine stratocumulus. *Monthly Weather Review*, 128(1), 229–243. [https://doi.org/10.1175/1520-0493\(2000\)128<0229:ANCPPI>2.0.CO;2](https://doi.org/10.1175/1520-0493(2000)128<0229:ANCPPI>2.0.CO;2)
- Kogan, Y. L., Kogan, Z. N., & Mechem, D. B. (2007). Assessing the errors of microphysical retrievals based on Doppler radar parameters. *Journal of Hydrometeorology - Special Section*, 8, 665–677. <https://doi.org/10.1175/JHM603.1>

- Kollias, P., Rémillard, J., Luke, E., & Szyrmer, P. W. (2011). Cloud radar Doppler spectra in drizzling stratiform clouds: 1. Forward modeling and remote sensing applications. *Journal of Geophysical Research*, *116*, D13201. <https://doi.org/10.1029/2010JD015237>
- Kollias, P., Szyrmer, W., Rémillard, J., & Luke, E. (2011). Cloud radar Doppler spectra in drizzling stratiform clouds: 2. Observations and microphysical modeling of drizzle evolution. *Journal of Geophysical Research*, *116*, D13203. <https://doi.org/10.1029/2010JD015238>
- Küchler, N., Kneifel, S., Löhnert, U., Kollias, P., Czekala, H., & Rose, T. (2017). A W-band radar-radiometer system for accurate and continuous monitoring of clouds and precipitation. *Journal of Atmospheric and Oceanic Technology*, *34*(11), 2375–2392. <https://doi.org/10.1175/JTECH-D-17-0019.1>
- Li, S., & Min, Q. (2013). Retrievals of vertical profiles of stratus cloud properties from combined oxygen A-band and radar observations. *Journal of Geophysical Research: Atmospheres*, *118*, 769–778. <https://doi.org/10.1029/2012JD018282>
- Löhnert, U., Acquistapace, C., Ebell, K., Maahn, M., Barrera-Verdejo, M., Hirsiko, A., et al. (2015). JOYCE: Julich Observatory for Cloud Evolution. *Bulletin of the American Meteorological Society*, *96*(7), 1157–1174. <https://doi.org/10.1175/BAMS-D-14-00105.1>
- Löhnert, U., Crewell, S., Simmer, C., & Macke, A. (2001). Profiling cloud liquid water by combining active and passive microwave measurements with cloud model statistics. *Journal of Atmospheric and Oceanic Technology*, *18*, 1354–1366. [https://doi.org/10.1175/1520-0426\(2001\)018<1354:PCLWBC>2.0.CO;2](https://doi.org/10.1175/1520-0426(2001)018<1354:PCLWBC>2.0.CO;2)
- Long, A. B. (1974). *Journal of the Atmospheric Sciences*, *31*, 1040–1052. [https://doi.org/10.1175/1520-0469\(1974\)031<1040:STTDCE>2.0.CO;2](https://doi.org/10.1175/1520-0469(1974)031<1040:STTDCE>2.0.CO;2)
- Luke, E. P., & Kollias, P. (2013). Separating cloud and drizzle radar moments during precipitation onset using Doppler spectra. *Journal of Atmospheric and Oceanic Technology*, *30*(8), 1656–1671. <https://doi.org/10.1175/JTECH-D-11-00195.1>
- Maahn, M., Löhnert, U., Kollias, P., Jackson, R. C., & McFarquhar, G. M. (2015). Developing and evaluating ice cloud parameterizations for forward modeling of radar moments using in situ aircraft observations. *Journal of Atmospheric and Oceanic Technology*, *32*(5), 880–903. <https://doi.org/10.1175/JTECH-D-14-00112.1>
- Nicholls, S. (1987). A model of drizzle growth in warm, turbulent, stratiform clouds. *Quarterly Journal of the Royal Meteorological Society*, *113*(478), 1141–1170. <https://doi.org/10.1002/qj.49711347805>
- O'Connor, E. J., Hogan, R. J., & Illingworth, A. J. (2005). Retrieving stratocumulus drizzle parameters using Doppler radar and lidar. *Journal of Applied Meteorology and Climatology*, *44*(1), 14–27. <https://doi.org/10.1175/JAM-2181.1>
- Petty, G. W. (2006). *A First Course in Atmospheric Radiation* (2nd ed.). Madison, WI: Sundog Publishing.
- Pujol, O., Georgis, J. F., & Sauvageot, H. (2007). Influence of drizzle on Z-M relationships in warm clouds. *Atmospheric Research*, *86*(3-4), 297–314. <https://doi.org/10.1016/j.atmosres.2007.06.005>
- Rusli, S. P., Donovan, D. P., & Russchenberg, H. W. (2017). Simultaneous and synergistic profiling of cloud and drizzle properties using ground-based observations. *Atmospheric Measurement Techniques*, *10*(12), 4777–4803. <https://doi.org/10.5194/amt-10-4777-2017>
- Sauvageot, H., & Omar, J. (1987). Radar reflectivity of cumulus clouds. *Journal of Atmospheric and Oceanic Technology*, *4*(2), 264–272. [https://doi.org/10.1175/1520-0426\(1987\)004<0264:RROCC>2.0.CO;2](https://doi.org/10.1175/1520-0426(1987)004<0264:RROCC>2.0.CO;2)
- Seifert, A., Nuijens, L., & Stevens, B. (2010). Turbulence effects on warm-rain formation in precipitating shallow convection. *Quarterly Journal of the Royal Meteorological Society*, *136*(652), 1753–1762. <https://doi.org/10.1002/qj.684>
- Stevens, B., Lenschow, D. H., Vali, G., Gerber, H., Bandy, A., Blomquist, B., et al. (2003). Dynamics and Chemistry of Marine Stratocumulus - DYCOMS-II. *Bulletin of the American Meteorological Society*, *84*(5), 579–593+548. <https://doi.org/10.1175/BAMS-84-5-579>
- Tripoli, G. J., & Cotton, W. R. (1980). *Journal of Applied Meteorology*, *19*(9), 1037–1063. [https://doi.org/10.1175/1520-0450\(1980\)019<1037:ANIOSF>2.0.CO;2](https://doi.org/10.1175/1520-0450(1980)019<1037:ANIOSF>2.0.CO;2)
- Wang, J., & Geerts, B. (2003). Identifying drizzle within marine stratus with W-band radar reflectivity. *Atmospheric Research*, *69*(1-2), 1–27. <https://doi.org/10.1016/j.atmosres.2003.08.001>
- Wood, R. (2012). Stratocumulus clouds. *Monthly Weather Review*, *140*(8), 2373–2423. <https://doi.org/10.1175/MWR-D-11-00121.1>
- Xie, X., & Liu, X. (2009). Analytical three-moment autoconversion parameterization based on generalized gamma distribution. *Journal of Geophysical Research*, *114*, D17201. <https://doi.org/10.1029/2008JD011633>
- Zhao, C., Xie, S., Klein, S. A., Protat, A., Shupe, M. D., McFarlane, S. A., et al. (2012). Toward understanding of differences in current cloud retrievals of ARM ground-based measurements. *Journal of Geophysical Research*, *117*, D10206. <https://doi.org/10.1029/2011JD016792>

# Supporting Information for ”Revisiting liquid water content retrievals in warm stratified clouds: The modified Frisch”

N. K uchler,<sup>1</sup> S. Kneifel,<sup>1</sup> P. Kollias,<sup>2,1</sup> and U. L ohnert<sup>1</sup>

## Contents of this file

1. Text S1
2. Figures S1

---

Corresponding author: N. K uchler, Institute for Geophysics and Meteorology, University of Cologne, Pohligstrasse 3, 50969 Cologne, Germany. (nkuech@meteo.uni-koeln.de)

<sup>1</sup>Institute for Geophysics and Meteorology, University of Cologne, Cologne, Germany.

<sup>2</sup>School of Marine and Atmospheric Sciences, Stony Brook University, New York, USA.



**Introduction** The accuracy of ModFrisch depends on how accurate the zero-skewness-height can be determined. In the following an uncertainty estimate based on the model study will be discussed in more detail.

### Separating Drizzle and Cloud Mode Using Skewness

The existence of a transition zone where skewness turns from positive to negative and where drizzle mode reflectivity equals cloud mode reflectivity is illustrated in Fig. S1a showing the probability density function (PDF) of skewness values found where  $Z_d/Z_c = 1$ . The PDF has a bell shape and is centered around zero exhibiting a standard deviation of 0.3 and a slightly positive mean value of 0.1. Both have been observed in measurements by *Acquistapace et al.* [2017] using a radar setup similar to the simulations in this study. However, ModFrisch works vice versa, i.e. it looks for the ZSH where it assumes that  $Z_d/Z_c = 1$ . Figure S1b shows the PDF for logarithmic  $Z_d/Z_c$  at the ZSH for non-/low-drizzling, drizzling, and all profiles. All distributions have their modes around zero. The width of the distribution for drizzling cases (about 4 dB) is larger than for non-/low-drizzling cases indicating a larger uncertainty of the retrieval for drizzling cases. Furthermore, the distribution of drizzling cases is associated with a tail towards low  $Z_d/Z_c$  ratios caused by identifying the ZSH to close to cloud top where  $Z_d/Z_c < 1$ .

### References

Acquistapace, C., S. Kneifel, U. Löhnert, P. Kollias, M. Maahn, and M. R. M. Bauer-Pfunstein (2017), Optimizing observations of drizzle onset with millimeter-wavelength radars, *Atmospheric Measurement Techniques*, (May), doi: <https://doi.org/10.5194/amt-10-1783-2017>.

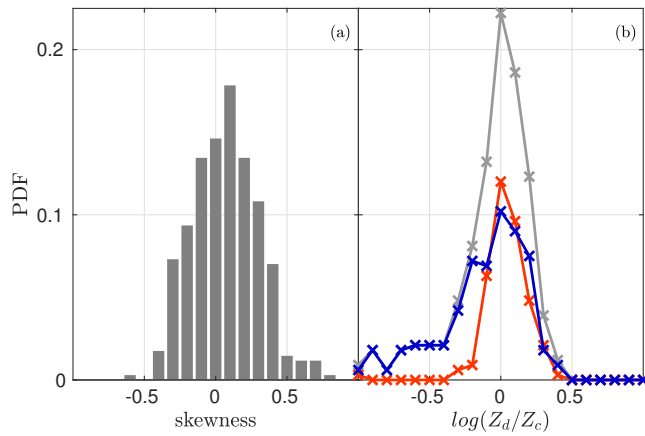


**Figure S1.** *a) Probability density function of Doppler spectrum skewness where the ratio between drizzle and cloud reflectivity equals one. b) Probability density function of logarithmic drizzle to cloud reflectivity ratio where skewness switches its sign from positive to negative. Gray: all cases. Blue: drizzling cases. Red: non-drizzling cases.*

## Chapter 6

# Discussion and Outlook

In this chapter, the main findings of [Study I](#), [Publication I](#), [Publication II](#), and [Publication III](#) are summarized and discussed. Moreover, an outlook is given based on the overall picture created by the work presented here.

### 6.1 Uncertainty Estimates of Energy System Investment Models

Energy system investment models (ESIM) optimize available renewable energy, demand and investment costs to predict the evolution of energy systems. Henckes et al. (2018b) show that ESIMs are sensitive to meteorological input data and exhibit a big spread of installed energy technologies if reasonable uncertainty estimates of the meteorological input data is provided. This is, to the authors' knowledge, the first time that the uncertainty of ESIMs is quantified based on the accuracy of the meteorological input data. The magnitude of the found model uncertainty implies that a comprehensive error analysis is indispensable before conclusion from ESIMs can be drawn.

To estimate the available solar energy, which is used by (Henckes et al., 2018b), correctly, the tilt angle of the photovoltaic (PV) panels must be known. The tilt angle is calculated using averaged surface albedo, direct and diffuse solar radiation data from the COSMO reanalysis (COSMO-REA6; Bollmeyer et al., 2015). Two different models, i.e. Klucher (1979) and Perez et al. (1990), are used to determine the optimal tilt angle for entire Germany. Figure 3.2 illustrates that the models differ on average by about  $4^\circ$ , which affects the total energy output by less than 1 % (see section 3.3). This error can be neglected when considering the uncertainty induced by the error due to direct solar radiation, being 23 %. The errors due to surface albedo and diffuse radiation have also negligible impacts on the available solar energy. All error estimates are based on the uncertainty estimates of radiation and surface albedo given

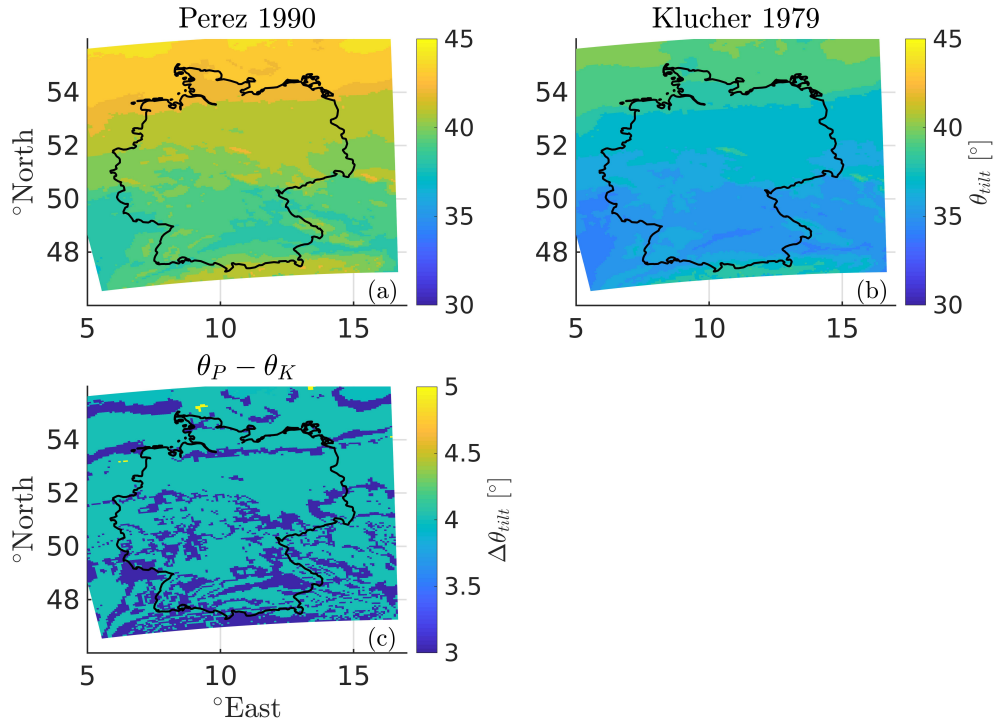


FIGURE 3.2: Optimal tilt angle for southerly oriented PV panels in Germany, determined using COSMO-REA6 radiation and surface albedo data with two different radiation models, i.e. PM (Perez 1990) and KM (Klucher 1979). Bottom left: Difference  $\Delta\theta$  between the two models' output angles  $\theta_P$  and  $\theta_K$  of PM and KM model, respectively. (repeated from page 35)

by Henckes et al. (2018b) (see table 3.1) and are converted into PV energy output. The PV energy output depends on the optimal tilt angle (Fig. 3.2), the total incoming solar radiation and the PV-efficiency that was assumed to be 0.1 (see section 3.3).

The study by Henckes et al. (2018b) and the analysis presented here point out that it is crucial to estimate the direct solar radiation correctly to provide accurate estimates of available solar energy. The latter is key for reliable prognoses of future energy systems. Therefore a comprehensive evaluation of models and cloud parameterizations, which are used in reanalyses, is necessary to decrease uncertainties and provide useful data for applications such as ESIMs.

## 6.2 New Opportunities for Remote Sensing of Clouds

[Publication I](#) presents a new *frequency modulated continuous wave* (FMCW) W-band radar-radiometer (JOYRAD-94) that is compared to a pulsed 35 GHz system (JOYRAD-35). Both systems are located at *Jülich Observatory for Cloud*

*Evolution - Central Facility (JOYCE-CF)*. The comparison shows good results implying that both instruments are well calibrated (see Fig. 6.2). It is found that the performance of JOYRAD-94 suffered from a degrading power chip that decreased the instrument's sensitivity by several dB. Yet, JOYRAD-94 is capable of detecting thin liquid clouds and has comparable sensitivity to JOYRAD-35, if the power chip is stable. The latter was replaced and since then, has been running without any evidence of degradation.

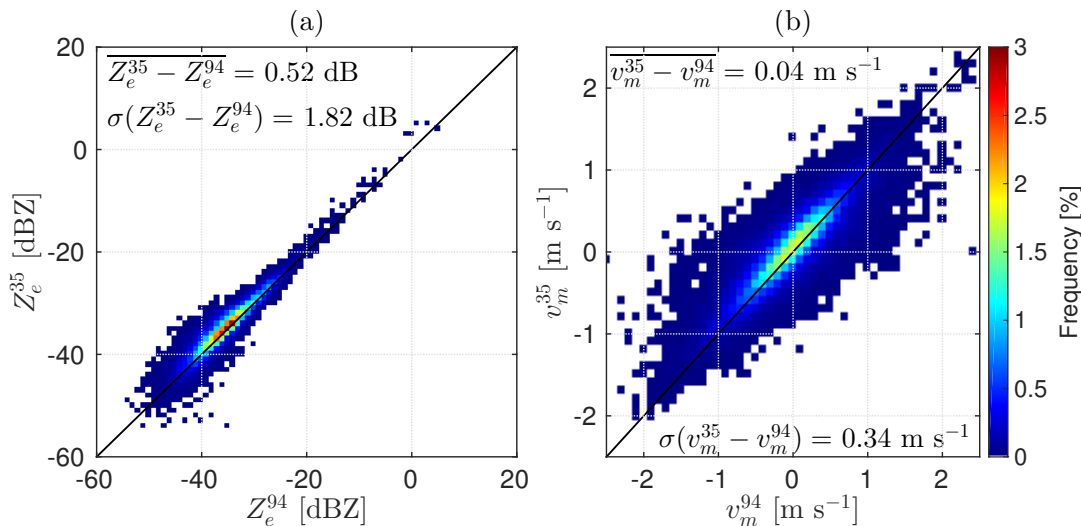


FIGURE 6.2: Scatterhistograms of (a) reflectivities and (b) mean Doppler velocities of JOYRAD-94 and JOYRAD-35, which were observed at cloud center of single-layer liquid clouds having a cloud base above 200 m. Source K uchler et al. (2017).

JOYRAD-94 can measure with high vertical resolution (5 m and smaller) which decreases the influence of turbulence on the Doppler spectrum. However, this implies a loss of sensitivity due to FMCW technology. Thus, users must weigh their decision whether high vertical resolution or high sensitivity should be accomplished. On the one hand, the sensitivity can be increased by longer averaging times, on the other hand, this decreases the temporal resolution. Thus, FMCW technology provides new opportunities but also requires trade-offs similar to those that appear when using pulsed systems.

A disadvantage of the instrument's design is the limited *intermediate frequency* (IF) range that requires to execute several chirp sequences consecutively to probe the vertical column until 12 km. This implies that each layer (corresponding to each sequence) is observed at slightly different times (see Fig. 4.1), which will be a problem if the entire column is of interest. Additionally, the different Doppler resolutions in each chirp sequence affect the data analysis, because higher spectral moments are statistical measures that

are dependent on the Doppler resolution. If the Doppler resolution changes, also the statistical properties of the spectral moments will change.

Furthermore, [Publication I](#) presents a new method to dealias Doppler spectra combining a radar with large unambiguous velocity range (also *Nyquist velocity*) and a radar with a small Nyquist velocity. The choice of the Nyquist velocities depends on the expected maximum Doppler velocity and the expected maximum spectral width that are observed. The latter determines the Nyquist range of the radar with large velocity range and the former the Nyquist range of the radar with small velocity range. If the spectral width spans the entire velocity range, the noise floor will not be detectable, hence, signal will be lost. A possible drawback of this method is that both instruments have to point always into the same direction, which requires perfect synchronization if both radars have scanning capability.

A novelty of JOYRAD-94 is that the passive and active components receive their signals over the same antenna, i.e. optimal beam match is accomplished. Although, the passive channel measures only at 89 GHz, *liquid water path* (LWP) with comparable accuracy to state-of-the-art instrumentation (Rose et al., 2005) can be achieved when the *integrated water vapor* (IWV) is known from an external source. [Publication II](#) shows that optimally matched beams are required to retrieve cloud properties with high temporal resolution. JOYRAD-94 provides new possibilities for cloud remote sensing; however, it is also associated with disadvantages, such as the limited IF range. Further technical development and improvement is needed to ensure reliable long-term data.

### 6.3 Retrieving Liquid Water Content of Warm Stratified Clouds

The retrieval of reliable LWC profiles implies that uncertainty sources must be characterized. These arise from measurement uncertainties (see [Publication I](#)), the measurement setup in case of synergetic profiling, and the retrieval itself. The latter two are discussed in the following.

### 6.3.1 How the Measurement Setup Affects Retrieval Uncertainties

[Publication II](#) presents a new methodology that helps to estimate retrieval uncertainties induced by combining co-located instruments. On the one hand, sensor synergy usually increases the degrees of freedom in the retrieval, on the other hand, the instruments might observe different scenes. Data from JOYRAD-94 is used, which has optimally matched beams (see [Publication I](#)), to create a reference two-dimensional *liquid water content* (LWC) cloud field in space. Thereby, a one-hour time series of radar and radiometer observables (*radar reflectivity*  $Z_e$  and LWP derived from radiometer *brightness temperatures* (BT)) and wind lidar measurements of a single-layer liquid cloud, which was observed at JOYCE-CF, serve as a reference.

In the next step, the reference cloud is used to calculate  $Z_e$ s and BTs for different beam widths. The distance between the instruments and their beam widths can now be arbitrarily changed to investigate the influence of displacement and sampling volume size on the retrieval. [Figure 6.3](#) illustrates that increasing sensor displacement affects the accuracy of the retrieved LWC much stronger than increasing the instruments' beam widths. Yet, if instruments are displaced to each other, a wider radiometer beam compensates partially the error due to displacement. At 20 m displacement an uncertainty of 10 % is found, which increases up to 30 % at 100 m. Finally, it is found that studying sharp cloud edges is not possible once the instruments are displaced by 10 m or more.

[Publication II](#) points out that a fundamental problem in synergetic ground-based remote sensing has been neglected in current research: retrievals can be strongly affected when combining data from instruments that are displaced by several meters. Note that the uncertainties shown in [Fig. 6.3](#) correspond to highly temporary resolved profiles. The uncertainty is expected to be much smaller when averaging over several seconds or minutes is applied.

The study does not aim to give a comprehensive analysis but introduces a new methodology that can be applied to investigate the expected uncertainties of any other synergetic retrievals. Next steps should be to investigate different cloud scenarios including different particle size distributions. The study could also be repeated using aircraft observations as reference, which would make the results less sensitive to the assumptions applied when creating the reference cloud. In addition to the errors introduced by sensor displacement, retrieval uncertainties should be quantified properly, e.g. as is

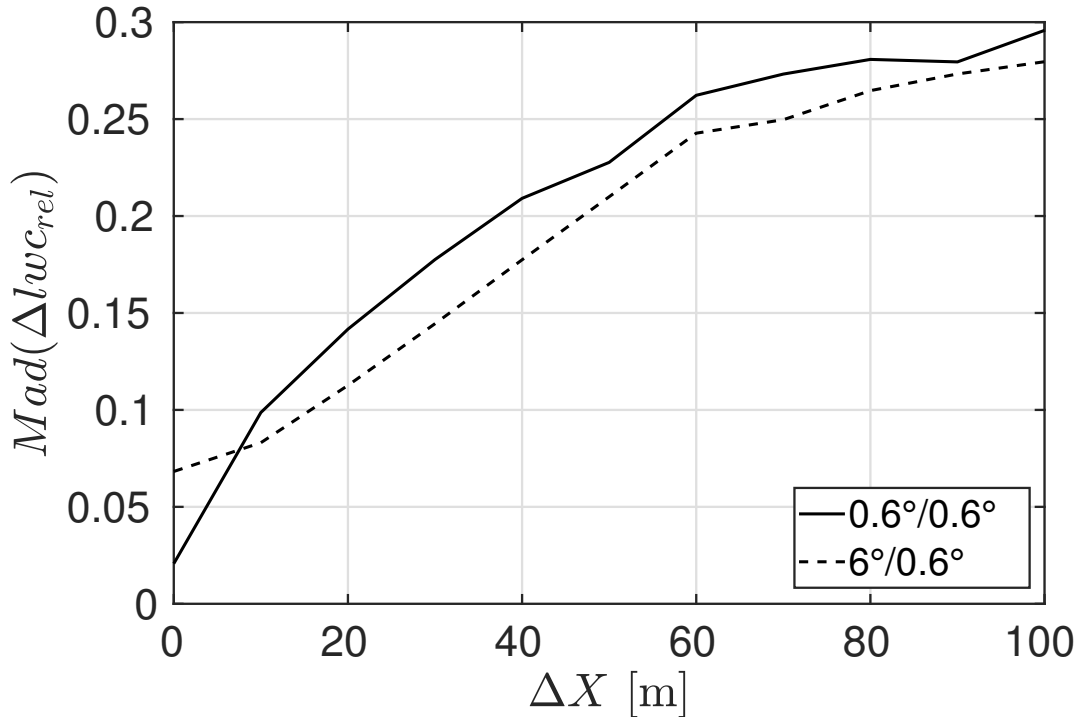


FIGURE 6.3: Median absolute deviation of relative liquid water content error ( $Mad(\Delta lwc_{rel})$ ) depending on sensor displacement  $\Delta X$  and different HPBW combinations (radiometer/radar). Source K uchler and L ohnert (2018).

proposed in [Publication III](#).

### 6.3.2 The Modified Frisch

[Publication III](#) presents a retrieval, *the modified Frisch* (modFrisch), that has the potential to determine LWC profiles under both non-drizzling and drizzling conditions by combining radar and radiometer observations. Retrieving LWC profiles under both drizzling and non-drizzling conditions has not yet been possible and represents an important research problem considering that Sc often contain drizzle (Stevens et al., 2003). The modFrisch is based on the retrieval by Frisch et al. (1998) (standFrisch) whose assumptions on the relation between  $Z_e$  and LWC are valid as long as drizzle is not present in the cloud. Once mature drizzle is present the standFrisch fails. However, Luke and Kollias (2013) showed that radar Doppler spectra can be used to identify drizzle development. Drizzle tends to tilt the Doppler spectrum, which can be quantified by calculating the spectrum's skewness. The modFrisch uses the skewness to identify trustworthy regions in the cloud where drizzle has no or at least a negligible influence on  $Z_e$ . In all other regions, the  $Z_e$  signal is reconstructed based on the shape of the non-contaminated  $Z_e$  signal and the



assumption of a linearly increasing LWC profile close to cloud base, which has been found to be generally valid in non- and weakly-drizzling Sc (Wood, 2012).

The performance of the modFrisch is evaluated by applying the retrieval to data output from a 1-D micro-physical model (MiMo; Kollias et al., 2011, modified) and to CLOUDNET observations (Illingworth et al., 2007) at JOYCE-CF. Figure 6.4 reveals that the modFrisch agrees well with the model in both drizzling and non-drizzling conditions, whereas the standFrisch does not produce reasonable results once drizzle is present. The model study shows that the retrieval uncertainty can be decreased by a factor of four, being on average smaller than 20 % for any amount of drizzle loading. Comparing the standFrisch and the modFrisch using data from CLOUDNET indicates a significant improvement of the quality of the LWC profile under drizzling conditions. Although, a reference is missing and therefore a final statement on the absolute accuracy cannot be made, the shape of the profiles under drizzling conditions look very similar to the profiles found in the model study.

**Publication III** suggests that the retrieval of LWC under drizzling conditions can be conducted in a robust and reliable way. So far, separate retrievals for drizzling and non-drizzling conditions are necessary (Khain et al., 2008) or explicit assumptions on certain shapes of drizzle and cloud PSD must be made (Rusli, Donovan, and Russchenberg, 2017). Although, there are studies showing that they can retrieve drizzle and cloud LWC simultaneously, they rarely provide statistically robust results as done by Löhnert et al. (2001); rather they are based on case studies (e.g. Rusli, Donovan, and Russchenberg, 2017).

The main weaknesses of **Publication III** are the lack of reliable observational references and the difficulty to determine trustworthy regions in the cloud based on skewness measurements. The latter is very sensitive to instrument noise and turbulence, which remains a big challenge to be solved. Nevertheless, considering that most LWC retrievals in comprehensive observatories are based on Frisch et al. (1998) or his previous work Frisch, Fairall, and Snider (1995) (Zhao et al., 2012), implies that the community misses a lot of data due to the frequent abundance of drizzling clouds (Stevens et al., 2003). Thus, the study is of great importance and provides a good fundament to build on.

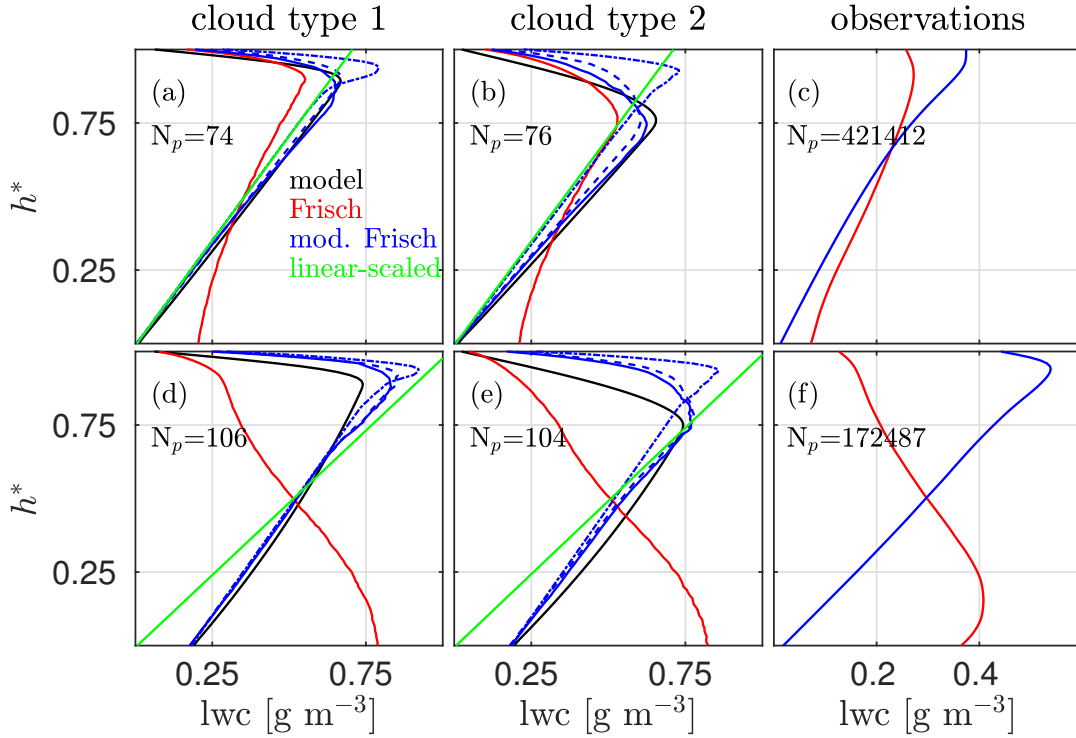


FIGURE 6.4: a) Comparison (74 profiles) between MiMo mean profiles (black) and several *LWC* retrievals for model cloud type 1 and no/low drizzling cases: the linear-scaled method (green), the standFrisch (red), and the modFrisch (blue; under low (solid), medium (dashed), and high (dotted-dashed) conditions). b) Like a) but for cloud type 2. c) standFrisch and modFrisch applied to observations of non-drizzling single-layer liquid cloud classified by CLOUDNET (Illingworth et al., 2007). d) Like a) but for drizzling cases. e) Like b) but for drizzling cases. f) like c) but for drizzling cases. Source K uchler et al. (2018).

## 6.4 The Big Picture and Future Visions

Climate change and its consequences for our lives demand shifts of our mindsets, lifestyles, and a more efficient and sustainable use of resources. The need for renewable energy sources is undoubtedly if we want to achieve the goals of the *Paris Agreement* (UNFCCC, 2015), i.e. to reduce CO<sub>2</sub>-emissions to zero by 2050 (Rockstr m et al., 2017). The integration of renewables into our current energy systems is constrained by their availabilities and fluctuations, energy demand, investment costs and political decisions such as reducing CO<sub>2</sub>-emission by 90 % compared to 1990 by 2050 in Germany. ES-IMs are an important tool to estimate how future energy systems will and should look like while considering these constraining parameters. However,

before drawing conclusions from results obtained by ESIMs, their uncertainties must be quantified. Chapter 3 shows that reanalysis data (COSMO-REA6) can be used to quantify the uncertainties of ESIMs by determining error sources in the meteorological input data, which is used to estimate the amount of available renewable energy. Moreover, it is shown that the major uncertainty source of available solar energy, used as input by ESIMs, is the direct solar radiation. Chapter 3 and the publication by Henckes et al. (2018b) represent a first step of a comprehensive error analysis estimating uncertainties of wind and solar radiation, affecting the predicted evolution of ESIMs, in reanalysis data. However, two questions were not discussed: how large are the uncertainties of other input parameters from ESIMs (e.g. demand and political decisions) and which processes cause uncertainties in reanalysis data? The latter is directly linked to meteorological observations that can be used to evaluate models and parameterizations in reanalyses; especially, predicting clouds and their interaction with solar radiation remains a major uncertainty source.

Accurate evaluations require accurate observations and the knowledge of measurement uncertainties. How physical properties of clouds, in particular stratocumulus clouds (Sc) that strongly affect the incoming solar radiation, can be quantified accurately by observations and which errors are associated with them is discussed in chapters 4 and 5. Chapter 4 (including Publication I and an additional analysis) introduces a radar-radiometer (JOYRAD-94) that, on the one hand, can provide long-term observations of cloud properties such as LWC. On the other hand, it is shown that there is further potential for technical development such as enabling the simultaneous probing of all range gates by JOYRAD-94 and improving the data acquisition and processing of radar Doppler spectra. Publication II investigates the uncertainties in synergetic LWC retrieval that arise from sensor displacement. The results show that the accuracy of a temporally highly-resolved LWC retrieval is strongly degraded by sensor displacement. Thus, to ensure accurate observations and to be able to evaluate models with increasing temporal and spatial resolutions, uncertainties caused by sensor displacement must be well quantified and/or displacement should be minimized. The findings of Publication II are based on a case study, a specific instrument combination and a specific retrieval. Therefore further investigations are needed to characterize uncertainties for various cloud conditions (e.g. drizzling or non-drizzling), instrument combinations and retrieval algorithms. Moreover, it should be investigated if sensor displacement impedes the possibility to observe small

scale processes such as autoconversion and rain production. [Publication III](#) presents a retrieval algorithm (ModFrisch) that is able to determine LWC under drizzling and non-drizzling conditions increasing the accuracy of LWC retrieval of  $Sc$ . Although ModFrisch can reconstruct the total LWC in  $Sc$ , it is not able to separate drizzle and cloud LWC, which is necessary to accurately observe small scale processes such as rain-production. Separating drizzle and cloud LWC based on ModFrisch is currently under investigation. To improve ModFrisch, the detection of drizzling and non-drizzling regions in the cloud can be further improved, for example by adding further criteria such as done by [Acquistapace \(2016\)](#).

To conclude: increasing knowledge, ignorance and complexity of our environment with its physical, social, political and economic processes and mechanisms require both specific and interdisciplinary research to solve the puzzle, or at least that part of the puzzle, which is currently most important for us, human beings, to understand and sustain our surroundings and ourselves on this planet, the Earth (Fig. [6.5](#)).

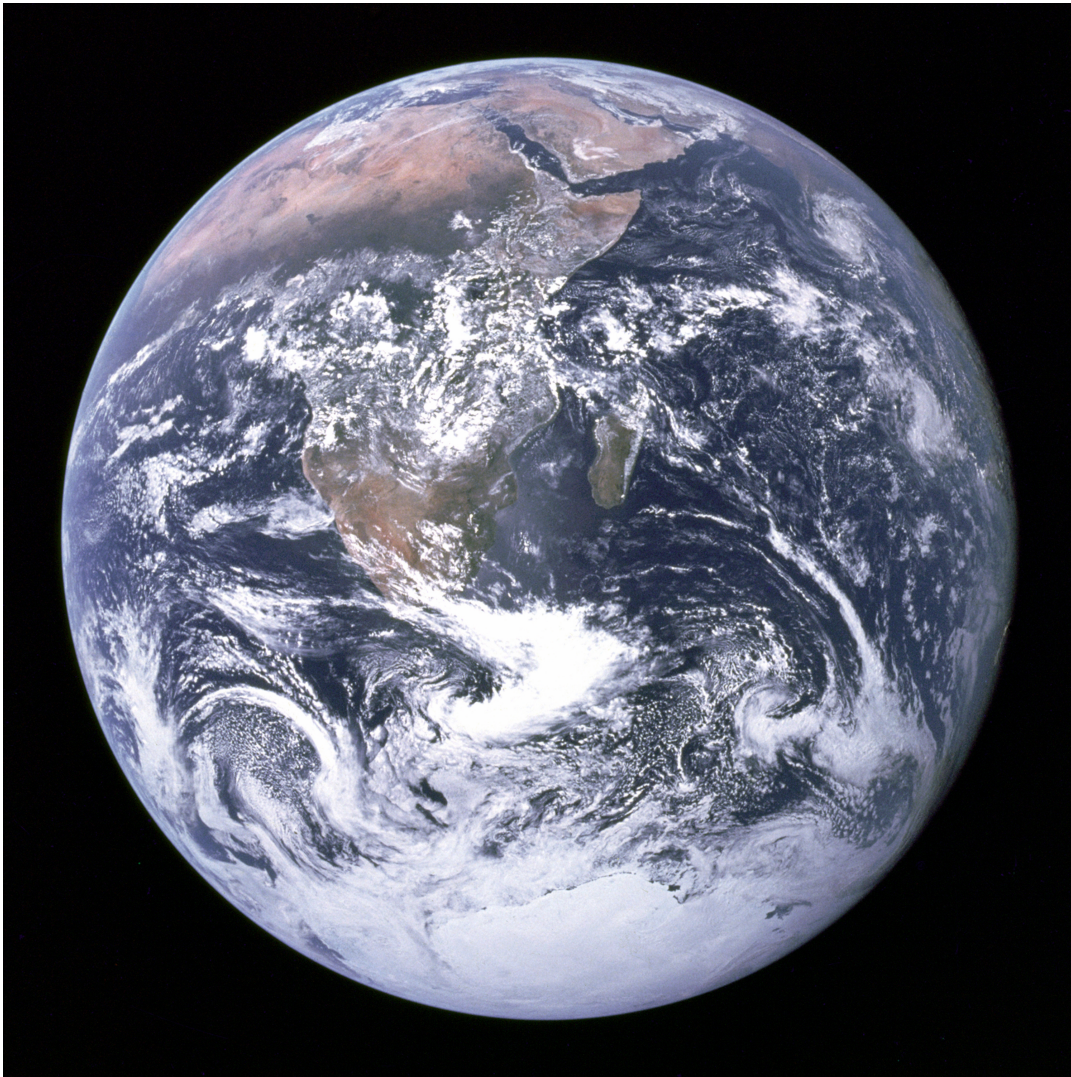


FIGURE 6.5: The Earth. Source: NASA/Apollo 17 crew; taken by either Harrison Schmitt or Ron Evans - [Link](#).



## Appendix A

# Eigene Beteiligung an Veröffentlichungen

### Publication I

N. Kuchler et al. (2017). "A W-Band Radar–Radiometer System for Accurate and Continuous Monitoring of Clouds and Precipitation". In: *Journal of Atmospheric and Oceanic Technology* 34.11, pp. 2375–2392. ISSN: 0739-0572. DOI: [10.1175/JTECH-D-17-0019.1](https://doi.org/10.1175/JTECH-D-17-0019.1). URL: <http://journals.ametsoc.org/doi/10.1175/JTECH-D-17-0019.1>

Als Erstautor habe ich den gesamten Text verfasst und alle Abbildungen außer Abbildung 9 selbst erstellt. Der Text in Kapitel 2 und 3, sowie Abbildung 2 wurden mit Unterstützung von *H. Czekala* und *T. Rose* erstellt. Abbildung 9 wurde von *U. Löhnert* erstellt. *S. Kneifel*, *P. Kollias* und *U. Löhnert* trugen bei regelmäßigen Treffen zur Interpretation der Ergebnisse und zur Bestimmung des weiteren Vorgehens bei.

### Publication II

N. Kuchler and U. Löhnert (2018). "Radar-radiometer based liquid water content retrievals of warm low-level clouds: how the measurement setup affects retrieval uncertainties". In: *IEEE Journal of Selected Topics in Applied Earth Observations and Remote Sensing* under review

Die gesamte Studie habe ich selbst erstellt. *U. Löhnert* trug bei regelmäßigen Treffen zur Interpretation der Ergebnisse und zur Bestimmung des weiteren Vorgehens bei.

## Publication III

N. Küchler et al. (2018). "Revisiting liquid water content retrievals in warm stratified clouds: The modified Frisch". In: *Geophysical Research Letters* 45.17. DOI: <https://doi.org/10.1029/2018GL079845>

Text und Abbildungen wurden von mir erstellt. In intensiver Zusammenarbeit mit *P. Kollias* wurde die Idee für das verbesserte Verfahren entwickelt. *S. Kneifel* und *U. Löhnert* trugen bei regelmäßigen Treffen zur Interpretation der Ergebnisse und zur Bestimmung des weiteren Vorgehens bei.



# List of Figures

|     |  |    |
|-----|--|----|
| 1.1 | "(a) Annual mean coverage of stratocumulus clouds. Data are from the combined land–ocean cloud atlas database (Hahn and Warren 2007)." (Wood, 2012) . . . . .  | 10 |
| 1.2 | Schematic overview of the studies. Key publications are the studies in green motivated by the broader context of the project <i>Energy Transitions and Climate Change</i> . . . . .  | 14 |
| 2.1 | "Microwave extinction due to water vapor, oxygen, and typical cloud liquid water content of $0.2 \text{ g m}^{-3}$ at 895 hPa. [...]" Source Löhnert and Crewell (2003). . . . .   | 21 |
| 2.2 | Schematic illustration of the receiver chain of a direct detecting radiometer. Source (Küchler et al., 2016). . . . .  | 22 |
| 2.3 | Example of a sawtooth chirp $T_c$ . Transmitted frequencies over B (black line). Received frequencies delayed by $\Delta t$ (gray line). The backscattering particle's distance and velocity determine $f_{IF}$ . The sampling time $T_{samp}$ is determined by the maximum distance that is sampled. . . . .  | 24 |
| 2.4 | Radar Doppler spectrum (solid line), measured by a 94 GHz radar (Publication I), showing the spectral reflectivity $Z_e(v_d)$ depending on the Doppler velocity $v_d$ . The dashed horizontal line indicates the mean noise floor that is subtracted from the signal before spectral moments are calculated. The circle indicates the mean Doppler velocity, the double-arrow the spectral width, and the dotted and tilted line the negative skewness. Note that Doppler velocities smaller than zero correspond to particles moving towards the radar. This notation is used in Publication I. However, some data sets are based on a converse notation, such as the data set used in Publication III. . . . . | 28 |

- 3.1 (a) Estimated contributions to the total energy generation in Germany of by different technologies for the 90%-scenario. CCGT, OCGT and PV are abbreviations for combined cycle gas turbine, open cycle gas turbine and photovoltaic, respectively. Runoff represents water power. The results are obtained from the Renewable Power System Model (RPSM) by Henckes et al. (2018b) that is coupled with the Renewable Energy Output Model (Henckes et al., 2018a) whose meteorological input data is based on 20 years averaged reanalysis data. (b) Difference between RPSM output based on meteorological input data from (a) perturbed by its uncertainty and the results shown in (a). The perturbed case represents an underestimation of available wind and solar energy. Source Henckes et al. (2018b). . . . . 33
- 3.2 Optimal tilt angle for southerly oriented PV panels in Germany determined using COSMO-REA6 radiation and surface albedo data with two different radiation models: (a) PM (Perez 1990) and (b) KM (Klucher 1979). (c) Difference  $\Delta\theta$  between the to models' output angles  $\theta_P$  and  $\theta_K$  of PM and KM model, respectively. . . . . 35
- 3.3 (a) Produced energy, depending on the tilt angle and the radiation model (KM and PM), by a PV system of  $1 \text{ m}^2$  area with an efficiency of 10 %. (b) Sensitivity of energy production in  $\text{kWh y}^{-1} \text{ deg}^{-1}$  depending on the tilt angle. . . . . 37
- 4.1 Occurrence frequency of the difference between the maximum reflectivities of JOYRAD-35 and JOYRAD-94 ( $\Delta\max(Z_e) = \max(Z_e^{35}) - \max(Z_e^{94})$ ) that were observed during a time window of 30 seconds versus the time difference  $\Delta t$  when the two instruments detected the maximum. Only single-layer ice-clouds are considered. (a) For cloud base heights (CBH) between 400 and 1200 m. (b) For CBH between 1200 and 3000 m. (c) For CBH between 3000 and 12000 m. Note that the color scale is different in (a). . . . . 60

|     |   |    |
|-----|---|----|
| 4.2 | (a) Results of the deliasing procedure of AddProc. Wrongly dealiased columns are visible at time indexes 630 and 894. (b) Absolute mean values of $v_m$ ( $\text{m s}^{-1}$ ) differences of two timely adjacent bins ( $ \overline{dv} $ ( $\text{m s}^{-1}$ ); blue). The peak noise level (yellow) of this signal was determined using Hildebrand and Sekhon, 1974. All values above the peak noise (red circles) are identified and corrected by AddProc. (c) Corrected velocity field of (a). . . . .  | 61 |
| 6.2 | Scatterhistograms of (a) reflectivities and (b) mean Doppler velocities of JOYRAD-94 and JOYRAD-35, which were observed at cloud center of single-layer liquid clouds having a cloud base above 200 m. Source K uchler et al. (2017). . . . .   | 85 |
| 6.3 | Median absolute deviation of relative liquid water content error ( $Mad(\Delta lwc_{rel})$ ) depending on sensor displacement $\Delta X$ and different HPBW combinations (radiometer/radar). Source K uchler and L ohnert (2018). . . . .   | 88 |
| 6.4 | a) Comparison (74 profiles) between MiMo mean profiles (black) and several LWC retrievals for model cloud type 1 and no/low drizzling cases: the linear-scaled method (green), the standFrisch (red), and the modFrisch (blue; under low (solid), medium (dashed), and high (dotted-dashed) conditions). b) Like a) but for cloud type 2. c) standFrisch and modFrisch applied to observations of non-drizzling single-layer liquid cloud classified by CLOUDNET (Illingworth et al., 2007). d) Like a) but for drizzling cases. e) Like b) but for drizzling cases. f) like c) but for drizzling cases. Source K uchler et al. (2018). . . . . | 90 |
| 6.5 | The Earth. Source: NASA/Apollo 17 crew; taken by either Harrison Schmitt or Ron Evans - Link. . . . .   | 93 |



# List of Abbreviations

|                   |  |
|-------------------|--|
| <b>AddProc</b>    | <b>Additional Data Processing</b>                                |
| <b>BT</b>         | <b>Brightness Temperature</b>                                    |
| <b>CBH</b>        | <b>Cloud Base Height</b>   |
| <b>CCN</b>        | <b>Cloud Condensation Nuclei</b>                                 |
| <b>COSMO-REA6</b> | <b>COSMO-Reanalysis with 6 km horizontal resolution</b>          |
| <b>CWT</b>        | <b>Circulation Weather Type</b>                                  |
| <b>dB</b>         | <b>Decibel</b>   |
| <b>ESIM</b>       | <b>Energy-System Investment Model</b>                            |
| <b>ET-CC</b>      | <b>Energy Transitions and Climate Change</b>                     |
| <b>FFT</b>        | <b>Fast Fourier Transform</b>                                    |
| <b>FMCW</b>       | <b>Frequency Modulated Continuous Wave</b>                       |
| <b>IF</b>         | <b>Intermediate Frequency</b>                                    |
| <b>IWV</b>        | <b>Integrated Water Vapor</b>                                    |
| <b>JOYCE-CF</b>   | <b>Jülich Observatory for Cloud Evolution - Central Facility</b> |
| <b>JOYRAD-35</b>  | <b>JOYCE Radar - 35 GHz</b>                                      |
| <b>JOYRAD-94</b>  | <b>JOYCE Radar - 94 GHz</b>                                      |
| <b>KM</b>         | <b>Klucher Model</b>   |
| <b>LES</b>        | <b>Large Eddy Simulation</b>                                     |
| <b>Lidar</b>      | <b>Light Detection and Ranging</b>                               |
| <b>LW</b>         | <b>Long Wave</b>   |
| <b>LWC</b>        | <b>Liquid Water Content</b>                                      |
| <b>LWP</b>        | <b>Liquid Water Path</b>   |
| <b>modFrisch</b>  | <b>modified Frisch retrieval</b>                                 |
| <b>MiMo</b>       | <b>1-D Steady State Bin-Micro-Physical Model</b>                 |
| <b>MWR</b>        | <b>Microwave Radiometer</b>                                      |
| <b>PAMTRA</b>     | <b>Passive and Active Microwave Radiative Transfer Model</b>     |
| <b>PM</b>         | <b>Perez Model</b>   |
| <b>PSD</b>        | <b>Particle Size Distribution</b>                                |
| <b>PV</b>         | <b>Photovoltaic</b>  |
| <b>Radar</b>      | <b>Radiation Detection and Ranging</b>                           |
| <b>RTM</b>        | <b>Radiative Transfer Model</b>                                  |
| <b>Sc</b>         | <b>Stratocumulus cloud</b>                                       |

**SDG** Sustainable Development Goals  
**standFrisch** **standard Frisch** retrieval

# List of Symbols

|                   |  |  |
|-------------------|--|--|
| $A$               | surface albedo                                 |  |
| $B$               | bandwidth                                      | Hz                                     |
| $B^*$             | effective bandwidth                            | Hz                                     |
| $BT$              | brightness temperature                         | K                                      |
| $c$               | speed of light                                 | $\text{m s}^{-1}$                      |
| $g$               | gain   | $\text{W V}^{-1}$                      |
| $\Delta g$        | gain fluctuation                               | $\text{W V}^{-1}$                      |
| $D$               | diameter                                       | m                                      |
| $ \overline{dv} $ | the absolute column-means of $v_m$ differences | $\text{m s}^{-1}$                      |
| $E_{opt}$         | energy at optimal tilt                         | $\text{kWh y}^{-1}$                    |
| $\Delta E$        | energy difference                              | $\text{kWh y}^{-1}$                    |
| $f_0$             | sampling frequency                             | Hz                                     |
| $f_d$             | Doppler frequency                              | Hz                                     |
| $f_{IF}$          | intermediate frequency                         | Hz                                     |
| $f_{samp}$        | chirp sampling frequency                       | Hz                                     |
| $h$               | Planck's constant                              | $6.63 \cdot 10^{-34} \text{ J s}$      |
| IWV               | integrated water vapor                         | $\text{kg m}^{-2}$                     |
| $K_w$             | dielectric parameter                           |  |
| $k_B$             | Boltzmann's constant                           | $1.38 \cdot 10^{-23} \text{ J K}^{-1}$ |
| LWC               | liquid water content                           | $\text{kg m}^{-2}$                     |
| LWP               | liquid water path                              | $\text{kg m}^{-2}$                     |
| $M_{fft}$         | number of sampling points of second FFT        |  |
| $n(D)$            | particle size distribution                     | $\text{m}^{-4}$                        |
| $N$               | number concentration                           | $\text{m}^{-3}$                        |
| $N_{fft}$         | number of sampling points of first FFT         |  |
| $N_l$             | number of layers                               |  |
| $P_N$             | instrument noise power                         | W                                      |
| $P_r$             | detected power                                 | W                                      |
| $P_{sc}$          | power of observed scene                        | W                                      |
| $R$               | radar range                                    | m                                      |
| $\delta R$        | radar range resolution                         | m                                      |

|                 |                              |                                 |
|-----------------|------------------------------|---------------------------------|
| $s_d$           | mixed detector signal        | W                               |
| $s_t$           | transmitted signal           | W                               |
| $s_r$           | received signal              | W                               |
| $S_{dir}$       | direct solar radiation       | W m <sup>-2</sup>               |
| $S_{dif}$       | diffuse solar radiation      | W m <sup>-2</sup>               |
| $S_{ref}$       | reflected solar radiation    | W m <sup>-2</sup>               |
| $S_{tot}$       | total solar radiation        | W m <sup>-2</sup>               |
| $Sk$            | Doppler spectrum skewness    |                                 |
| $\theta_{tilt}$ | tile angle                   | °                               |
| $\Delta t$      | signal delay time            | s                               |
| $T_{bin}$       | bin sample time              | s                               |
| $T_c$           | chirp duration               | s                               |
| $T_{samp}$      | effective sampling time      | s                               |
| $v_d$           | Doppler velocity             | m s <sup>-1</sup>               |
| $v_m$           | mean Doppler velocity        | m s <sup>-1</sup>               |
| $v_N$           | Nyquist velocity             | m s <sup>-1</sup>               |
| $Z_e$           | radar reflectivity           | mm <sup>6</sup> m <sup>-3</sup> |
| $\eta$          | radar reflectivity factor    | m <sup>-1</sup>                 |
| $\lambda$       | wavelength                   | m                               |
| $\nu$           | receiver bandwidth           | Hz                              |
| $\pi$           | Archimedes' constant         |                                 |
| $\sigma_B$      | backscattering cross-section | m <sup>2</sup>                  |
| $\sigma_v$      | Doppler spectrum width       | m s <sup>-1</sup>               |
| $\tau$          | integration time             | s                               |



# Bibliography

- Acquistapace, C. (2016). "Investigation of Drizzle Onset in Liquid Clouds Using Ground Based Active and Passive Remote Sensing Instruments". PhD thesis. Universität zu Köln.
- Acquistapace, C. et al. (2017). "Optimizing observations of drizzle onset with millimeter-wavelength radars". In: *Atmospheric Measurement Techniques* 10.5, pp. 1783–1802. DOI: [10.5194/amt-10-1783-2017](https://doi.org/10.5194/amt-10-1783-2017).
- Armstrong, E. H. (1921). "A New System of Short Wave Amplification". In: *Proceedings of the Institute of Radio Engineers* 9.1, pp. 3–11. ISSN: 0731-5996. DOI: [10.1109/JRPROC.1921.220092](https://doi.org/10.1109/JRPROC.1921.220092).
- Atlas, D. (1964). "Advances in Radar Meteorology". In: ed. by H E Landsberg and J Van Mieghem. Vol. 10. *Advances in Geophysics*. Elsevier, pp. 317–478. DOI: [https://doi.org/10.1016/S0065-2687\(08\)60009-6](https://doi.org/10.1016/S0065-2687(08)60009-6). URL: <http://www.sciencedirect.com/science/article/pii/S0065268708600096>.
- Atlas, David (1954). "THE ESTIMATION OF CLOUD PARAMETERS BY RADAR". In: *Journal of Meteorology* 11.4, pp. 309–317. DOI: [http://dx.doi.org/10.1175/1520-0469\(1954\)011<0309:TEOCPB>2.0.CO;2](http://dx.doi.org/10.1175/1520-0469(1954)011<0309:TEOCPB>2.0.CO;2).
- Babkovskaia, N. et al. (2015). "A study of aerosol activation at the cloud edge with high resolution numerical simulations". In: *Atmospheric Research* 153, pp. 49–58. ISSN: 01698095. DOI: [10.1016/j.atmosres.2014.07.017](https://doi.org/10.1016/j.atmosres.2014.07.017). URL: <http://www.sciencedirect.com/science/article/pii/S0169809514002804>.
- Baedi, R. J. P. et al. (2000). "Estimating effective radius and liquid water content from radar and lidar based on the CLARE98 data-set". In: *Physics and Chemistry of the Earth, Part B: Hydrology, Oceans and Atmosphere* 25.10-12, pp. 1057–1062. ISSN: 14641909. DOI: [10.1016/S1464-1909\(00\)00152-0](https://doi.org/10.1016/S1464-1909(00)00152-0).
- Beard, K. V. and H. T. Ochs (1993). "Warm-Rain Initiation: An Overview of Microphysical Mechanisms". In: *Journal of Applied Meteorology* 32.4, pp. 608–625. DOI: [10.1175/1520-0450\(1993\)032<0608:WRIA00>2.0.CO;2](https://doi.org/10.1175/1520-0450(1993)032<0608:WRIA00>2.0.CO;2).
- Bengtsson, L., S. Hagemann, and K. I. Hodges (2004). "Can climate trends be calculated from reanalysis data?" In: *Journal of Geophysical Research: Atmospheres* 109.11, pp. 1–8. ISSN: 01480227. DOI: [10.1029/2004JD004536](https://doi.org/10.1029/2004JD004536).

- Bennett, A. et al. (2009). "Observations from the UK Met Office 94 GHz FMCW cloud radar". In: *Proceedings of the 8th International Symposium on Tropospheric Profiling*. October, pp. 2–5. ISBN: 9789069602332. URL: <ftp://ftp.meteoswiss.ch/outgoing/dcr/ISTP/ABSTRACTS/data/1657328.pdf>.
- Bergman, J. W. and M. L. Salby (1996). "Diurnal Variations of Cloud Cover and Their Relationship to Climatological Conditions". In: *Journal of Climate* 9.11, pp. 2802–2820. DOI: [10.1175/1520-0442\(1996\)009<2802:DVOCCA>2.0.CO;2](https://doi.org/10.1175/1520-0442(1996)009<2802:DVOCCA>2.0.CO;2).
- BGR (2017). *BGR Energiestudie 2017 - Daten und Entwicklung der deutschen und globalen Energieversorgung*. Tech. rep. Hannover: Bundesanstalt für Geowissenschaften und Rohstoffe (BGR).
- Bogenschutz, P. A. and S. K. Krueger (2013). "A simplified PDF parameterization of subgrid-scale clouds and turbulence for cloud-resolving models". In: *Journal of Advances in Modeling Earth Systems* 5.2, pp. 195–211. ISSN: 19422466. DOI: [10.1002/jame.20018](https://doi.org/10.1002/jame.20018).
- Bollmeyer, C. et al. (2015). "Towards a high-resolution regional reanalysis for the european CORDEX domain". In: *Quarterly Journal of the Royal Meteorological Society* 141.686, pp. 1–15. ISSN: 1477870X. DOI: [10.1002/qj.2486](https://doi.org/10.1002/qj.2486).
- Cadeddu, M. P. et al. (2017). "Microwave Passive Ground-Based Retrievals of Cloud and Rain Liquid Water Path in Drizzling Clouds: Challenges and Possibilities". In: *IEEE Transactions on Geoscience and Remote Sensing* 55.11, pp. 6468–6481. ISSN: 0196-2892. DOI: [10.1109/TGRS.2017.2728699](https://doi.org/10.1109/TGRS.2017.2728699).
- Cai, W. et al. (2014). "Increasing frequency of extreme El Niño events due to greenhouse warming". In: *Nature Climate Change* 4.2, pp. 111–116. ISSN: 1758678X. DOI: [10.1038/nclimate2100](https://doi.org/10.1038/nclimate2100). URL: <http://dx.doi.org/10.1038/nclimate2100>.
- Chen, H. et al. (2018). "Vertically resolved concentration and liquid water content of atmospheric nanoparticles at the US DOE Southern Great Plains site". In: *Atmospheric Chemistry and Physics* 18.1, pp. 311–326. ISSN: 16807324. DOI: [10.5194/acp-18-311-2018](https://doi.org/10.5194/acp-18-311-2018).
- Clothiaux, E E et al. (1995). "An Evaluation of a 94-GHz Radar for Remote Sensing of Cloud Properties". In: *Journal of Atmospheric and Oceanic Technology* 12.2, pp. 201–229. ISSN: 0739-0572. DOI: [10.1175/1520-0426\(1995\)012<0201:AEOAGR>2.0.CO;2](https://doi.org/10.1175/1520-0426(1995)012<0201:AEOAGR>2.0.CO;2).
- Clough, S. A. et al. (2005). "Atmospheric radiative transfer modeling: A summary of the AER codes". In: *Journal of Quantitative Spectroscopy and Radiative Transfer* 91.2, pp. 233–244. ISSN: 00224073. DOI: [10.1016/j.jqsrt.2004.05.058](https://doi.org/10.1016/j.jqsrt.2004.05.058).

- Cooley, J. W. and J. W. Tukey (1965). "An Algorithm for the Machine Calculation of Complex Fourier Series". In: *Mathematics of Computation* 19.90, pp. 297–301. ISSN: 00255718, 10886842. URL: <http://www.jstor.org/stable/2003354>.
- Crewell, S. et al. (2001). "Microwave Radiometer for Cloud Carthography: A 22-channel ground-based microwave radiometer for atmospheric research". In: *Radio Science* 36.4, pp. 621–638. DOI: [10.1029/2000RS002396](https://doi.org/10.1029/2000RS002396).
- Delanoë, J. et al. (2016). "BASTA: A 95-GHz FMCW Doppler radar for cloud and fog studies". In: *Journal of Atmospheric and Oceanic Technology* 33.5, pp. 1023–1038. ISSN: 15200426. DOI: [10.1175/JTECH-D-15-0104.1](https://doi.org/10.1175/JTECH-D-15-0104.1).
- Delucchi, M. A. and M. Z. Jacobson (2011). "Providing all global energy with wind, water, and solar power, Part II: Reliability, system and transmission costs, and policies". In: *Energy Policy* 39.3, pp. 1170–1190. ISSN: 03014215. DOI: [10.1016/j.enpol.2010.11.045](https://doi.org/10.1016/j.enpol.2010.11.045). URL: <http://dx.doi.org/10.1016/j.enpol.2010.11.045>.
- Doviak, R. J. and D. S. Zrnić (1993). "4 - Weather Signals". In: *Doppler Radar and Weather Observations (Second Edition)*. Ed. by Richard J Doviak and Dušan S Zrnić. Second Edi. San Diego: Academic Press, pp. 64–86. ISBN: 978-0-12-221422-6. DOI: <https://doi.org/10.1016/B978-0-12-221422-6.50009-7>.
- Doviak, R. J., D. S. Zrnić, and D. S. Sirmans (1979). "Doppler Weather Radar". In: *Proceedings of the IEEE*. Vol. 67. 11, pp. 1522–1553. DOI: [0018-9219/79/1100-1522\\$00.75](https://doi.org/10.1109/1100-1522$00.75).
- Dowling, P. (2013). "The impact of climate change on the European energy system". In: *Energy Policy* 60, pp. 406–417. ISSN: 03014215. DOI: [10.1016/j.enpol.2013.05.093](https://doi.org/10.1016/j.enpol.2013.05.093). URL: <http://dx.doi.org/10.1016/j.enpol.2013.05.093>.
- Dufresne, J. L. and S. Bony (2008). "An assessment of the primary sources of spread of global warming estimates from coupled atmosphere-ocean models". In: *Journal of Climate* 21.19, pp. 5135–5144. ISSN: 08948755. DOI: [10.1175/2008JCLI2239.1](https://doi.org/10.1175/2008JCLI2239.1).
- Ebell, K. et al. (2011). "Cloud statistics and cloud radiative effect for a low-mountain site". In: *Quarterly Journal of the Royal Meteorological Society* 137.SUPPL. 1, pp. 306–324. ISSN: 00359009. DOI: [10.1002/qj.748](https://doi.org/10.1002/qj.748).
- Feingold, G. et al. (1994). "An explicit cloud microphysics/LES model designed to simulate the Twomey effect". In: *Atmospheric Research* 33.1, pp. 207–233. ISSN: 0169-8095. DOI: [https://doi.org/10.1016/0169-8095\(94](https://doi.org/10.1016/0169-8095(94)

- 90021-3. URL: <http://www.sciencedirect.com/science/article/pii/S0169809594900213>.
- Fielding, M. D. et al. (2014). "A novel ensemble method for retrieving properties of warm cloud in 3-D using ground-based scanning radar and zenith radiances". In: *Journal of Geophysical Research: Atmospheres* 119, pp. 10912–10930. DOI: [10.1002/2014JD021742](https://doi.org/10.1002/2014JD021742).
- Fox, N. I. and A. J. Illingworth (1997). "The Retrieval of Stratocumulus Cloud Properties by Ground-Based Cloud Radar". In: *Journal of Applied Meteorology* 36.5, pp. 485–492. ISSN: 0894-8763. DOI: [10.1175/1520-0450\(1997\)036<0485:TR0SCP>2.0.CO;2](https://doi.org/10.1175/1520-0450(1997)036<0485:TR0SCP>2.0.CO;2).
- Frankfurt School-UNEP (2018). *Global Trends in Renewable Energy investment 2018*. Tech. rep. Frankfurt: FS-UNEP Collaborating Centre for Climate & Sustainable Energy Finance. URL: <http://fs-uneep-centre.org/publications/global-trends-renewable-energy-investment-report-2018>.
- Frisch, A. S., C. W. Fairall, and J. B. Snider (1995). "Measurement of Stratus Cloud and Drizzle Parameters in ASTEX with a Ka -Band Doppler Radar and a Microwave Radiometer". In: *Journal of the Atmospheric Sciences* 52.16, pp. 2788–2799. DOI: [10.1175/1520-0469\(1995\)052<2788:MOSCAD>2.0.CO;2](https://doi.org/10.1175/1520-0469(1995)052<2788:MOSCAD>2.0.CO;2).
- Frisch, A. S. et al. (1998). "On cloud radar and microwave radiometer measurements of stratus cloud liquid water profiles". In: *Journal of Geophysical Research: Atmospheres* 103.18, pp. 23195–23197. DOI: [10.1029/1987JD011827](https://doi.org/10.1029/1987JD011827).
- Gaffard, C. and T. Hewison (2003). "Radiometrics MP3000 Microwave Radiometer Trial Report". In: *Water* 44.0, pp. 1–27.
- Gerber, H. (1996). "Microphysics of Marine Stratocumulus Clouds with Two Drizzle Modes". In: *Journal of the Atmospheric Sciences* 53.12, pp. 1649–1662. ISSN: 0022-4928. DOI: [10.1175/1520-0469\(1996\)053<1649:MOMSCW>2.0.CO;2](https://doi.org/10.1175/1520-0469(1996)053<1649:MOMSCW>2.0.CO;2). URL: [http://journals.ametsoc.org/doi/abs/10.1175/1520-0469\(1996\)053<1649:MOMSCW>2.0.CO;2](http://journals.ametsoc.org/doi/abs/10.1175/1520-0469(1996)053<1649:MOMSCW>2.0.CO;2).
- Gerland, P. et al. (2014). *World population stabilization unlikely this century*. Tech. rep. 6206, pp. 234–237. DOI: [10.1126/science.1257469](https://doi.org/10.1126/science.1257469).
- Giangrande, S. E. et al. (2016). "Insights into riming and aggregation processes as revealed by aircraft, radar, and disdrometer observations for a 27 April 2011 widespread precipitation event". In: *Journal of Geophysical Research* 121.10, pp. 5846–5863. ISSN: 21562202. DOI: [10.1002/2015JD024537](https://doi.org/10.1002/2015JD024537).

- Görsdorf, U. et al. (2015). "A 35-GHz polarimetric doppler radar for long-term observations of cloud parameters-description of system and data processing". In: *Journal of Atmospheric and Oceanic Technology* 32.4, pp. 675–690. ISSN: 15200426. DOI: [10.1175/JTECH-D-14-00066.1](https://doi.org/10.1175/JTECH-D-14-00066.1).
- Gunn, R. and G. D. Kinzer (1949). *The Terminal Velocity of Fall for Water Droplets in Stagnant Air*. DOI: [10.1175/1520-0469\(1949\)006<0243:TTVOFF>2.0.CO;2](https://doi.org/10.1175/1520-0469(1949)006<0243:TTVOFF>2.0.CO;2).
- Henckes, P. et al. (2018a). "The benefit of long-term high resolution wind data for electricity system analysis". In: *Energy* 143, pp. 934–942. ISSN: 0360-5442. DOI: <https://doi.org/10.1016/j.energy.2017.10.049>. URL: <http://www.sciencedirect.com/science/article/pii/S0360544217317280>.
- Henckes, P. et al. (2018b). "Uncertainty in energy system investment models based on a climatological reanalysis". In: *Energy* in preparation.
- Herring, S. C. et al. (2014). "Explaining Extreme Events of 2013 from a Climate Perspective". In: *American Meteorological Society* 95.9, pp. 1–96. ISSN: 0003-0007. DOI: [10.1175/1520-0477-95.9.S1.1](https://doi.org/10.1175/1520-0477-95.9.S1.1).
- Hersbach, H. et al. (2017). "The potential value of early (1939–1967) upper-air data in atmospheric climate reanalysis". In: *Quarterly Journal of the Royal Meteorological Society* 143.704, pp. 1197–1210. ISSN: 1477870X. DOI: [10.1002/qj.3040](https://doi.org/10.1002/qj.3040).
- Hewison, T. J. and C. Gaffard (2007). "1D-VAR retrieval of temperature and humidity profiles from a ground-based microwave radiometer". In: *IEEE Transactions on Geoscience and Remote Sensing* 45.7, pp. 2163–2168. ISSN: 01962892. DOI: [10.1109/TGRS.2007.898091](https://doi.org/10.1109/TGRS.2007.898091).
- Hildebrand, P. H. and R. S. Sekhon (1974). "Objective Determination of the Noise Level in Doppler Spectra". In: *Journal of Applied Meteorology* 13.7, pp. 808–811. ISSN: 0021-8952. DOI: [10.1175/1520-0450\(1974\)013<0808:ODOTNL>2.0.CO;2](https://doi.org/10.1175/1520-0450(1974)013<0808:ODOTNL>2.0.CO;2).
- Hogan, R. J., N. Gaussiat, and A. J. Illingworth (2005). "Stratocumulus liquid water content from dual-wavelength radar". In: *Journal of Atmospheric and Oceanic Technology* 22.8, pp. 1207–1218. ISSN: 07390572. DOI: [10.1175/JTECH1768.1](https://doi.org/10.1175/JTECH1768.1).
- Hogan, R. J. et al. (2003). "Absolute calibration of 94/95-GHz radars using rain". In: *Journal of Atmospheric and Oceanic Technology* 20.4, pp. 572–580. ISSN: 07390572. DOI: [10.1175/1520-0426\(2003\)20<572:ACOGRU>2.0.CO;2](https://doi.org/10.1175/1520-0426(2003)20<572:ACOGRU>2.0.CO;2).

- Houze, R. A. (2014a). "Chapter 4 - Remote Sensing of Clouds and Precipitation". In: *Cloud Dynamics*. Ed. by R. A. Houze. Vol. 104. International Geophysics. Academic Press, pp. 77–97. DOI: <https://doi.org/10.1016/B978-0-12-374266-7.00004-4>. URL: <http://www.sciencedirect.com/science/article/pii/B9780123742667000044>.
- (2014b). "Chapter 5 - Clouds in Shallow Layers at Low, Middle, and High Levels". In: *Cloud Dynamics*. Ed. by R. A. Houze. Vol. 104. International Geophysics. Academic Press, pp. 101–140. DOI: <https://doi.org/10.1016/B978-0-12-374266-7.00005-6>. URL: <http://www.sciencedirect.com/science/article/pii/B9780123742667000056>.
- Huggard, P. G. et al. (2008). "94 GHz FMCW cloud radar". In: *Proceedings of SPIE 7117, Millimetre Wave and Terahertz Sensors and Technology*. Cardiff. URL: <http://dx.doi.org/10.1117/12.800347>.
- Illingworth, A. J. et al. (2007). "Cloudnet: Continuous evaluation of cloud profiles in seven operational models using ground-based observations". In: *Bulletin of the American Meteorological Society* 88.6, pp. 883–898. ISSN: 00030007. DOI: [10.1175/BAMS-88-6-883](https://doi.org/10.1175/BAMS-88-6-883).
- IPCC (2014). *Summary for Policymakers*. Tech. rep. Geneva, Switzerland: IPCC. DOI: [10.1017/CB09781107415324](https://doi.org/10.1017/CB09781107415324). arXiv: [arXiv:1011.1669v3](https://arxiv.org/abs/1011.1669v3).
- Kaundinya, D. P., P. Balachandra, and N. H. Ravindranath (2009). "Grid-connected versus stand-alone energy systems for decentralized power-A review of literature". In: *Renewable and Sustainable Energy Reviews* 13.8, pp. 2041–2050. ISSN: 13640321. DOI: [10.1016/j.rser.2009.02.002](https://doi.org/10.1016/j.rser.2009.02.002). arXiv: [arXiv:1011.1669v3](https://arxiv.org/abs/1011.1669v3).
- Kessler, E. (1969). "On the Distribution and Continuity of Water Substance in Atmospheric Circulations". In: *On the Distribution and Continuity of Water Substance in Atmospheric Circulations*. Boston, MA: American Meteorological Society, pp. 1–84. ISBN: 978-1-935704-36-2. DOI: [10.1007/978-1-935704-36-2\\_1](https://doi.org/10.1007/978-1-935704-36-2_1). URL: [https://doi.org/10.1007/978-1-935704-36-2\\_{\\_}1](https://doi.org/10.1007/978-1-935704-36-2_{_}1).
- Khain, A. et al. (2008). "Combined observational and model investigations of the Z-LWC relationship in stratocumulus clouds". In: *Journal of Applied Meteorology and Climatology* 47.2, pp. 591–606. ISSN: 15588424. DOI: [10.1175/2007JAMC1701.1](https://doi.org/10.1175/2007JAMC1701.1).
- Kim, B. G., S. A. Klein, and J. R. Norris (2005). "Continental liquid water cloud variability and its parameterization using Atmospheric Radiation Measurement data". In: *Journal of Geophysical Research D: Atmospheres* 110.15, pp. 1–18. ISSN: 01480227. DOI: [10.1029/2004JD005122](https://doi.org/10.1029/2004JD005122).

- Klucher, T. M. (1979). "Evaluation of models to predict insolation on tilted surfaces". In: *Solar Energy* 23.2, pp. 111–114. ISSN: 0038-092X. DOI: [https://doi.org/10.1016/0038-092X\(79\)90110-5](https://doi.org/10.1016/0038-092X(79)90110-5). URL: <http://www.sciencedirect.com/science/article/pii/0038092X79901105>.
- Kneifel, S., M. S. Kulie, and R. Bennartz (2011). "A triple-frequency approach to retrieve microphysical snowfall parameters". In: *Journal of Geophysical Research: Atmospheres* 116.11, pp. 1–15. ISSN: 01480227. DOI: [10.1029/2010JD015430](https://doi.org/10.1029/2010JD015430).
- Kneifel, S. et al. (2016). "First observations of triple-frequency radar Doppler spectra in snowfall: Interpretation and applications". In: *Geophysical Research Letters* 43.5, pp. 2225–2233. ISSN: 19448007. DOI: [10.1002/2015GL067618](https://doi.org/10.1002/2015GL067618).
- Kogan, Y. L., Z. N. Kogan, and D. B. Mechem (2007). "Assessing the Errors of Microphysical Retrievals Based on Doppler Radar Parameters". In: *Journal of Hydrometeorology - Special Section* 8, pp. 665–677. ISSN: 1525-755X. DOI: [10.1175/JHM603.1](https://doi.org/10.1175/JHM603.1).
- Kollias, P., B. A. Albrecht, and F. Marks (2002). "Why Mie?" In: *Bulletin of the American Meteorological Society* 83.10, pp. 1471–1483. ISSN: 0003-0007. DOI: [10.1175/BAMS-83-10-1471](https://doi.org/10.1175/BAMS-83-10-1471). URL: <http://journals.ametsoc.org/doi/abs/10.1175/BAMS-83-10-1471>.
- Kollias, P. et al. (2007). "Millimeter-wavelength radars: New frontier in atmospheric cloud and precipitation research". In: *Bulletin of the American Meteorological Society* 88.10, pp. 1608–1624. ISSN: 00030007. DOI: [10.1175/BAMS-88-10-1608](https://doi.org/10.1175/BAMS-88-10-1608).
- Kollias, P. et al. (2011). "Cloud radar Doppler spectra in drizzling stratiform clouds: 2. Observations and microphysical modeling of drizzle evolution". In: *Journal of Geophysical Research Atmospheres* 116.13, pp. 1–14. ISSN: 01480227. DOI: [10.1029/2010JD015238](https://doi.org/10.1029/2010JD015238).
- Küchler, N. and U. Löhnert (2018). "Radar-radiometer based liquid water content retrievals of warm low-level clouds: how the measurement setup affects retrieval uncertainties". In: *IEEE Journal of Selected Topics in Applied Earth Observations and Remote Sensing* under review.
- Küchler, N. et al. (2016). "Calibrating ground-based microwave radiometers: Uncertainty and drifts". In: *Radio Science* 51.4, pp. 311–327. DOI: [10.1002/2015RS005826](https://doi.org/10.1002/2015RS005826).
- Küchler, N. et al. (2017). "A W-Band Radar–Radiometer System for Accurate and Continuous Monitoring of Clouds and Precipitation". In: *Journal of Atmospheric and Oceanic Technology* 34.11, pp. 2375–2392. ISSN: 0739-0572.

- DOI: [10.1175/JTECH-D-17-0019.1](https://doi.org/10.1175/JTECH-D-17-0019.1). URL: <http://journals.ametsoc.org/doi/10.1175/JTECH-D-17-0019.1>.
- Küchler, N. et al. (2018). "Revisiting liquid water content retrievals in warm stratified clouds: The modified Frisch". In: *Geophysical Research Letters* 45.17. DOI: <https://doi.org/10.1029/2018GL079845>.
- Kumar, B. et al. (2017). "Cloud-edge mixing: Direct numerical simulation and observations in Indian Monsoon clouds". In: *Journal of Advances in Modeling Earth Systems* 9.1, pp. 332–353. DOI: [10.1002/2013MS000282](https://doi.org/10.1002/2013MS000282).
- Lamb, D. and J. Verlinde (2011). *Physics and Chemistry of Clouds*. Cambridge University Press. DOI: [10.1017/CB09780511976377](https://doi.org/10.1017/CB09780511976377).
- Langodan, S. et al. (2016). "A high-resolution assessment of wind and wave energy potentials in the Red Sea". In: *Applied Energy* 181, pp. 244–255. ISSN: 03062619. DOI: [10.1016/j.apenergy.2016.08.076](https://doi.org/10.1016/j.apenergy.2016.08.076). URL: <http://dx.doi.org/10.1016/j.apenergy.2016.08.076>.
- Lhermitte, R. M. (1987). "Small cumuli observed with a 3 mm wavelength Doppler radar". In: *Geop* 14.7, pp. 707–710. DOI: [10.1029/GL014i007p00707](https://doi.org/10.1029/GL014i007p00707).
- Li, L. et al. (2005). "Measurements of ocean surface backscattering using an airborne 94-GHz cloud radar - Implication for calibration of airborne and spaceborne w-band radars". In: *Journal of Atmospheric and Oceanic Technology* 22.7, pp. 1033–1045. ISSN: 07390572. DOI: [10.1175/JTECH1722.1](https://doi.org/10.1175/JTECH1722.1).
- Lilly, D. K. (1968). "Models of cloud-topped mixed layers under a strong inversion". In: *Quarterly Journal of the Royal Meteorological Society* 94.401, pp. 292–309. DOI: <https://doi.org/10.1002/qj.49709440106>.
- Löhnert, U. and S. Crewell (2003). "Accuracy of cloud liquid water path from ground-based microwave radiometry 1. Dependency on cloud model statistics". In: *Radio Science* 38.3, pp. 1–11. ISSN: 0048-6604. DOI: [10.1029/2002RS002654](https://doi.org/10.1029/2002RS002654).
- Löhnert, U. et al. (2001). "Profiling cloud liquid water by combining active and passive microwave measurements with cloud model statistics". In: *Journal of Atmospheric and Oceanic Technology* 18.8, pp. 1354–1366. ISSN: 07390572. DOI: [10.1175/1520-0426\(2001\)018<1354:PCLWBC>2.0.CO;2](https://doi.org/10.1175/1520-0426(2001)018<1354:PCLWBC>2.0.CO;2).
- Löhnert, U. et al. (2008). "Advances in continuously profiling the thermodynamic state of the boundary layer: Integration of measurements and methods". In: *Journal of Atmospheric and Oceanic Technology* 25.8, pp. 1251–1266. ISSN: 07390572. DOI: [10.1175/2007JTECHA961.1](https://doi.org/10.1175/2007JTECHA961.1).
- Lorenz, E. et al. (2011). "Regional PV power prediction for improved grid integration". In: *Progress in Photovoltaics: Research and Applications* 19.7, pp. 757–771. DOI: [10.1002/pip](https://doi.org/10.1002/pip).



- Luke, E. P. and P. Kollias (2013). "Separating cloud and drizzle radar moments during precipitation onset using doppler spectra". In: *Journal of Atmospheric and Oceanic Technology* 30.8, pp. 1656–1671. ISSN: 07390572. DOI: [10.1175/JTECH-D-11-00195.1](https://doi.org/10.1175/JTECH-D-11-00195.1).
- Maahn, M. et al. (2015). "Developing and Evaluating Ice Cloud Parameterizations for Forward Modeling of Radar Moments Using In Situ Aircraft Observations". In: *Journal of Atmospheric and Oceanic Technology* 32.5, pp. 880–903. ISSN: 0739-0572. DOI: [10.1175/JTECH-D-14-00112.1](https://doi.org/10.1175/JTECH-D-14-00112.1). URL: <http://journals.ametsoc.org/doi/abs/10.1175/JTECH-D-14-00112.1>.
- Madsen, H. et al. (2014). "Review of trend analysis and climate change projections of extreme precipitation and floods in Europe". In: *Journal of Hydrology* 519.PD, pp. 3634–3650. ISSN: 00221694. DOI: [10.1016/j.jhydrol.2014.11.003](https://doi.org/10.1016/j.jhydrol.2014.11.003). URL: <http://dx.doi.org/10.1016/j.jhydrol.2014.11.003>.
- Marchand, R. et al. (2008). "Hydrometeor Detection Using Cloudsat - An Earth-Orbiting 94-GHz Radar". In: *Journal of Atmospheric and Oceanic Technology* 25.4, pp. 519–533. ISSN: 07390572. DOI: [10.1175/2007JTECHA1006.1](https://doi.org/10.1175/2007JTECHA1006.1).
- Maschwitz, G. et al. (2013). "Investigation of ground-based microwave radiometer calibration techniques at 530 hPa". In: *Atmospheric Measurement Techniques* 6.10, pp. 2641–2658. ISSN: 18671381. DOI: [10.5194/amt-6-2641-2013](https://doi.org/10.5194/amt-6-2641-2013).
- McFiggans, G. et al. (2006). "The effect of physical and chemical aerosol properties on warm cloud droplet activation". In: *Atmospheric Chemistry and Physics* 6.9, pp. 2593–2649. ISSN: 16807324. DOI: [10.5194/acp-6-2593-2006](https://doi.org/10.5194/acp-6-2593-2006).
- Merker, C. et al. (2015). "A novel approach for absolute radar calibration: formulation and theoretical validation". In: *Atmospheric Measurement Techniques* 8.6, pp. 2521–2530. ISSN: 1867-8548. DOI: [10.5194/amt-8-2521-2015](https://doi.org/10.5194/amt-8-2521-2015). URL: <http://www.atmos-meas-tech.net/8/2521/2015/>.
- Mie, G. (1908). "Beiträge zur Optik trüber Medien, speziell kolloidaler Metallösungen". In: *Analen der Physik* 25.3. DOI: [10.1002/andp.19083300302](https://doi.org/10.1002/andp.19083300302).
- Miles, N. L., J. Verlinde, and E. E. Clothiaux (2000). "Cloud Droplet Size Distributions in Low-Level Stratiform Clouds". In: *Journal of the Atmospheric Sciences* 57.2, pp. 295–311. ISSN: 0022-4928. DOI: [10.1175/1520-0469\(2000\)057<0295:CDSDIL>2.0.CO;2](https://doi.org/10.1175/1520-0469(2000)057<0295:CDSDIL>2.0.CO;2).
- Nahmacher, P. et al. (2016). "Carpe diem: A novel approach to select representative days for long-term power system modeling". In: *Energy* 112,

- pp. 430–442. ISSN: 0360-5442. DOI: <http://dx.doi.org/10.1016/j.energy.2016.06.081>. URL: <http://www.sciencedirect.com/science/article/pii/S0360544216308556>.
- Nature Editorial (2016). *Meet the challenge of interdisciplinary science*. Tech. rep., pp. 589–590. DOI: [10.1038/534589b](https://doi.org/10.1038/534589b).
- Nicholls, S. (1989). “The structure of radiatively driven convection in stratocumulus”. In: *Quarterly Journal of the Royal Meteorological Society* 115.487, pp. 487–511. ISSN: 1477870X. DOI: [10.1002/qj.49711548704](https://doi.org/10.1002/qj.49711548704).
- Nicholls, S. and J. Leighton (1986). “An observational study of the structure of stratiform cloud sheets: Part I. Structure”. In: *Quarterly Journal of the Royal Meteorological Society* 112.472, pp. 431–460. DOI: <https://doi.org/10.1002/qj.49711247209>.
- Perez, R. et al. (1990). “Modeling daylight availability and irradiance components from direct and global irradiance”. In: *Solar Energy* 44.5, pp. 271–289. ISSN: 0038-092X. DOI: [https://doi.org/10.1016/0038-092X\(90\)90055-H](https://doi.org/10.1016/0038-092X(90)90055-H). URL: <http://www.sciencedirect.com/science/article/pii/S0038092X9090055H>.
- Petty, G. W. (2006). *A First Course in Atmospheric Radiation*. Second Edi. Sundog Publishing. ISBN: 978-0-9729033-1-8.
- Reeves, R. G., A. Ansons, and D. Landen (1975). *Manual of Remote Sensing*. 1st ed. Falls Church: American Society of Photogrammetry.
- Rockström, J. et al. (2017). “A roadmap for rapid decarbonization”. In: *Science* 355.6331, pp. 1269–1271. ISSN: 0036-8075. DOI: [10.1126/science.aah3443](https://doi.org/10.1126/science.aah3443). URL: <http://science.sciencemag.org/content/355/6331/1269>.
- Rogers, R. R. and M. K. Yau (1989). *A Short Course in Cloud Physics*. 3rd ed. Butterworth-Heinemann. ISBN: 9780750632157.
- Rooy, W. C. de et al. (2013). “Entrainment and detrainment in cumulus convection: an overview”. In: *Quarterly Journal of the Royal Meteorological Society* 139.670, pp. 1–19. ISSN: 00359009. DOI: [10.1002/qj.1959](https://doi.org/10.1002/qj.1959). URL: <http://doi.wiley.com/10.1002/qj.1959>.
- Rose, T. et al. (2005). “A network suitable microwave radiometer for operational monitoring of the cloudy atmosphere”. In: *Atmospheric Research* 75.3, pp. 183–200. ISSN: 01698095. DOI: [10.1016/j.atmosres.2004.12.005](https://doi.org/10.1016/j.atmosres.2004.12.005).
- Rossow, W. B. and R. A. Schiffer (1999). “Advances in Understanding Clouds from ISCCP”. In: *Bulletin of the American Meteorological Society* 80.11, pp. 2261–2287. ISSN: 00030007. DOI: [10.1175/1520-0477\(1999\)080<2261:AIUCFI>2.0.CO;2](https://doi.org/10.1175/1520-0477(1999)080<2261:AIUCFI>2.0.CO;2).

- Rusli, S. P., D. P. Donovan, and H. W. J. Russchenberg (2017). "Simultaneous and synergistic profiling of cloud and drizzle properties using ground-based observations". In: *Atmospheric Measurement Techniques* 10.12, pp. 4777–4803. ISSN: 18678548. DOI: [10.5194/amt-10-4777-2017](https://doi.org/10.5194/amt-10-4777-2017).
- Sauvageot, H. and J. Omar (1987). *Radar Reflectivity of Cumulus Clouds*. DOI: [10.1175/1520-0426\(1987\)004<0264:RR0CC>2.0.CO;2](https://doi.org/10.1175/1520-0426(1987)004<0264:RR0CC>2.0.CO;2).
- Shannon, C. E. (1949). "Communication in the Presence of Noise". In: *Proceedings of the IRE* 37.1, pp. 10–21. ISSN: 0096-8390. DOI: [10.1109/JRPROC.1949.232969](https://doi.org/10.1109/JRPROC.1949.232969).
- Slingo, A. (1990). "Sensitivity of the Earth's radiation budget to changes in low clouds". In: *Nature* 343.6253, pp. 49–51. ISSN: 00280836. DOI: [10.1038/343049a0](https://doi.org/10.1038/343049a0).
- Stephens, G. L. and J. M. Haynes (2007). "Near global observations of the warm rain coalescence process". In: *Geophysical Research Letters* 34.20, pp. 1–5. ISSN: 00948276. DOI: [10.1029/2007GL030259](https://doi.org/10.1029/2007GL030259).
- Stephens, G L, G W Paltridge, and C M R Platt (1978). "Radiation Profiles in Extended Water Clouds. III: Observations". In: *Journal of the Atmospheric Sciences* 35.11, pp. 2133–2141. ISSN: 0022-4928. DOI: [10.1175/1520-0469\(1978\)035<2133:RPIEWC>2.0.CO;2](https://doi.org/10.1175/1520-0469(1978)035<2133:RPIEWC>2.0.CO;2). URL: [http://journals.ametsoc.org/doi/abs/10.1175/1520-0469\(1978\)035<2133:RPIEWC>2.0.CO;2](http://journals.ametsoc.org/doi/abs/10.1175/1520-0469(1978)035<2133:RPIEWC>2.0.CO;2).
- Stevens, B. et al. (2003). "Dynamics and Chemistry of Marine Stratocumulus - DYCOMS-II". In: *Bulletin of the American Meteorological Society* 84.5, pp. 579–593+548. ISSN: 00030007. DOI: [10.1175/BAMS-84-5-579](https://doi.org/10.1175/BAMS-84-5-579).
- Strauch, R. G. (1976). "Theory and application of the FM-CW doppler radar". PhD thesis. University of Colorado.
- Teuling, A. J. (2018). "A hot future for European droughts". In: *Nature Climate Change* 8.5, pp. 364–365. ISSN: 17586798. DOI: [10.1038/s41558-018-0154-5](https://doi.org/10.1038/s41558-018-0154-5).
- Thies, B. et al. (2010). "Fog monitoring using a new 94 GHz FMCW cloud radar". In: *5th International Conference on Fog, Fog Collection and Dew*. July. Münster, Germany. URL: <http://adsabs.harvard.edu/abs/2010ffcd.confE.103T>.
- Tridon, F. and A. Battaglia (2015). "Dual-frequency radar Doppler spectral retrieval of rain drop size distributions and entangled dynamics variables". In: *Journal of Geophysical Research: Atmospheres* 120.11, pp. 5585–5601. ISSN: 21698996. DOI: [10.1002/2014JD023023](https://doi.org/10.1002/2014JD023023). Received.

- Turner, D. D. et al. (2007). "Retrieving Liquid Water Path and Precipitable Water Vapor From the Atmospheric Radiation Measurement (ARM) Microwave Radiometers". In: *IEEE Transactions on Geoscience and Remote Sensing* 45.11, pp. 3680–3690. ISSN: 0196-2892. DOI: [10.1109/TGRS.2007.903703](https://doi.org/10.1109/TGRS.2007.903703).
- Ulaby, F. T., R. K. Moore, and K. A. Fung (1981). *Microwave Remote Sensing*. Addison-Wesley.
- Ulaby, F.T. and D. G. Long (2014). *Microwave Radar and Radiometric Remote Sensing*. 1st ed. The University of Michigan Press, pp. 615–621. ISBN: 978-0-472-11935-6.
- UNFCCC (2015). *Paris Agreement*. Tech. rep. December, p. 32. URL: <http://unfccc.int/resource/docs/2015/cop21/eng/l09r01.pdf>.
- United Nations (2017). *The Sustainable Development Goals Report*. Tech. rep. New York. DOI: [10.18356/3405d09f-en](https://doi.org/10.18356/3405d09f-en). URL: <https://unstats.un.org/sdgs/files/report/2017/TheSustainableDevelopmentGoalsReport2017.pdf>.
- Uyar, T. S. and D. Beşikci (2017). "Integration of hydrogen energy systems into renewable energy systems for better design of 100% renewable energy communities". In: *International Journal of Hydrogen Energy* 42.4, pp. 2453–2456. ISSN: 03603199. DOI: [10.1016/j.ijhydene.2016.09.086](https://doi.org/10.1016/j.ijhydene.2016.09.086).
- Vidaurre, G., J. Hallett, and D. C. Rogers (2011). "Airborne measurement of liquid and total water content". In: *Journal of Atmospheric and Oceanic Technology* 28.9, pp. 1088–1103. ISSN: 07390572. DOI: [10.1175/JTECH-D-10-05035.1](https://doi.org/10.1175/JTECH-D-10-05035.1).
- Wahl, S. et al. (2017). "A novel convective-scale regional reanalysis COSMO-REA2: Improving the representation of precipitation". In: *Meteorologische Zeitschrift* 26.4, pp. 345–361. ISSN: 16101227. DOI: [10.1127/metz/2017/0824](https://doi.org/10.1127/metz/2017/0824).
- Wang, J. and B. Geerts (2003). "Identifying drizzle within marine stratus with W-band radar reflectivity". In: *Atmospheric Research* 69.1-2, pp. 1–27. ISSN: 01698095. DOI: [10.1016/j.atmosres.2003.08.001](https://doi.org/10.1016/j.atmosres.2003.08.001).
- Wang, Y. et al. (2017). "Identification of precipitation onset based on Cloudsat observations". In: *Journal of Quantitative Spectroscopy and Radiative Transfer* 188, pp. 142–147. ISSN: 00224073. DOI: [10.1016/j.jqsrt.2016.06.028](https://doi.org/10.1016/j.jqsrt.2016.06.028). URL: <http://dx.doi.org/10.1016/j.jqsrt.2016.06.028>.

- Wang, Z. et al. (2012). "Single aircraft integration of remote sensing and in situ sampling for the study of cloud microphysics and dynamics". In: *Bulletin of the American Meteorological Society* 93.5, pp. 653–668. ISSN: 00030007. DOI: [10.1175/BAMS-D-11-00044.1](https://doi.org/10.1175/BAMS-D-11-00044.1).
- Wood, R. (2005). "Drizzle in Stratiform Boundary Layer Clouds. Part I: Vertical and Horizontal Structure". In: *Journal of the Atmospheric Sciences* 62.9, pp. 3011–3033. ISSN: 0022-4928. DOI: [10.1175/JAS3529.1](https://doi.org/10.1175/JAS3529.1). URL: <http://journals.ametsoc.org/doi/abs/10.1175/JAS3529.1>.
- (2012). "Stratocumulus Clouds". In: *Monthly Weather Review* 140.8, pp. 2373–2423. ISSN: 0027-0644. DOI: [10.1175/MWR-D-11-00121.1](https://doi.org/10.1175/MWR-D-11-00121.1).
- (2015). "CLOUDS AND FOG | Stratus and Stratocumulus". In: *Encyclopedia of Atmospheric Sciences (Second Edition)*. Ed. by Gerald R North, John Pyle, and Fuqing Zhang. Second Edi. Oxford: Academic Press, pp. 196–200. ISBN: 978-0-12-382225-3. DOI: <https://doi.org/10.1016/B978-0-12-382225-3.00396-0>. URL: <http://www.sciencedirect.com/science/article/pii/B9780123822253003960>.
- Wood, R. et al. (2011). "The VAMOS Ocean-Cloud-Atmosphere-Land Study Regional Experiment (VOCALS-REx): goals, platforms, and field operations". In: *Atmospheric Chemistry and Physics* 11.2, pp. 627–654. DOI: [10.5194/acp-11-627-2011](https://doi.org/10.5194/acp-11-627-2011). URL: <https://www.atmos-chem-phys.net/11/627/2011/>.
- Yamaguchi, J. et al. (2009). "Evaluation of Radar Reflectivity (Z) for FMCW Millimeter-Wave Cloud Radar "FALCON-I"". In: *IEEE Transactions on Fundamentals and Materials* 129.4, pp. 183–189. DOI: <http://doi.org/10.1541/ieejfms.129.183>.
- Yu, G. et al. (2014). "Mixed-phase cloud phase partitioning using millimeter wavelength cloud radar Doppler velocity spectra". In: *Journal of Geophysical Research: Atmospheres* 119.12, pp. 7556–7576. DOI: [10.1002/2013JD021182](https://doi.org/10.1002/2013JD021182). URL: <https://agupubs.onlinelibrary.wiley.com/doi/abs/10.1002/2013JD021182>.
- Zhang, H. et al. (2018). "Quantitative synergy assessment of regional wind-solar energy resources based on MERRA reanalysis data". In: *Applied Energy* 216. December 2017, pp. 172–182. ISSN: 03062619. DOI: [10.1016/j.apenergy.2018.02.094](https://doi.org/10.1016/j.apenergy.2018.02.094). URL: <https://doi.org/10.1016/j.apenergy.2018.02.094>.
- Zhang, M. H. et al. (2005). "Comparing clouds and their seasonal variations in 10 atmospheric general circulation models with satellite measurements".

In: *Journal of Geophysical Research D: Atmospheres* 110.15, pp. 1–18. ISSN: 01480227. DOI: [10.1029/2004JD005021](https://doi.org/10.1029/2004JD005021).

Zhao, C. et al. (2012). “Toward understanding of differences in current cloud retrievals of ARM ground-based measurements”. In: *Journal of Geophysical Research Atmospheres* 117.10. ISSN: 01480227. DOI: [10.1029/2011JD016792](https://doi.org/10.1029/2011JD016792).

Zuidema, P. et al. (2005). “Ship-based liquid water path estimates in marine stratocumulus”. In: *Journal of Geophysical Research* 110.D20206. DOI: [10.1029/2005JD005833](https://doi.org/10.1029/2005JD005833).

# Danksagung

Danke liebe Verwaltung der Universität zu K., dass ihr euch stets bemüht habt keine Langeweile in meinem so tristen Alltag am Schreibtisch aufkommen zu lassen. Insbesondere werde ich niemals vergessen, dass ihr mich gebeten habt bei meiner nächsten Nutzung eines Handytickets in der Deutschen Bahn einen "Selfy" von mir und dem Schaffner zu machen, damit ich nachweisen kann, dass ich auch wirklich im Zug saß - danke!

Passend dazu, liebe Dagmar, danke dass du das immer ausgehalten hast und mich auch bei sonstigen bürokratischen Ereignissen unterstützt hast. Danke auch euch, Nadine und Sarah.

Uli, danke für deine unglaublich gute Betreuung, für die Freiheit, die du mir gegeben hast und dabei trotzdem dafür gesorgt hast, dass ich mich nicht verlaufe.

Susanne, danke für alles was du mir in meinen Jahren in deiner Arbeitsgruppe und als Student ermöglicht hast.

Rosa, thanks for making this office what it is.

Tobi, danke für all die Ruhe, die du in unseren gemeinsamen Jahren (von Anfang bis zum Ende) ausgestrahlt hast.

Erlend, svigersønn av min mor, thanks for your engagement and motivation - it reached me.

Stefan, danke für Input, Korrekturlesen, Rückmelden, Diskussionen und dafür, dass auch immer ein Schwätzchen über irgendwas anderes möglich war.

Pavlos, thanks a lot for hosting and pushing me in the last third of my thesis.

Liebe Eltern, danke, dass ihr mir immer das Gefühl gegeben habt, dass ich alles schaffen kann. Ohne das würde es diese Dissertation wohl nicht geben.

Liebe Marlene, lieber Markus, danke für unser zu Hause, dass ihr mir den Rücken frei gehalten habt, immer ein offenes Ohr hattet, insbesondere in Zeiten fehlender Motivation und Frustration. Lieber Andi, danke auch dir, vorallem für musikalische Inspiration.

Jakob, danke, dass du mich daran erinnerst mehr im Moment zu leben.

Karl, danke fürs zuverlässige Auffangen - nicht nur am Kletterseil.

Jonas, danke fürs Fachsimpeln, ob über Didaktik, Fußball oder die ganze Welt.

Christopher, danke für einen guten Start ins Doktorat.

Silvan, es ist wunderbar, dass wir gleichzeitig fertig werden. Ich kann mir niemand Besseren vorstellen, mit dem ich diesen Moment zusammen feiern möchte.

Henrik, danke, dass ich mich immer auf dich verlassen kann.

Kerstin, Mario, Rainer, Pavel, Claudia und ganz viele andere: Danke für die entspannte Arbeitsatmosphäre.

Bernhard, danke dass du mir zu so einem Ende verholfen hast.

Danke an alle, deren Namen hier nicht stehen, ich bin froh dass es euch gibt.

Hauke, danke für Spaß, Motivation und Enthusiasmus - wir haben da was richtig gutes auf die Beine gestellt.

Danke liebe Studierende, fürs Aushalten und Mitmachen meiner didaktischen Experimente und das tolle Feedback, das mich in schwierigen Zeiten über Wasser gehalten hat.

Danke liebes ET-CC Team für gute Ideen und gute Stimmung.

Danke an das ZHD und die GSGS für außerordentlich gute Workshops.

Christian, danke für die vielen gemeinsamen Jahre, ich hatte eine wunderbare Zeit neben dir erwachsen zu werden.

Opa, ich bin froh, dass ich diesen Moment mit dir teilen kann.

Liebe Andrea, liebe Oma, euch gebührt die letzte Zeile. Ihr fehlt mir.



# Erklärung

Ich versichere, dass ich die von mir vorgelegte Dissertation selbständig angefertigt, die benutzten Quellen und Hilfsmittel vollständig angegeben und die Stellen der Arbeit - einschließlich Tabellen, Karten und Abbildungen -, die anderen Werken im Wortlaut oder dem Sinn nach entnommen sind, in jedem Einzelfall als Entlehnung kenntlich gemacht habe; dass diese Dissertation noch keiner anderen Fakultät oder Universität zur Prüfung vorgelegen hat; dass sie - abgesehen von unten angegebenen Teilpublikationen - noch nicht veröffentlicht worden ist, sowie, dass ich eine solche Veröffentlichung vor Abschluss des Promotionsverfahrens nicht vornehmen werde. Die Bestimmungen der Promotionsordnung sind mir bekannt. Die von mir vorgelegte Dissertation ist von PD Dr. Ulrich Löhnert betreut worden.

Köln, 14. März 2019

Nils Kuchler

## Teilpublikationen

N. Kuchler et al. (2017). "A W-Band Radar–Radiometer System for Accurate and Continuous Monitoring of Clouds and Precipitation". In: *Journal of Atmospheric and Oceanic Technology* 34.11, pp. 2375–2392. ISSN: 0739-0572. DOI: [10.1175/JTECH-D-17-0019.1](https://doi.org/10.1175/JTECH-D-17-0019.1). URL: <http://journals.ametsoc.org/doi/10.1175/JTECH-D-17-0019.1>

N. Kuchler and U. Löhnert (2018). "Radar-radiometer based liquid water content retrievals of warm low-level clouds: how the measurement setup affects retrieval uncertainties". In: *IEEE Journal of Selected Topics in Applied Earth Observations and Remote Sensing* under review

N. Kuchler et al. (2018). "Revisiting liquid water content retrievals in warm stratified clouds: The modified Frisch". In: *Geophysical Research Letters* 45.17.  
DOI: <https://doi.org/10.1029/2018GL079845>

# Nils Küchler

## Curriculum vitae

Subbelrather Straße 284  
50825 Köln  
✉ nilskuechler@posteo.de

---

### Personal Information

Date and place of birth **31 October 1987**, Karlsruhe, Germany.

---

### Education

03/2015 – **PhD Student**, *Institute for Geophysics and Meteorology*, University of Cologne,  
10/2018 Germany.

#### PhD Thesis

Title **Ground-based remote sensing of warm low-level stratified clouds - new perspectives and applications.**

08/2018 **NRW-Zertifikat “Professionelle Lehrkompetenz für die Hochschule”**  
(**NRW-Certificate “Professional Teaching Competence at the University”**), *Center for University Didactics*, University of Cologne, <http://zhd.uni-koeln.de/23376.html>.

#### Project Work

Title **Soziale und Ethische Verantwortung von Wissenschaftler\*innen: Interdisziplinäre Perspektiven.**

10/2012 – **Master of Science**, *Physics of the Earth and Atmosphere - Meteorology*, University of Cologne, Germany.  
02/2015

#### Master's Thesis

Title **Characterization and Improvement of Absolute Calibration Techniques for Microwave Radiometers.**

10/2009 – **Bachelor of Science**, *Geophysics and Meteorology*, University of Cologne, Germany.  
06/2012

#### Bachelor's Thesis

Title **Calibration of Microwave Radiometers.**

06/2007 **Allgemeine Hochschulreife (High School)**, *Ludwig-Marum Gymnasium*, Pfinztal, Germany.

---

### Civil and Voluntary Service

- 09/2008 – **Voluntary service in South Africa**, *Organization: Leka Gape*, Program  
07/2009 »weltwärts« of the Federal Ministry for Economical Cooperation and Develop-  
ment, Germany.
- 09/2007 – **Civil service**, *Arbeiter und Samariterbund Karlsruhe e.V.*, elderly care.  
05/2008

---

## Publications and Awards

### Peer-Reviewed Articles

- 08/2018 **N. Kuchler, S. Kneifel, U. Löhnert, and P. Kollias**, *Revisiting liquid water content retrievals in warm stratified clouds: The modified Frisch*, *Geoph. Res. Letters*, <https://doi.org/10.1029/2018GL079845>.
- 07/2018 **H.-P. Vehrs und N. Kuchler**, *Lehren im interdisziplinären Team: das Team als Lerngegenstand*, *Neues Handbuch Hochschullehre*, DUZ Medienhaus, accepted.
- 04/2018 **N. Kuchler and U. Löhnert**, *Radar-radiometer based liquid water content retrievals of warm low-level clouds: how the measurement setup affects retrieval uncertainties*, *IEEE J. of Sel. Top. in Appl. Earth Observ. and Rem. Sens.*, under review.
- 11/2017 **N. Kuchler, S. Kneifel, U. Löhnert, P. Kollias, H. Czekala, and T. Rose**, *A W-Band Radar-Radiometer System for Accurate and Continuous Monitoring of Clouds and Precipitation.*, *J. Atmos. Ocean. Tech.*, <https://doi.org/10.1175/JTECH-D-17-0019.1>.
- 03/2016 **N. Kuchler, D. D. Turner, U. Löhnert, and S. Crewell**, *Calibrating ground-based microwave radiometers: Uncertainty and drifts.*, *Radio Science.*, <https://doi.org/10.1002/2015RS005826>.
- 04/2014 **S. Paine, D. D. Turner, and N. Kuchler**, *Understanding thermal drift in liquid nitrogen loads used for radiometric calibration in the field.*, *J. Atmos. Ocean. Tech.*, doi: 10.1175/JTECH-D-13-00171.1.
- 09/2012 **B. Pospichal, G. Maschwitz, N. Kuchler, and T. Rose**, *Standing Wave Patterns at Liquid Nitrogen Calibration of Microwave Radiometers.*, *Proceedings of the 9th International Symposium on Tropospheric Profiling, L'Aquila/Italy.*

### Awards

- 07/2018 **Albertus-Magnus Award for Excellent Teaching**, *Department for Geosciences*, University of Cologne.
- 07/2017 **Award for Excellent Supervising**, *Student Council of the Institute for Geophysics and Meteorology*, University of Cologne.
- 04/2016 **MicroRad 2016 Poster Award**, *MicroRad 2016 Conference*, Espoo, Finland, April 11-14, 2016.